IMPERIAL COLLEGE LONDON

Nonlocal Effects in Plasmonic Nanostructures

by

Aeneas Wiener

A thesis submitted in partial fulfillment for the
degree of Doctor of Philosophy

in the
Faculty of Natural Sciences
The Blackett Laboratory

24th September 2014

IMPERIAL COLLEGE LONDON

ABSTRACT

FACULTY OF NATURAL SCIENCES
THE BLACKETT LABORATORY

Doctor of Philosophy

by Aeneas Wiener

The field of plasmonics investigates how electromagnetic fields can be confined into sub-wavelength dimensions. This discipline constitutes a major subset of nano-photonics, and is enabled by the rich physics of light-matter interactions at the nano-scale. However, at the lower end of the length scales involved in plasmonic devices, metals are often shaped to have dimensions that approach the thickness of only a few atomic layers, which makes classical local electrodynamics insufficient due to the emergence of nonlocal and quantum effects that are not included in the model.

In this thesis we focus specifically on nonlocal effects, investigating their impact in experimentally relevant plasmonic nanostructures. In order to describe the spatial dispersion in the metal permittivity, we develop a full three-dimensional nonlocal hydrodynamic solution of *Maxwell*'s equations in frequency domain, complementing it with analytical closed form solutions where possible.

In this way, effects of nonlocal electron-electron interactions in the dielectric response of metals are taken into account in a phenomenological fashion, offering deep insights into the way spatial dispersion modifies the electromagnetic response of plasmonic nanostructures.

The geometries we investigate are driven by both plane wave and electron beam sources, mimicking experimental conditions. We use our numerical approach to perform an exhaustive analysis of the impact of nonlocality in the plasmonic response of five experimentally relevant plasmonic structures: plasmonic hourglass metal-insulator-metal waveguides, kissing metallic nanowires, nanofocusing metallic tips, three-dimensional nanocrescent light harvesters, and coupled metallic nanoprisms under electron beam excitation.

Our results demonstrate the complexity of the interplay between nonlocal and geometric effects taking place in the structures under investigation. We discuss the different sensitivities to both effects of the various plasmonic modes supported by these structures.

© Copyright 2014 Aeneas Wiener

"The copyright of this thesis rests with the author and is made available under a Creative Commons Attribution Non-Commercial No Derivatives license. Researchers are free to copy, distribute or transmit the thesis on the condition that they attribute it, that they do not use it for commercial purposes and that they do not alter, transform or build upon it. For any reuse or redistribution, researchers must make clear to others the license terms of this work." (Imperial College London PhD regulations 2012)

Declaration of Originality

I hereby certify that all materials presented in this theses, unless where indicated otherwise in the body of the text using appropriate referencing, is my own work.

Aeneas Wiener

Contents

Acknowledgements **1**

1 Introduction **7**
1.1 Plasmonics . . . 9
1.2 Nonlocality . . . 14
1.2.1 Conceptual background . . . 14
1.2.2 Experiments . . . 15
1.2.3 Quantum theories . . . 18
1.2.4 Meso-scale theories . . . 19

2 Theory **21**
2.1 Electrodynamics . . . 21
2.2 The finite element method . . . 23
2.3 Dielectric functions . . . 24
2.3.1 Drude dielectric function . . . 24
2.3.2 Hydrodynamic model . . . 28
2.3.3 Additional boundary conditions . . . 30
2.4 Nonlocal analytical solutions . . . 32
2.4.1 Infinite metallic half-space . . . 33
2.4.2 Infinite metallic cylinder . . . 37
2.4.3 Infinite metal-insulator-metal waveguide . . . 39
2.5 Nonlocal FEM solutions . . . 41
2.6 Calculating dispersion relations . . . 45

3 Results **47**
3.1 Nonlocality induced tunneling of surface plasmons through singular contacts 49
3.1.1 Introduction . . . 49
3.1.2 Methods . . . 50
3.1.3 Results and discussion . . . 52
3.1.4 Conclusion . . . 57
3.2 Nonlocal resonances in kissing plasmonic nanowires . . . 58
3.2.1 Introduction . . . 58
3.2.2 Methods . . . 59
3.2.3 Results and discussion . . . 59
3.2.4 Conclusion . . . 62
3.3 Nonlocal effects in the nanofocusing performance of plasmonic tips . . . 63
3.3.1 Introduction . . . 63

3.3.2 Methods . . . 63
3.3.3 Results and discussion . . . 65
3.3.4 Conclusion . . . 73
3.4 Nonlocal effects in three-dimensional nanocrescent light harvesters . . . 74
3.4.1 Introduction . . . 74
3.4.2 Methods . . . 76
3.4.3 Results and discussion . . . 77
3.4.4 Conclusion . . . 80
3.5 Probing the nonlocal response using electron beam excitation . . . 80
3.5.1 Introduction . . . 80
3.5.2 Theory . . . 81
3.5.3 Results and discussion . . . 84
3.5.4 Conclusion . . . 93

4 Conclusion **95**

Bibliography **99**

A1 Drude fitting **111**

A2 Copies of permission documents **113**

List of Figures

1.1 Dispersion relation for an Surface Plasmon Polariton (SPP) propagating along the interface of an infinite metallic half space with bulk plasma frequency ω_{P} (solid line), alongside the dispersion relation of light propagating in air (dashed line) and in silica (dotted line.) 9

1.2 Normalised electric field component E_y/E_0 for an SPP propagating in the x direction along the metal-dielectric interface, evaluated at $0.7\omega_{\mathrm{SPP}}$. The saturated colour scale ranges from -1 (blue) to 1 (red.) 10

1.3 A dielectric prism is separated from a thin metallic film with a small air gap. In the *Otto* configuration (a), the SPPs (dotted arrow) are excited on the upper side of the metallic film. In the *Kretschmann* configuration (b) the metallic film is deposited directly onto the prism and SPPs are excited on the lower side of this thin film. 11

1.4 Excitation of SPPs using a metallic grating with period a. Radiation is incident on the grating at an angle θ and with wavevector k. 11

1.5 Absorption cross section C_{abs} for a gold sphere suspended in air, for sphere radii a = 10, 30 and 80 nm. Results calculated using the quasi-static approach (solid blue lines) are compared to the full electrodynamic result obtained from *Mie* theory (dashed black lines.) 13

1.6 (a) Theoretical nonlocal (solid line) and local (dashed line) transmittance spectrum for p-polarized light incident on a 52 Angstrom thick potassium film. Adapted from Ref. [87] (b) Transmittance spectra of a thin silver film for p-polarized light and for three different film thicknesses, 110, 120 and 145 Angstrom. The angle of incidence is 75deg. Adapted from Ref. [72] Copyright 1971 by the Royal Swedish Academy of Sciences. Reproduced by permission of IOP Publishing. All rights reserved. 16

1.7 (a) Experimental results for small metal spheres. Comparison of experimental data with quantum theory for Ag Nano-Particles (NPs) ranging in diameter from 20 nm to less than 2 nm are reproduced. Experimental, EELS-determined localized surface plasmon resonance energies of various particle diameters are plotted on the absorption spectra generated from an analytic quantum permittivity model. The experimental bulk resonance energies (grey dots) together with the theory predictions (grey line) are also plotted. The local *Mie* theory peak prediction is given by the dashed white line. Adapted from Ref. [128] (b) Experimental results for a coupled NP-film system. The trace of the surface plasmon scattering peak as a function of particle-film separation is reproduced. Experimental results (markers) are compared with results from theoretical nonlocal (solid red line) and local (dashed black line) calculations. Adapted with permission from Ref. [23] Copyright 2012 by The American Association for the Advancement of Science. 16

1.8 Onset of quantum tunnelling in sub-nm plasmonic cavities. (a) Measured dark-field optical back-scattering with increasing force applied to the inter-tip cavity (decreasing inter-tip cavity size). The onset of the quantum regime is marked at d_{QR}. (b) Theoretical total scattering intensity from a tip-tip system incorporating quantum mechanical tunnelling. (c) Theoretical scattering intensity as in (b) but using purely classical calculations. Adapted with permission from Ref. [125] Copyright 2012 by Nature Publishing Group. 17

1.9 Theoretical Time Dependent Local Density Approximation (TDLDA) results for a diminutive metallic dimer. (a) The dipolar (full circles) and quadrupolar (open circles) dimer plasmon energy as a function of the radius normalised diameter d/R, for of radius $R = 16$ (red) and 24 *Bohr* radii (blue) sphere dimers calculated using TDLDA. The local result is rendered with solid (dipolar) and dashed (quadrupolar) lines. (b) Trace of the maximum electromagnetic field enhancements calculated using the local theory (red) and TDLDA (blue) for spheres with radius $R = 24$ *Bohr* radii forming dimers of separations $d = 24$ (A), 8 (B), 4 (C), and 2 *Bohr* radii (D). (c) Field distributions calculated using local theory (top panels) and TDLDA (bottom panels). Adapted with permission from Ref. [156] Copyright 2009 by the American Chemical Society. 18

1.10 Illustration of the quantum corrected model. (a) A simple plasmonic system composed of two semi-infinite planar interfaces separated by a distance l is used to obtain a characteristic tunnelling transmission $T(l)$. The tunnelling-induced conductivity between these surfaces defines an effective separation-dependent dielectric material $\epsilon(l, \omega)$ used in the quantum corrected model. (b) In the case of a metallic dimer (schematically depicted) ϵ_i, obtained in the previous step, is used as a separation-dependent dielectric constant of the shells of fictitious material that accounts for the quantum tunnelling. A number of shells (i = 1,...,n) are used. (c) The normalized electron tunnelling transmission $T(l)/T(0)$ and (d) tunnelling damping γ_g is plotted as a function of the separation distance l. In both (c) and (d), red corresponds to a Na jellium material, and blue to a Au jellium. Adapted with permission from Ref. [32] Copyright 2012 by Nature Publishing Group. 20

2.1 Infinite metallic half space. 33

2.2 Dispersion relation for SPP propagating on an infinite metallic metallic half space. 35

2.3 Infinitely long metallic cylinder of diameter d, embedded in air. The SPP mode is propagating in the z direction. 37

2.4 Infinite Two-Dimensional (2D) Metal-Insulator-Metal (MIM) waveguide with insulator thickness d, The SPP modes are propagating in the x direction. 39

2.5 Results for an $R = 2$ nm silver nanowire with $\epsilon_\infty = 1$, $\omega_p = 3.3$ eV and $\gamma = 0.01\omega_p$. (a) Local analytic (dashed line) and local FEM (solid line) absorption cross section. (b) nonlocal curl-free analytic [121] (dashed line) and nonlocal curl-free Finite Element Method (FEM) (solid line) absorption cross section. (c) nonlocal analytic [122] (dashed line) and nonlocal FEM (solid line) absorption cross section. (d) field plot corresponding to a. (e) field plot corresponding to (b). (f) field plot corresponding to (c). (g) nonlocal FEM (solid line) absorption cross section for different degrees of nonlocality. (h) E field along a line cutting through the cylinder of the incident field for different β. 44

3.1 Schematic renderings of plasmonic structures investigated: (a) 2D hourglass MIM waveguides under end-fire excitation, (b) 2D kissing metallic nanowires under plane wave illumination, (c) rotationally symmetric Three-Dimensional (3D) nanofocusing metallic tips under end-fire excitation, (d) rotationally symmetric 3D nanocrescent light harvesters under plane wave illumination, and (e) coupled metallic nanoprisms under electron beam excitation, separated from a dielectric substrate by a thin chromium adhesion layer. 48

3.2 (a) 3D rendering of a linearly tapered MIM hourglass waveguide with translational invariance in the direction normal to the page (y-direction). The arrow indicates the direction of SPP propagation. (b) Schematic xz-plane view of the structure depicted in panel (a), with input gap thickness D, hourglass waist thickness W, arm length L', SPP path length L, and gap (metal) permittivity ϵ_1 and (ϵ_2). The hourglass angle α is measured wall to wall. Note that the x and z axes are displaced for clarity. The coordinate origin is located at the center of the hourglass waist. 50

3.3 (a) Dispersion relation for the lowest SPP mode supported by a silver-air-silver MIM waveguide with gap thickness d, ranging from 1 nm to 50 nm. Black dashed (red solid) lines show local (nonlocal, $\beta = 0.0036c$) results. The inset renders the modal propagation length as a function of frequency. (b) Schematic of the infinite MIM geometry used in panel (a), fully characterised by the gap thickness d, gap permittivity ϵ_1 and metal permittivity ϵ_2. Reprinted with permission from Ref. [149]. Copyright 2013 by The Optical Society of America. 53

3.4 Real part of the electric z-field component (E_z/E_0) evaluated at $0.7\omega_{\mathrm{SPP}}$, plotted along the surface of a silver-air-silver plasmonic hourglass waveguide with $L = 1000$ nm, $D = 60$ nm and $W = 0$ nm. Dots and solid lines render FEM and analytical *Wentzel-Kramers-Brillouin* (WKB) calculations, respectively. Local (nonlocal) results are plotted in black (red). Reprinted with permission from Ref. [149]. Copyright 2013 by The Optical Society of America. 54

3.5 (a) Frequency dependent electric z-field amplitude enhancement $|E_z/E_0|$ evaluated at the waist of the waveguide, for different hourglass waist thicknesses W, for fixed $L = 1000$ nm and $\alpha = 3.44°$. Good agreement between WKB analytical (lines) and FEM numerical (dots) results is observed. Nonlocal and local predictions are shown in red and black, respectively (b) $|E_z/E_0|$ for $\omega = 0.7\omega_{\rm SPP}$, plotted as a function of the hourglass angle α. The hourglass waist is fixed to $W = 0.1$ nm, with all other parameters taking the same values as in panel (a). Reprinted with permission from Ref. [149]. Copyright 2013 by The Optical Society of America. 55

3.6 (a) $|E_z/E_0|$ evaluated at $0.7\omega_{\rm SPP}$, along the surface of a silver-air-silver plasmonic hourglass waveguide with length $L = 1000$ nm and input gap thickness $D = 60$ nm. Nonlocal (local) FEM numerical results are plotted in red (black). Results for hourglass waist thicknesses of both $W = 0.15$ nm and $W = 5$ nm are rendered. (b) and (c) Nonlocal $|E_z/E_0|$ map for the $W = 0.15$ nm and $W = 5$ nm cases in panel (a). (d) Same as panel (a), but for $W < 0$ ($g = W/(\tan(\alpha/2))$. Results for separation metal thicknesses of $g = 0.5$ nm and $g = 5$ nm are rendered. (e) and (f) Nonlocal $|E_z/E_0|$ map for the $g = 0.5$ nm and $g = 5$ nm cases in panel (d). Reprinted with permission from Ref. [149]. Copyright 2013 by The Optical Society of America. 56

3.7 (a) Sketch of kissing metallic nanowires enclosed in vacuum with the incident field polarised along the dimer axis. (b) FEM results for nonocal E_y at around the touching point and at 7 eV. (c) nonocal E_y in the bulk of the nanowires at 8.5 eV. All results are for for a *Drude* metal with $\epsilon_\infty = 1$, $\omega_p = 8$ eV, $\gamma = 0.01\omega_p$ and $\beta = 0.001c$. The fields are normalised so that the pointing vector of the incident plane wave is unity. 59

3.8 Field enhancement in the vicinity of the touching point of two 10 nm radii Ag nanowires at $\omega = 0.5\omega_{\rm SP}$ and different degrees of nonlocality, $\delta/\lambda_{\rm P}$: 10^{-4} (blue), 10^{-3} (green) – this is a realistic value for Ag – and 10^{-2} (red). Solid (dotted) lines show transformation optics [37] (numerical) results. Grey line plots Ex/E0 under the local description. The inset displays $|E_x/E_0|$ at the touching point as a function of the incident frequency, $\omega/\omega_{\rm SP}$ and $\delta/\lambda_{\rm P}$. The white dashed line indicates the operating frequency in the main panel. Reprinted with permission from Ref. [37]. Copyright 2012 by the American Physical Society. 60

3.9 Theoretical [37] (solid lines) and numerical (dots) absorption spectra for 10 nm radii nonlocal nanowires, together with the cross section obtained within the local approximation (grey dashed line). $\sigma_{\rm abs}$ for a local (nonlocal, $\delta = 10^{-2}\lambda_{\rm P}$) single nanowire is also plotted in solid (dashed) black line. Panel (b): Real part of the phase accumulated by the circulating surface plasmon modes in one loop around the nanowires. (c) Field enhancement close to the touching point at the three lowest nonlocal resonances for $\delta = 10^{-3}\lambda_{\rm P}$ (value appropriate for silver). Reprinted with permission from Ref. [37]. Copyright 2012 by the American Physical Society. 61

3.10 Absolute value of the field enhancement at the touching point as a function of ω/ω_{SP} and R. Solid (dashed) lines in the inset render theoretical [37] (numerical) —Ex/E0— at the two lowest enhancement maxima for R = 50 nm: $0.55\omega_{SP}$ (yellow), $0.72\omega_{SP}$ (green). Results are for for Ag with $\beta = 3.6\times10^{-3}$c. Reprinted with permission from Ref. [37]. Copyright 2012 by the American Physical Society. 62

3.11 (a) Dispersion relation for the symmetric SPP mode supported by silver slabs of thickness d. Black solid (red dashed) lines show local (nonlocal, $\beta = 0.0036c$) results. The inset renders the modal propagation length as a function of frequency. (b) The same as (a) but for the azimuthally independent SPP mode suported by silver cylinders of diameter d. In both panels, the SPP frequency and wavevector are normalized to the surface plasmon frequency, defined as $\mathrm{Re}(\epsilon_D(\omega_{SPP})) = -1$. Reprinted with permission from Ref. [148]. Copyright 2012 by the American Chemical Society. 66

3.12 (a) Enhancement in the radial component of the electric field along the surface of a plasmonic Ag tip with $L = 1.5\mu$m and $\alpha = 6^\circ$ evaluated at $\omega = 0.6\omega_{SPP}$. WKB (lines) and FEM (crosses) calculations are shown for both a local (black) and nonlocal (red) description of the tip dielectric response. (b) Absolute value of the electric field in the same geometry as in panel (a) within the local approximation (solid line) and for two values of β: $0.0036c$ (dashed line) and $0.01c$ (dotted line). (c) Normal component of the electric field along the surface of a Ag wedge of the same dimensions as (a) and (b) at $\omega = 0.6\omega_{SPP}$. Panels (b) and (c) show WKB results. In all panels, the Electromagnetic (EM) fields are normalized to the input amplitude E_0. Reprinted with permission from Ref. [148]. Copyright 2012 by the American Chemical Society. 67

3.13 Local (a) and nonlocal (b) electric fields at $\omega = 0.6\omega_{SPP}$ along the conical tip geometry considered in fig. 3.12 (a). The right contour plots show E_r maps within the symmetry plane of the structure. The left panels plot the radial and parallel components of the electric field 5nm (solid lines) and 10nm (dotted lines) away from the apex. In all cases, fields are normalized to the input amplitude, E_0. The saturated color scale in the contour plots ranges from -100 (blue) to 100 (red). Reprinted with permission from Ref. [148]. Copyright 2012 by the American Chemical Society. 68

3.14 (a) Absolute value of the field enhancement, $|E/E_0|$, at the tip end as a function of the operating frequency for $L = 1.5\mu$m and $\alpha = 6^\circ$. The inset renders local (black) and nonlocal (red) $|E/E_0|$ obtained from WKB calculations at $0.6\omega_{SPP}$ (solid lines) and $0.8\omega_{SPP}$ (dashed lines) as a function of the tip length ($\alpha = 6^\circ$). (b) Electric field enhancement as a function of the tip angle evaluated at $\omega = 0.6\omega_{SPP}$. Reprinted with permission from Ref. [148]. Copyright 2012 by the American Chemical Society. 69

3.15 (a) Absolute value of the electric field ($\omega = 0.6\omega_{\rm SPP}$) in the vicinity of three different blunt plasmonic tips ($L = 1.5\mu$m, $\alpha = 10^\circ$) characterized by the apex diameter $D_{\rm out}$. Local (black) and nonlocal (red) FEM calculations are shown. In all cases, the fields are normalized to their value at the tip surface. Panels (b), (c) and (d) display nonlocal near field amplitude maps for $D_{\rm out} = 0.1$, 0.5, and 1 nm, respectively. Reprinted with permission from Ref. [148]. Copyright 2012 by the American Chemical Society. 71

3.16 (a) Absolute value of the local (black lines) and nonlocal (red lines) electric field on the surface of a silver cone of length $L = 1500$ nm and angle $\alpha = 10$ deg. The surface roughness is achieved by radially displacing points on the surface every 0.25 nm by a random number in the range -0.25 nm to $+0.25$ nm. The inset renders the fields on the surface of the cone. (b) Contour plot of the local radial electric field at $\omega = 0.8\omega_{\rm SPP}$ for the cone used in panel a. (c) Contour plot of the nonlocal radial electric field ($\omega = 0.8\omega_{\rm SPP}$) for the cone used in panel a. Reprinted with permission from Ref. [148]. Copyright 2012 by the American Chemical Society. . . . 72

3.17 Contour plots of the local (top) and nonlocal (bottom) radial electric fields at $\omega = 0.8\omega_{\rm SPP}$ in an Ag tip with $L = 1500$ nm and $\alpha = 10^\circ$. In all cases, the surface roughness is achieved by radially displacing points on the surface by a random number in the range -0.25 nm to $+0.25$ nm. Panels (a) and (b) show results based on points spaced 0.25 nm away from each other along the surface. In panels (b) and (c) the spacing between points on the surface was increased to 1 nm. The points form the basis of the cubic spline interpolation which defines the metal dielectric interface. The saturated color scale ranges from $E_r/E_0 = -35$ (blue) to $E_r/E_0 = 35$ (red). Reprinted with permission from Ref. [148]. Copyright 2012 by the American Chemical Society. 73

3.18 Schematic depiction of a metallic nanocrescent, rotationally symmetric around the z-axis, with outer radius R_o and inner radius R_i. The structure is blunted through a hole of radius R_b which is cut at the thin end of the crescent. Plane wave illumination, polarised perpendicular to the z-axis, is incident from the thin side of the crescent. 74

3.19 (a) Absorption cross section of gold nanocrescents with $R_{\rm o} = 10$ nm and $\tau = 0.85$. The red (blue) line renders the nonlocal (local) spectrum for the singular (blunt) geometry with $R_{\rm b} = 0$ ($R_{\rm b} = 1$ nm). For comparison, the singular, local cross section is plotted in black line. The inset shows nonlocal $\sigma_{\rm abs}/R_{\rm o}^3$ for singular crescents with 10 (red) and 40 (green) nm outer radius, together with the nonlocal spectrum for a solid nanosphere (black). (b) Field enhancement versus θ for the lowest absorption maximum in the nonlocal (red) and blunt (blue) spectra in (a). The lower inset shows E_z/E_0 for the three lowest nonlocal resonances in (a). The upper panel plots the maximum $|E_z/E_0|$ versus frequency for $R_{\rm o} = 10$ (red) and 40 (green) nm crescents within the nonlocal approximation. Reprinted with permission from Ref. [34]. Copyright 2012 by the American Chemical Society. 77

3.20 (a) Absorption cross section of gold nanocrescents with $R_o = 10$ nm and $\tau = 0.5$. The red (blue) line renders the nonlocal (local) spectrum for the singular (blunt) geometry with $R_b = 0$ ($R_b = 0.88$ nm). For comparison, the singular, local cross section is plotted in black line. The inset shows nonlocal σ_{abs}/R_o^3 for singular crescents with 10 (red) and 40 (green) nm outer radius, together with the nonlocal spectrum for a solid nanosphere (black). (b) Field enhancement versus θ for the lowest absorption maximum in the nonlocal (red) and blunt (blue) spectra in (a). The lower inset shows nonlocal $|E/E_0|_max$ for a solid nanosphere (a). The upper panel plots the maximum $|E_z/E_0|$ versus frequency for $R_o = 10$ (red) and 40 (green) nm crescents within the nonlocal approximation. Reprinted with permission from Ref. [34]. Copyright 2012 by the American Chemical Society. 79

3.21 Simulated Electron Energy Loss Spectroscopy (EELS) response of single gold nanoprisms (height $D = 0.3L$) on a 1 nm chromium adhesion layer, supported by a SiN_x membrane of thickness D. (a) Black and red lines plot local (1.6 eV) and nonlocal (1.9 eV) E_y^{ind} along the y-axis of a nanoprism with $L = 5$ nm. (b) Local E_y^{ind} map within the $z = D/2$ plane at 1.6 eV. (c) The same as (b) but under the nonlocal description and at 1.9 eV. In both panels, the saturated color scale ranges from positive (red) to negative (blue) electric field amplitude, and the position of the electron beam source is indicated by a grey dot. (d) Simulated local (black) and nonlocal (red) EELS spectra for single nanoprisms with various L. In order to make the system fully scalable, we have set the distance between target and source to $0.15L$. (e) Trace of the spectral position of the modes identified in panel (d). The insets show saturated nonlocal charge density maps ($L = 5$ nm) at the energies of the dipole (1.9 eV) and quadrupole (2.4 eV) modes. Reprinted with permission from Ref. [147]. Copyright 2013 by the American Chemical Society. 85

3.22 Geometry considered in our calculations. Two gold nanoprisms of height D and side length L, connected through a bridge of width d and length g (measured apex to apex). The resulting structure is separated from a SiN_x supporting membrane through a 0.5 nm thick chromium adhesion layer. The impact parameter of the electron beam is $0.15L$ nm away from the center of the outer side of the connected nanoprisms. 87

3.23 Simulated $\Gamma_{EELS}(\omega)$ for connected gold nanoprisms of side length L and height $D = 0.3L$. The bridge width and length are $d = 0.1L$ and $g = 0$, respectively. The nanostructures are placed on top of a 0.5 nm chromium layer, and supported by a SiN_x membrane of thickness D. The distance target-excitation is $0.15L$. (a) Local (black) and nonlocal (red) E_y^{ind} along the y-axis for $L = 5$ nm evaluated at 0.75 and 0.8 eV, respectively. (b) Local E_y^{ind} maps within the $z = D/2$ plane at 0.75 eV. (c) The same as (b) but under the nonlocal description and at 0.8 eV. The position of the electron beam is indicated by a grey dot in both panels. (d) Simulated local (black) and nonlocal (red) $\Gamma_{EELS}(\omega)$ for connected nanoprisms with L ranging from 5 to 200 nm. (e) Trace of the spectral position of the EELS maxima identified in panel (d). The insets show saturated nonlocal charge density maps for the $L = 5$ nm dimer. Reprinted with permission from Ref. [147]. Copyright 2013 by the American Chemical Society. 88

3.24 (a) Simulated local (black) and nonlocal (red) EELS spectra for gold nanoprisms connected by bridges of various widths, d ($L = 10$, $D = 3$, and $g = 0$ nm). The target configuration (substrate, adhesion layer, electric beam excitation) remain the same as in Figure 3.23. (b) Electric field amplitude along the bridge width for the three narrowest geometries in (a). Top (bottom) profiles correspond to local (nonlocal) calculations. (c) Trace of the local (black) and nonlocal (red) resonances for connected nanoprisms against d (top, $g = 0$ nm) and against g (bottom, $d = 1$ nm). Reprinted with permission from Ref. [147]. Copyright 2013 by the American Chemical Society. 89

3.25 (a) Experimental EELS spectra for connected gold nanoprisms with $L =$ 70 nm, $D = 20$ nm, and $d = 1.6$ nm, 4 nm and 7 nm. The bowties are placed on top of a 1 nm chromium layer and are supported by a 30 nm thick SiN_x membrane. The inset shows a Transverse Electromagnetic (TEM) image of one of the samples. (b)-(c) TEM images zooming at the two narrowest connective bridges. (d) Local (dotted lines) and nonlocal (solid lines) simulations mirroring the experimental geometries in (a). (e)-(f) Nonlocal charge density maps evaluated at the charge transfer resonance for the geometries modelling the bridges in (b)-(c). (g) Local $\Gamma_{\mathrm{EELS}}(\omega)$ for bowties with $d = 1.6$ nm and chromium bridges of height 5, 2, 1 and 0 nm (from top to bottom). (h) The same as (g) but for 1 nm chromium thickness and increasing *Drude* damping frequency at the gold bridge, effectively modelling grain boundary electron scattering effects. The top (bottom) spectrum corresponds to an increase in the gold damping frequency by a factor of 1 (75) with respect to the prism regions. Reprinted with permission from Ref. [147]. Copyright 2013 by the American Chemical Society. 91

1 Real (bottom panel) and imaginary (top panel) parts of the permittivity used in all calculations. Results from Palik experimental data for silver (red crosses) are compared to our Drude fit based on 1 (black lines). The Drude fitting parameters are $\epsilon_\infty = 3.46 + 0.256i$, $\omega_{\mathrm{P}} = 8.59$eV, $\gamma = 0.075$eV, which gives $\mathrm{Re}(\epsilon_{\mathrm{D}}) = -1$ at $\omega_{\mathrm{SPP}} = 4.06$eV. 111

2 Permission to reproduce figures from: Bridging quantum and classical plasmonics with a quantum-corrected model 113

3 Permission to reproduce figures from: Electron-Energy Loss Study of Nonlocal Effects in Connected Plasmonic Nanoprisms 114

4 Permission to reproduce figures from: Experimental Verification of Optically Excited Longitudinal Plasmons 115

5 Permission to reproduce figures from: Nonlocal Effects in the Nanofocusing Performance of Plasmonic Tips 116

6 Permission to reproduce figures from: Plasmonic Sinks for the Selective Removal of Long-Lived States 117

7 Permission to reproduce figures from: Probing the Ultimate Limits of Plasmonic Enhancement 118

8 Permission to reproduce figures from: Quantum Description of the Plasmon Resonances of a Nanoparticle Dimer 119

9 Permission to reproduce figures from: Rapid Ultrasensitive Single Particle Surface-Enhanced Raman Spectroscopy Using Metallic Nanopores 120

10 Permission to reproduce figures from: Revealing the quantum regime in tunnelling plasmonics 121
11 Permission to reproduce figures from: Theory of Three-Dimensional Nanocrescent Light Harvesters 122

Acknowledgements

My time at Imperial College London has been an exciting and stimulating experience thanks to the numerous people who have offered their generous support along the way, to only some of whom it is possible to give particular mention here. First, I would like to thank my supervisors Dr Andrew Horsfield and Professor Stefan Maier for giving guidance to my research and for inspiring me with their enthusiasm and commitment to science. Besides my supervisors, it was Dr Antonio Fernandez-Dominguez whom I would like to thank foremost for always being there for my questions, for teaching me how to construct scientific arguments and present my work to others. Next, I thank my fellow postgraduate students and postdoctoral researchers and academic staff from across the college for numerous opportunities for stimulating discussions and collaborative work. In particular, I would like to thank Professor Alexei Kornyshev, Professor Joshua Edel, Dr Stephane Kena-Cohen, Dr Yonatan Sivan, Dr Yu Luo and Dr Michael Cecchini. I also thank the Doctoral Training Center for Theory and Simulation of Materials for funding, and for providing an enthusiastic environment for extracurricular activities. In particular, it was the leadership of Professor Adrian Sutton, Professor Peter Haynes, Dr Arash Mosofi and the late Julian Walsh who have made possible the founding of the Hermes Summer School, for which Jassel Majevadia and so many others so generously volunteered their time. Finally, I would also like to thank my friends and family in London and in Switzerland for their invaluable support.

2D Two-Dimensional

3D Three-Dimensional

AC Alternating Current

ABC Additional Boundary Condition

AFM Atomic Force Microscope

DFT Density Functional Theory

DC Direct Current

EM Electromagnetic

EELS Electron Energy Loss Spectroscopy

FDTD Finite Difference Time Domain

FEM Finite Element Method

IMI Insulator-Metal-Insulator

LHS Left Hand Side

LSPR Localised Surface Plasmon Resonance

LSP Localised Surface Plasmon

MBC Maxwell Boundary Condition

MIM Metal-Insulator-Metal

MUMPS MUltifrontal Massively Parallel Sparse direct Solver

NP Nano-Particle

PML Perfectly Matched Layer

PDE Partial Differential Equation

PSP Propagating Surface Plasmons

RHS Right Hand Side

SEM Scanning Electron Microscope

SHG Second-Harmonic Generation

SPP Surface Plasmon Polariton

SPR Surface Plasmon Resonance

TE Transverse Electric

TEM Transverse Electromagnetic

TDDFT Time-Dependent Density Functional Theory

TDLDA Time Dependent Local Density Approximation

TM Transverse Magnetic

TO Transformation Optics

WKB *Wentzel-Kramers-Brillouin*

Publications

1. Nonlocal propagation and tunnelling of surface plasmons in metallic hourglass waveguides. Wiener, A.; Fernandez-Dominguez, A. I.; Pendry, J.B.; Horsfield, A.P.; Maier, S.A. Opt. Express, 21 (22), 27509-27518 (2013)

2. Rapid Ultrasensitive Single Particle Surface-Enhanced Raman Spectroscopy Using Metallic Nanopores. Cecchini, M. P.; Wiener, A.; Turek, V. A.; Chon, H.; Lee, S.; Ivanov, A.P.; McComb, D.W.; Choo, J.; Albrecht, T.; Maier, S.A.; Edel, J.B. Nano Lett., 13 (10), 46024609 (2013)

3. Surface Plasmons and Nonlocality: A Simple Model. Luo, Y.; Fernandez-Dominguez, A. I.; Wiener, A.; Maier, S.A.; Pendry, J. B. Phys. Rev. Lett. 111, 093901 (2013)

4. Electron-Energy Loss Study of Nonlocal Effects in Connected Plasmonic Nanoprisms. Wiener, A.; Duan, H.; Bosman, M.; Pendry, J.B.; Horsfield, A.P.; Yang, J.K.W.; Maier, S.A.; Fernandez-Dominguez, A.I. ACS Nano, 7 (7), 62876296 (2013)

5. Theory of Three-Dimensional Nanocrescent Light Harvesters. Fernandez-Dominguez, A I.; Luo, Y; Wiener, A; Pendry, J. B.; Maier, S. A. Nano Lett., 12 (11), 59465953 (2012)

6. Nonlocal Effects in the Nanofocusing Performance of Plasmonic Tips. Wiener, A.; Fernandez-Dominguez, A. I.; Horsfield, A. P.; Pendry, J. B.; Maier, S. A. Nano Lett, 12 (6), 33083314 (2012)

7. Transformation-Optics Description of Nonlocal Effects in Plasmonic Nanostructures. Fernandez-Dominguez, A. I.; Wiener, A.; Garcia-Vidal, F. J.; Maier, S. A.; Pendry, J. B. Phys. Rev. Lett., 108, 106802 (2012)

8. Plasmonic Sinks for the Selective Removal of Long-Lived States. Kana-Cohen, S.; Wiener, A.; Sivan, Y; Stavrinou, P.N.; Bradley, D.D.C.; Horsfield, A.P.; Maier, S.A. ACS Nano, 5 (12), 99589965 (2011)

Chapter 1

Introduction

In recent years, innovations in the field of nanophotonics have led to a wealth of technological applications in areas as diverse as high-sensitivity chemical and biological sensing [5; 152], improved photovoltaic light harvesting [7], signal processing based on active plasmonic nanostructures, [65], optical waveguiding [44], ultrafast photonic signal processing [78], nanolasing [100], and Electromagnetic (EM) field modulation using metamaterials [132; 129]. All these devices have been possible thanks to the enormous progress that nanofabrication and optical characterisation techniques have experienced lately. One of the central concepts in plasmonics that enables such rich physics is the Surface Plasmon Polariton (SPP), an infrared or visible frequency EM wave that propagates along a metal-dielectric or metal-air boundary. SPPs have exponentially decaying tails that extend into the metal and air regions. The name of this wave is derived from the fact that it involves the motion of charge in the metal regions (surface plasmons) and EM waves in the dielectric or air regions (polaritons). [79]

Typically, plasmonic devices have in the past involved structures whose metallic features are very large compared to the interatomic spacing, often involving geometries such as metallic films [102] and colloidal suspensions of metallic particles [150] with characteristic thicknesses greater than 10 nm. At such large length scales, as we will demonstrate in section 2.3.1, effects of nonlocality do occur but they do not affect significantly the EM response of matter, making classical local electrodynamics a suitable and extremely powerful tool to describe the physics of these devices.

However, the miniaturisation trend in the experimental production of many of the above plasmonic devices is reaching the limit where the local solutions of macroscopic *Maxwell*'s equations are no longer able to describe accurately their EM properties. The failure of the local picture originates from the emergence of strong nonlocal electron-electron interactions in the dielectric response of metals. These increase as the effective wavelength of the EM fields becomes comparable to the inter electronic distance, given by the *Coulomb* screening length, which is of the order of 0.1 nm in noble metals such as

gold or silver [61]. Therefore, the theoretical investigation of plasmonic phenomena in this sub-nanometer regime requires the implementation of nonlocal (spatially dispersive) permittivities to model the dielectric characteristics of plasmonic nanostructures, and ultimately a quantum mechanical treatment. [15]

At the current time, progress is being made towards a deeper understanding of the influence of nonlocality, or spatial dispersion,[1] on the permittivities of metals using three complementary approaches:

1. Optical experiments probing extremely thin films [4; 72] and diminutive particles; [104; 23]
2. Time dependent many-body quantum treatments viable for small system sizes [156; 32]; and
3. Phenomenological mesoscale models based on extensions of *Maxwell*'s equations into the nonlocal regime using, for example, a hydrodynamic approach. [38; 122; 41; 115; 148]

Out of these three, the hydrodynamic theory has advantages due to its ease of implementation, qualitative validity of results [133; 138], and the possibility to modulate the degree of nonlocality, offering theoretical insights into the way spatial dispersion modifies EM fields [37].

In this Thesis we study the effects of nonlocality on the optical properties of plasmonic systems, with a focus on identifying suitable numerical electromagnetics solutions that offer a convenient balance between computational complexity and physical insight. Once suitable solution strategies have been identified, the remaining parts of this thesis will focus on applying these solving strategies to a variety of plasmonic systems that are affected by spatial dispersion. In this way, we aim to provide both general insight about creating plasmonics models that incorporate effects of nonlocality, but also to identify and study new physical effects that come as a result of nonlocality.

This discussion is divided into three parts:

1. In chapter 1 we give a broad introduction to nonlocality in plasmonics. We explain how meso-scale descriptions of nonlocal effects are particularly well suited to treat spatial dispersion in experimentally relevant geometries, and further define the scope of the questions that will be addressed in this thesis.
2. In chapter 2 we show how nonlocality can be implemented into mesh based electromagnetics simulation schemes. We describe a nonlocal Finite Element Method (FEM) implementation, which solves *Maxwell*'s equations in the frequency domain, and show how analytical solutions can be obtained for certain special geometries.

[1] The terms nonlocality and spatial dispersion are used interchangeably in this Thesis

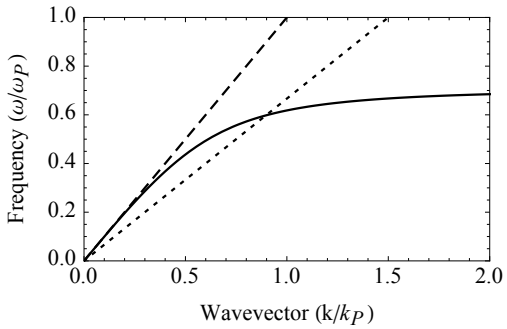


FIGURE 1.1: Dispersion relation for an SPP propagating along the interface of an infinite metallic half space with bulk plasma frequency ω_{P} (solid line), alongside the dispersion relation of light propagating in air (dashed line) and in silica (dotted line.)

3. In chapter 3 we apply nonlocal analytical and FEM simulations to five geometries which are expected to be affected by the inclusion of nonlocal effects: plasmonic hourglass Metal-Insulator-Metal (MIM) waveguides, kissing metallic nanowires, nanofocusing metallic tips, three-dimensional nanocrescent light harvesters, and coupled metallic nanoprisms under electron beam excitation.

1.1 Plasmonics

One of the exciting electromagnetic phenomena that can occur in metals are waves of free electron gas pressure in the bulk of the material. These so called bulk plasmon waves are predicted by *Maxwell*'s equations, and their energy is given by [57; 79]

$$E_{\mathrm{P}} = \hbar\omega_{\mathrm{P}} = \sqrt{\frac{ne^2}{m_e\epsilon_0}} \tag{1.1}$$

where $\hbar$ is the reduced *Planck* constant (or *Dirac* constant), ω_{P} is the frequency of the bulk plasma wave. n is the electron density, e is the charge of one electron, and m_e is the mass of one electron.

Closely related to bulk plasmons, there is another class of oscillations of the electron gas that can occur at metallic surfaces. These so called Surface Plasmon Polaritons (SPPs) are characterised by a broadband dispersion relation. In addition to the wide frequency window spanned by SPPs, their wave vectors are also highly geometry dependent. These factors open the door to the engineering of a wide class of nano-scale devices that exploit the ability to control SPP dispersion relations.

Perhaps the simplest geometry that supports SPPs is given by a finite metallic half space. Within the local approximation, the derivation of the SPP dispersion relation can straightforwardly be obtained from *Maxwell*'s equations. [79] The result of this

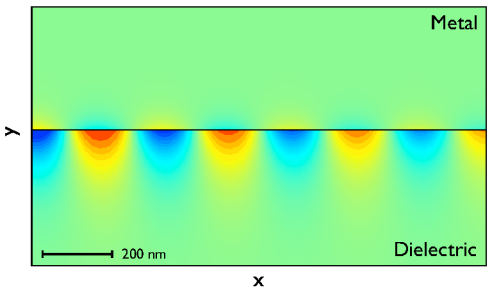


FIGURE 1.2: Normalised electric field component E_y/E_0 for an SPP propagating in the x direction along the metal-dielectric interface, evaluated at $0.7\omega_{\mathrm{SPP}}$. The saturated colour scale ranges from -1 (blue) to 1 (red.)

derivation, which is provided in full in section 2.4.1, is given by the SPP wavevector

$$k_{\mathrm{SPP}} = k_0 \sqrt{\frac{\epsilon_m \epsilon_d}{\epsilon_m + \epsilon_d}} \tag{1.2}$$

where $k_0 = \omega/c$ is the wavevector in free space (commonly referred to as the light line), ϵ_m is the (frequency dependent) dielectric function of the bulk metal, and ϵ_d is the dielectric constant of the adjacent dielectric medium (ϵ_m=1 for air). As they propagate along metallodielectric interfaces, SPPs have evanescently decaying tails both into the metal and the air regions, as illustrated by the plot of the surface normal electric field component provided in fig. 1.2. In practise the propagation length of SPPs is highly geometry and material dependent, taking on values between tens of nanometers to several microns. In experimental setups, the propagation length is limited both by resistive heating in the metal and by scattering induced by metallic imperfections.

One interesting property of k_{SPP} is that it always lies to the right of the light line in a plot of ω versus k_{SPP} (as seen in fig. 1.1). This increase in the wavevector parallel to the surface results in a concomitant increase of the mode confinement perpendicular to the interface (z-direction), since the SPP field amplitude falls off as $e^{-|k_z||z|}$ with $k_z = (k_{\mathrm{SPP}}^2 - \epsilon_{\mathrm{metal}}(\omega/c)^2)^{1/2}$. This property illustrates the potential of SPPs for applications that aim to concentrate electromagnetic energy into sub-wavelength regions. [79]

The fact that k_{SPP} is larger than the free space wavevector poses a challenge when attempting to launch propagating surface plasmons using optical excitation incident from air, as the mode mismatch prohibits direct coupling. Several approaches exist to overcome this mode mismatch: [79]

- **Prism Coupling** can be used to obtain an in-plane wavevector that is large enough to couple to SPPs. Under attenuated total internal reflection, the in-plane wavevector at the lower side of a dielectric prism with dielectric constant ϵ, embedded in a vacuum ($\epsilon = 1$) is $k_{\parallel} = k_0\sqrt{\epsilon}\sin\theta$, which is sufficient to enable mode matching to SPPs.

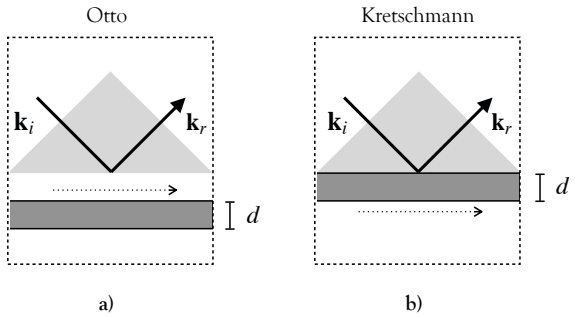


FIGURE 1.3: A dielectric prism is separated from a thin metallic film with a small air gap. In the *Otto* configuration (a), the SPPs (dotted arrow) are excited on the upper side of the metallic film. In the *Kretschmann* configuration (b) the metallic film is deposited directly onto the prism and SPPs are excited on the lower side of this thin film.

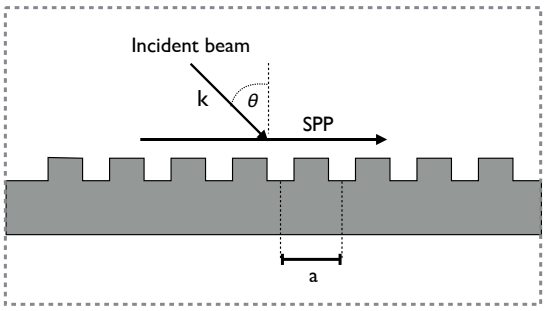


FIGURE 1.4: Excitation of SPPs using a metallic grating with period a. Radiation is incident on the grating at an angle θ and with wavevector k.

Two closely related prism setups, schematically illustrated in fig. 1.3, are commonly used. In the *Otto* configuration [99] a quartz prism is separated from a thin metallic film with a small air gap. The surface plasmon waves are excited on the upper side of the metallic film, where they propagate along the surface. Later on, *Kretschmann* has refined [66] this experimental setup by showing that it is possible to perform SPR measurements even if the film is deposited straight onto the prism, without leaving a thin air gap, which proved to be difficult to realise in laboratory experiments. In the *Kretschmann* configuration the surface plasmon waves (dotted arrow) are excited on the far side of the silver film, where they are propagating along the silver-air interface.

- **Grating Coupling**, illustrated schematically in fig. 1.4, can be used to couple photons into SPPs by increasing the surface parallel wavevector component of free space radiation by an amount related to the grating period a. Mode matching between free space radiation with wavevector k_0 and the SPP wavevector k_{SPP} can be achieved if $k_{\mathrm{SPP}} = k_0 \sin\theta \pm 2n\pi/a$, where $n = 1, 2, 3$, etc.

- **Near field excitation**. The above two schemes can be used to excite SPPs over a diffraction limited macroscopic area. In contrast to this, it is also possible to excite SPPs using near-field microscopy techniques [51], which are able to excite these

modes from regions that are smaller than the diffraction limit. Usually, a small probe of aperture size $a < \lambda_{\mathrm{SPP}} < \lambda_0$ is positioned close to a metallic surface. Due to the small size of its aperture, such a probe will emit radiation with wavevector components $k > k_{\mathrm{SPP}} > k_0$, which establishes a phase-matched excitation of SPPs.

Surface plasmons can be divided into two classes: Surface Plasmon Polaritons (SPPs) (which are some times also called Propagating Surface Plasmonss (PSPs)) and Localised Surface Plasmons (LSPs). Both are characterised by oscillations in the surface electron density, however in the case of LSP this oscillation is caused directly by the Electromagnetic (EM) driving field given by incident light, which in the case of small metallic particles is able to induce a collective oscillation of the surface electron density. At the so called Localised Surface Plasmon Resonance (LSPR) frequency the oscillation of the surface electrons is in phase with the driving field, which results in strong absorption and light scattering into the far field. [79]

In the case of a spherical particle illuminated by light, whose diameter d is much smaller than the wavelength of the incident radiation λ_0, the resultant scattering problem can be accurately described within the quasi-static limit. [16] When $d \ll \lambda_0$ the phase of the harmonically oscillating EM field is almost uniform over the particle volume. Thus, one can consider the simplified problem of a particle in an electrostatic field. Once the spatial field distribution has been determined the harmonic time dependence of the resulting EM fields can then be added back. [16]

We assume a homogeneous isotropic spherical Nano-Particle (NP) of radius $r = a$, located in a uniform static electric field $\mathbf{E} = E_0\hat{\mathbf{z}}$. The surrounding medium is a non-absorbing isotropic dielectric with dielectric constant ϵ_m, and the particle itself is described by a complex valued dielectric constant ϵ. The electric fields can be calculated from the potential ϕ via $\mathbf{E} = -\nabla\phi$ after solving the Laplace equation $\nabla^2\phi = 0$. Thus, introducing the dipole moment $\mathbf{p}$ we can write the potential outside the sphere as [57]

$$\phi_{\mathrm{out}} = -E_0 r\cos\theta + \frac{\mathbf{p}\cdot\mathbf{r}}{4\pi\epsilon_0\epsilon_m r^3} \tag{1.3}$$

$$\mathbf{p} = 4\pi\epsilon_0\epsilon_m a^3 \frac{\epsilon - \epsilon_m}{\epsilon + 2\epsilon_m}\mathbf{E}_0 \tag{1.4}$$

We observe that the applied field induces a dipole moment proportional to $\mathbf{E}_0$ inside the small sphere. If we define the polarisability α of the particle via $\mathbf{p} = \epsilon_0\epsilon_m\alpha\mathbf{E}_0$ this implies the following relation for the complex polarisability for a small metallic sphere of sub-wavelength diameter within the (local) electrostatic approximation [57]

$$\alpha = 4\pi a^3 \frac{\epsilon - \epsilon_m}{\epsilon + 2\epsilon_m} \tag{1.5}$$

This polarisability experiences a resonant enhancement at the condition $\mathrm{Re}[\epsilon(\omega)] = -2\epsilon_m$. This condition is known as the *Frohlich* condition, and the type of this resonance

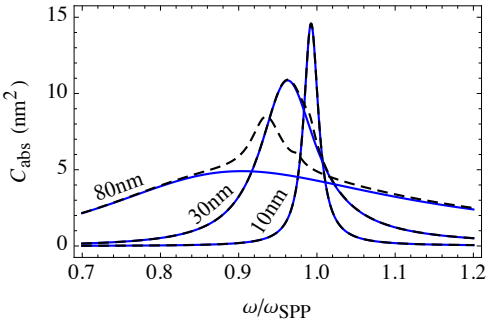


FIGURE 1.5: Absorption cross section C_{abs} for a gold sphere suspended in air, for sphere radii $a = 10$, 30 and 80 nm. Results calculated using the quasi-static approach (solid blue lines) are compared to the full electrodynamic result obtained from *Mie* theory (dashed black lines.)

is referred to as an LSPR. An interesting consequence of the resonant enhancement of the polarisability is the concomitant enhancement of both the absorption (C_{abs}) and scattering (C_{sca}) cross sections of the sphere. These can be calculated as [16]

$$C_{\text{abs}} = k\text{Im}[\alpha] = 4\pi k a^4 \left[\frac{\epsilon - \epsilon_m}{\epsilon + 2\epsilon_m}\right] \tag{1.6}$$

$$C_{\text{abs}} = \frac{k^4}{6\pi}|\alpha|^2 = \frac{8\pi}{3}k^4 a^6 \left[\frac{\epsilon - \epsilon_m}{\epsilon + 2\epsilon_m}\right]^2 \tag{1.7}$$

where $k = 2\pi/\lambda$. For small particles ($a \ll \lambda$) the absorption cross section (which scales with a^3 section dominates over the scattering cross section (which is proportional to a^6). However, for large particles the scattering cross section dominates, which makes it difficult to detect very small particles in an inhomogeneous sample that contains NPs with different diameters.

Figure 1.5 renders the absorption cross section for a gold sphere suspended in air for sphere radii between 10 and 80 nm (solid blue lines) and compares them to a full electrodynamic solution (dashed black lines.) The results of these two approaches begin to diverge significantly starting from a sphere radius of 30 nm, which highlights how the quasi-static formalism is limited in its applicability to sub-wavelength particles illuminated by visible or near-infrared radiation. Typically, for particles with $a > 20$ nm the applicability of the quasi-static approximation no longer holds due to the significant phase change of the driving field over the particle volume. Thus, for these larger particles, a fully retarded electrodynamic solution of the EM fields is required. In the early 20th century, *Gustav Mie* published an analytical solution to *Maxwell*'s equations that provides expressions for the scattering and absorption of light by spherical particles. [88] This solution, which has later been extended to include effects of spatial dispersion [120], agrees with the quasi-static result in the limit $a \ll \lambda$.

1.2 Nonlocality

1.2.1 Conceptual background

Nonlocality is a fundamental concept in physics, and it is by no means limited to electrodynamics. It is related to the way physical fields (electromagnetic and otherwise) interact with each other over a distance and in time. From a mathematical perspective, an observed field $D_{\mathrm{i}}(\mathbf{r}, t)$, where $\mathrm{i} = 1, 2, 3$ and $\mathbf{r}$ denotes the *Euclidean* position vector of the detector and t denotes the time of measurement, can be related to a driving field $E_{\mathrm{i}}(\mathbf{r}', t')$ through a (in general tensorial) response function $f_{\mathrm{ij}}(\mathbf{r}, \mathbf{r}', t, t')$ via [68]

$$D_{\mathrm{i}}(\mathbf{r}, t) = E_{\mathrm{i}}(\mathbf{r}, t) + \int_0^t \mathrm{dt}' \int \mathrm{d}\mathbf{r}' \mathrm{f}_{\mathrm{ij}}(\mathbf{r}, \mathbf{r}', \mathrm{t}, \mathrm{t}') \mathrm{E}_{\mathrm{j}}(\mathbf{r}', \mathrm{t}') \tag{1.8}$$

where the $d\mathbf{r}'$-integral is over all space and where causality restricts the dt' integral to the domain $\{t \in \mathbb{R} | 0 < t' < t\}$. In cases where the integral over this time domain is retained the solution is some times termed a 'retarded' solution.

So far, even though we used symbols familiar from electromagnetics in eq. 1.8, the observable $\mathbf{D}$, its driving field and the response function have been left intentionally general. We do this to illustrate the general nature of eq. 1.8, which constitutes a nonlocal relation that always holds when physical fields interact with each other in space and time. For example, in the context of sound propagation in liquid-saturated porous media, eq. 1.8 some times appears as the following general linear response expression

$$d_{\mathrm{i}}(\mathbf{r}, t) = \int_0^t \mathrm{dt}' \int \mathrm{d}\mathbf{r}' \rho_{\mathrm{ij}}(\mathbf{r}, \mathbf{r}', \mathrm{t}, \mathrm{t}') \mathrm{v}_{\mathrm{j}}(\mathbf{r}', \mathrm{t}') \tag{1.9}$$

where $d_{\mathrm{i}}(\mathbf{r}, t)$ defines an 'acoustic momentum density', $v_{\mathrm{i}}(\mathbf{r}', t')$ is the velocity field of the fluid and $\rho_{\mathrm{ij}}(\mathbf{r}, \mathbf{r}'; t, t')$ is the fluid excess density.

In the context of macroscopic electrodynamics, eq. (1.8) relates the electric field $E_{\mathrm{i}}(\mathbf{r}, t)$ to the displacement field $D_{\mathrm{i}}(\mathbf{r}, t)$ in the metal via a material dependent response function $f_{\mathrm{ij}}(\mathbf{r}, \mathbf{r}', t, t')$, which models effects of polarisation in the metal. However, evaluation of eq. 1.8 in its full form is often impractical for experimentally relevant geometries, because every point $(\mathbf{r}, t)$ is connected to all other points $(\mathbf{r}', t')$, which constitutes a highly coupled system. For this reason, by neglecting the integration in space, a so called local approximation is often made to simplify this relation.

The local approximation may seem like a gross simplification at first glance. However, the reason why such a local approximation is often a valid one to make, is related to the fact that the value of the dielectric response function $f_{\mathrm{ij}}(|\mathbf{r} - \mathbf{r}'|; t)$ decreases rapidly with distances large compared to the interatomic distance. Thus, as long as the effective wavelength ($\sim 1/|\mathbf{k}|$) of a electromagnetic modes is large compared to the interatomic distance spatial dispersion can often safely be neglected, as we will now illustrate.

To see explicitly this dependants on the wavevector $\mathbf{k}(\mathbf{r})$ it is useful to consider the simplifying case of an infinite, macroscopically homogeneous, isotropic medium. In such a medium, the dielectric response tensor only depends on the distance $\rho = |\mathbf{r}-\mathbf{r}'|$ and we may expand the fields E_i and D_i in terms of plane wave Fourier components by mapping the time dependence of the fields into frequency space and the spatial dependence into k- space. In this way, the electric field can be written in the form

$$E_\mathrm{i}(\mathbf{r},t) = \int \mathrm{d}\mathbf{k} \int_{-\infty}^{\infty} \mathrm{d}\omega \ \mathrm{E_i}(\mathbf{k},\omega)\mathrm{e}^{\mathrm{i}(\mathbf{k}\cdot\mathrm{r}-\omega\mathrm{t})} \tag{1.10}$$

With a similar expression for $E_\mathrm{i}(\mathbf{r},t)$. In Fourier space, these plane wave components are related via

$$D_i(\mathbf{k},\omega) = \epsilon_\mathrm{ij}(\mathbf{k},\omega)\ E_\mathrm{j}(\mathbf{k},\omega) \tag{1.11}$$

with

$$\epsilon_\mathrm{ij}(\mathbf{k},\omega) = \delta_\mathrm{ij} + \int_0^t \mathrm{d}\tau \int_{-\infty}^{\infty} \mathrm{d}\rho \ \mathrm{f_{ij}}(\rho,\tau)\ \mathrm{e}^{\mathrm{i}(\omega\tau-\mathrm{k}\rho)} \tag{1.12}$$

and $\tau = t - t'$. This description is useful because it reduces nonlocality to a dependance on the wavevector $\mathbf{k}$, or equivalently the effective wavelength of electromagnetic modes, which is proportional to $1/|k|$. We see immediately that in the long wavelength limit where $|\mathbf{k}| \to 0$ the $\mathbf{k}$-dependence disappears and eq. 1.12 reduces to a purely local description, where $\epsilon_\mathrm{ij}(\omega)$ is a function of frequency only. The specific requirement for the local approximation of the response function ϵ to hold is that $kr_0 \ll 1$, where r_0 defines the region where the kernel of eq. (1.12) is significantly greater than zero. [68] There are several models that are commonly used to describe this local dielectric function for metals, and in section 2.3.1 we give a derivation of the *Drude* model as one of the most intuitive schemes that are commonly used in the context of plasmonics.

1.2.2 Experiments

The exploration of nonlocal effects in metallic nanostructures can be approached either using experimental or using theoretical techniques, with both approaches informing each other. Fore example, sensitive experiments can be performed that probe the electronic response of metallic structures in geometries where nonlocal effects are expected to be significant. The impact of nonlocality can then be estimated by comparing these experimental results to both local and nonlocal models.

One geometry that exhibits nonlocal effects experimentally is given by ultra thin metallic films with thicknesses in the sub 10 nm regime. Thin metallic films are unusual because of the importance of longitudinal polarisation modes on the surface [72]. Beyond the local approximation, inelastic light scattering can excite these modes, in addition to the usual transverse surface plasmon modes that occur within the local approximation. The emergence of longitudinal waves leads to additional absorption, which manifests itself in

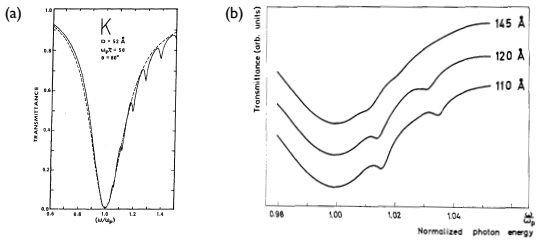


FIGURE 1.6: (a) Theoretical nonlocal (solid line) and local (dashed line) transmittance spectrum for p-polarized light incident on a 52 Angstrom thick potassium film. Adapted from Ref. [87] (b) Transmittance spectra of a thin silver film for p-polarized light and for three different film thicknesses, 110, 120 and 145 Angstrom. The angle of incidence is 75deg. Adapted from Ref. [72] Copyright 1971 by the Royal Swedish Academy of Sciences. Reproduced by permission of IOP Publishing. All rights reserved.

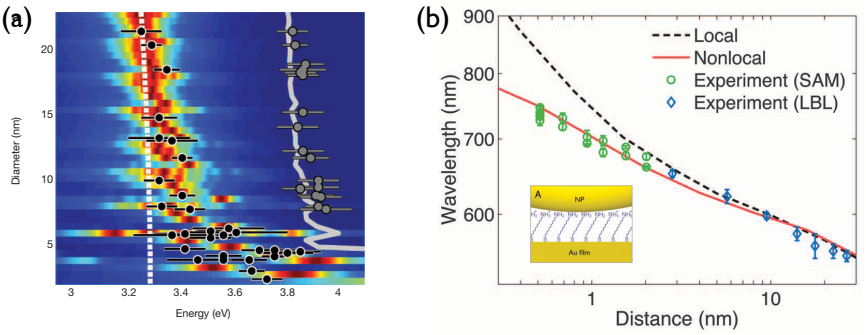


FIGURE 1.7: (a) Experimental results for small metal spheres. Comparison of experimental data with quantum theory for Ag NPs ranging in diameter from 20 nm to less than 2 nm are reproduced. Experimental, EELS-determined localized surface plasmon resonance energies of various particle diameters are plotted on the absorption spectra generated from an analytic quantum permittivity model. The experimental bulk resonance energies (grey dots) together with the theory predictions (grey line) are also plotted. The local *Mie* theory peak prediction is given by the dashed white line. Adapted from Ref. [128] (b) Experimental results for a coupled NP-film system. The trace of the surface plasmon scattering peak as a function of particle-film separation is reproduced. Experimental results (markers) are compared with results from theoretical nonlocal (solid red line) and local (dashed black line) calculations. Adapted with permission from Ref. [23] Copyright 2012 by The American Association for the Advancement of Science.

a resonant set of absorption induced dips in the transmittance, as illustrated in fig. 1.6. This behaviour was predicted in theoretical results, reproduced in fig. 1.6 (a), obtained by *Melnyk et al.* [87] and experimental verification of this effect was provided by *Lindau et al.* in 1971 [72] (see reproduced experimental curves in fig. 1.6 (b)). More recent Finite Difference Time Domain (FDTD) results also corroborate this behaviour. [84]

Another geometry that is expected to exhibit nonlocal effects are diminutive Nano-Particles (NPs). In 2007 *Palomba et al.* [104] deposited size-selected Au nanoparticles on transparent substrates. In their study, interferometric optical detection measurements obtained using a supercontinuum laser source has indicated a blue-shifted plasmon resonance at the single particle level, which they attributed to nonlocal effects.

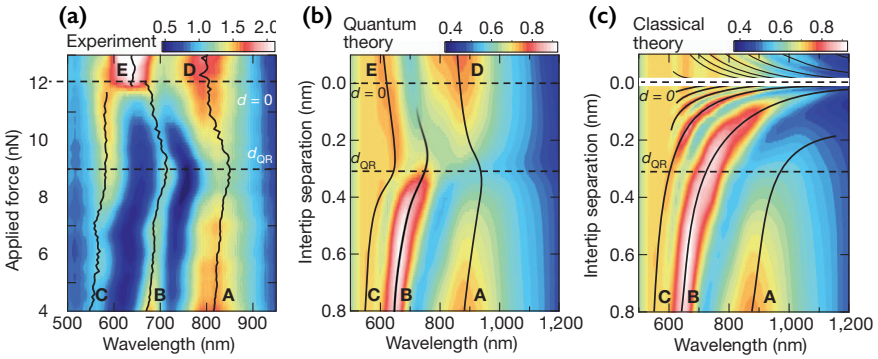


FIGURE 1.8: Onset of quantum tunnelling in sub-nm plasmonic cavities. (a) Measured dark-field optical back-scattering with increasing force applied to the inter-tip cavity (decreasing inter-tip cavity size). The onset of the quantum regime is marked at d_{QR}. (b) Theoretical total scattering intensity from a tip-tip system incorporating quantum mechanical tunnelling. (c) Theoretical scattering intensity as in (b) but using purely classical calculations. Adapted with permission from Ref. [125] Copyright 2012 by Nature Publishing Group.

A particularly promising technique for the investigation of sensitive plasmonic effects is Electron Energy Loss Spectroscopy (EELS). In 2012, *Scholl et al.* [128] revealed the quantum plasmon resonances of individual silver nanoparticles of controlled sizes between 20 nm to less than 2 nm (see experimental data points reproduced in fig. 1.7 (a)). Their study showed experimentally the significant blue-shifting of the Localised Surface Plasmon Resonance (LSPR) in silver nanoparticles below a diameter of 10 nm that occurs as a result of spatial dispersion. Excellent agreement with a Density Functional Theory (DFT) simulation for the geometry was also obtained. In 2013, *Raza et al.* [116] used EELS in a similar study to show how spatial dispersion leads to a blue-shifted LSPR in silver nanoparticles in the diameter range 26 down to 3.5 nm.

In 2012, *Ciraci et al.* [23] combined the above two geometries, demonstrating the impact of nonlocality in film coupled gold nanoparticles. In their experiment the distance between the film and the nanoparticles was chemically controlled, which enabled *Ciraci* and coworkers to confirm experimentally how spatial dispersion leads to blue-shifted plasmon resonances when compared to local predictions, as illustrated in fig. 1.7 (b). They also emphasised the limits in field enhancements that come as a result of nonlocality, imposing ultimate limitations on a wide range of nonlinear and quantum optical phenomena.

One characteristic that is shared by all experiments investigating nonlocality is the small length scale on which metallic samples are shaped. For example, the film coupled nanoparticles studied by *Ciraci et al.* [23] had characteristic gap thicknesses in the sub nanometer regime, which were achieved using a carefully controlled carbon spacer layer. One question that arises in this context is around the onset of electronic tunnelling effects in these nearly touching metallic nanoparticle configurations.

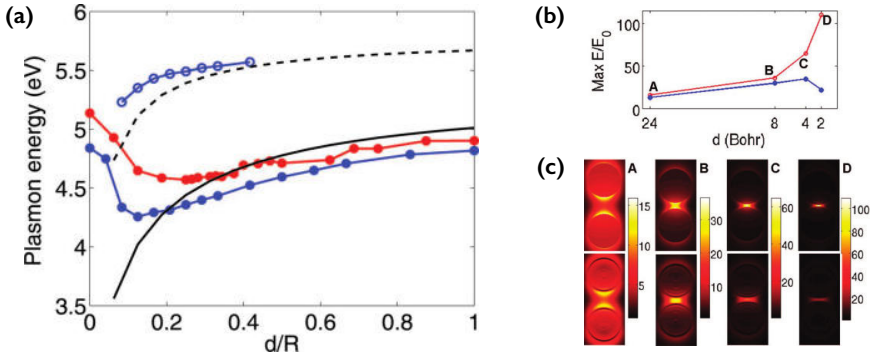


FIGURE 1.9: Theoretical TDLDA results for a diminutive metallic dimer. (a) The dipolar (full circles) and quadrupolar (open circles) dimer plasmon energy as a function of the radius normalised diameter d/R, for of radius $R = 16$ (red) and 24 *Bohr* radii (blue) sphere dimers calculated using TDLDA. The local result is rendered with solid (dipolar) and dashed (quadrupolar) lines. (b) Trace of the maximum electromagnetic field enhancements calculated using the local theory (red) and TDLDA (blue) for spheres with radius $R = 24$ *Bohr* radii forming dimers of separations $d = 24$ (A), 8 (B), 4 (C), and 2 *Bohr* radii (D). (c) Field distributions calculated using local theory (top panels) and TDLDA (bottom panels). Adapted with permission from Ref. [156] Copyright 2009 by the American Chemical Society.

A notable experimental study that aims to answer this question was conducted in 2012 by *Savage et al.*. [125] By simultaneously measuring both the electrical and optical properties of two gold tips with controllable subnanometre separation, *Savage et al.* were able to estimate the onset of quantum tunnelling effects in this geometry to occur at a gap distance of 0.3 nm, see experimental and theoretical results reproduced in fig. 1.8.

1.2.3 Quantum theories

Theoretical models that include the nonlocal nature of the electromagnetic response of metals can be obtained in a variety of ways, and trade-offs in accuracy, physical insight, and computational cost have to be considered. The highest level of accuracy is generally achieved by first principles calculations, which are based on full quantum mechanical solutions. These approaches are viable for small system sizes and in principle they model the full complexity resultant not only from nonlocal effects but also from other quantum effects, such as quantum tunneling.

Time-Dependent Density Functional Theory (TDDFT) offers a way to study the temporal evolution of plasmons at the nanoscale from first principles. For example, *Zuloaga* and co-workers used a TDLDA model to treat the ground state of atoms in small metal clusters separated by a nanometric gap using a jellium model [156]. Dimers of metal spheres with radii as large $R = 2.5$ nm were considered. The principle findings of this study are twofold: First, as the distance between spheres is decreased from 24 to 2 Bohr radii, the maximum field achieved in the gap reaches a maximum in the quantum

simulations around a gap distance of 4 Bohr radii (~ 0.2 nm) whereas it reaches a maximum value in the touching limit in the local model (see reproduced theoretical results in fig. 1.9 (a)). Second, the study also identified a saturation of the redshift experienced by the dipolar dimer plasmon resonance energy with decreasing separation distance. Local models predict this quantity to redshift without an inflection point as the interparticle distance is decreased. In contrast to this, as illustrated in fig. 1.9 (b), *Zuloaga et al.* found a redshifting of the dipolar dimer plasma mode down to separation distances of $\sim 0.1R$, after which a blueshifting of the mode was observed as the distance between spheres was further decreased.

Another recent study where static polarisabilities and optical absorption spectra of gold clusters was calculated using a first principles approach is by *Idrobo* and co-workers. [56] Stable gold cluster sizes as large as 20 atoms were considered.

The *Zuloaga* and *Idrobo* studies highlight one of the major limitations of first principles quantum mechanical solutions, namely the restricted system size regime that can be investigated with such methods. Even though nanofabrication techniques are continuously improving, with feature sizes in the nanometre [23] and even sub-nanometre regime [125], in general the overall size of plasmonic systems that are of interest to experimentalists still span tends to thousands of nanometres, making the use of first-principles approaches impractical.

1.2.4 Meso-scale theories

After experimental and full-quantum approaches, a third avenue of investigation of nonlocal effects in plasmonics is offered by meso-scale solutions, which are parametrised using quantum mechanical models. This class of solutions offers access to much larger system sizes, at the expense of being quantitatively accurate or generally applicable.

The size limitations of first-principles simulations have lead to the development of so called meso-scale models. These often employ the use of continuum equations that are calibrated using results from first principles simulations. They then allow for the investigation of much larger systems, whilst retaining selected physical effects from higher accuracy simulations.

For example, the quantum corrected model [32] has recently been introduced by *Esteban* and co-workers to investigate quantum tunnelling in systems spanning hundreds of nanometres in size. Summarised in fig. 1.10, the model defines an effective dielectric function for the tunnelling gap, with a damping-like fitting parameter that is calibrated by the use of full-quantum simulations.

The remaining parts of this thesis will focus entirely on meso-scale approaches, where we will show how the hydrodynamical *Drude* model can be used effectively as a nonlocal

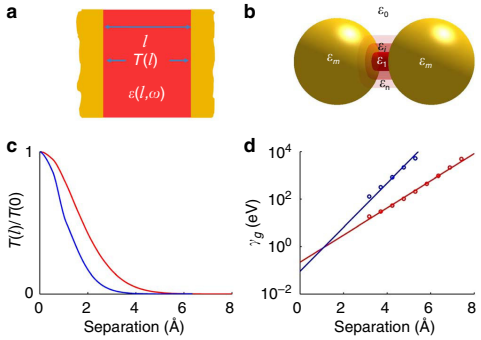


FIGURE 1.10: Illustration of the quantum corrected model. (a) A simple plasmonic system composed of two semi-infinite planar interfaces separated by a distance l is used to obtain a characteristic tunnelling transmission $T(l)$. The tunnelling-induced conductivity between these surfaces defines an effective separation-dependent dielectric material $\epsilon(l,\omega)$ used in the quantum corrected model. (b) In the case of a metallic dimer (schematically depicted) ϵ_i, obtained in the previous step, is used as a separation-dependent dielectric constant of the shells of fictitious material that accounts for the quantum tunnelling. A number of shells (i = 1,...,n) are used. (c) The normalized electron tunnelling transmission $T(l)/T(0)$ and (d) tunnelling damping γ_g is plotted as a function of the separation distance l. In both (c) and (d), red corresponds to a Na jellium material, and blue to a Au jellium. Adapted with permission from Ref. [32] Copyright 2012 by Nature Publishing Group.

mesoscale solution to tackle a range of experimentally relevant geometries, from kissing cylidnders to plasmonic tip waveguides.

Chapter 2

Theory

In this chapter we introduce the theory background and simulation techniques that form the basis of the studies presented in chapter 3 of this Thesis. We begin by introducing classical electromagnetics in a general way, and then proceed to describe how material properties enter the description through the use of material specific dielectric functions. In this context, different methods of encoding material properties in dielectric functions are discussed, ranging from a simple local *Drude* function to a nonlocal hydrodynamical transport equation for the electron current. After motivating the choice of this hydrodynamic model for the treatment of nonlocal effects, we show how it can be used to study the electromagnetic response of plasmonic systems both analytically, as well as numerically using a finite element method. We conclude the chapter by outlining a reliable computational algorithm for calculating dispersion relations, which will be used frequently in the remaining parts of this thesis.

2.1 Electrodynamics

On the atomic level, plasmonic materials are described by quantum mechanics. However, in many cases that are of practical interest to experimentalists, the *Maxwell*'s equations provide an adequate description. For many length scales, such as those characteristic of a laser beam propagating in free space with effective wavelength around 1 micron, or a 500 nm radius spherical gold nanoparticle suspended in a dielectric environment such as oil, analytical solutions of *Maxwell*'s equations give an accurate description of the underlying physics, provided that there are no sharp corners or nearly touching particles. [32]

In this context, after separating external and internal charges and currents, electromagnetic phenomena can be described by the set of four macroscopic *Maxwell*'s equations [79]

$$\nabla \cdot \mathbf{D} = \rho_{\text{ext}} \tag{2.1a}$$

$$\nabla \times \mathbf{H} = \mathbf{J}_{\text{ext}} + \frac{\partial \mathbf{D}}{\partial t} \tag{2.1b}$$

$$\nabla \cdot \mathbf{B} = 0 \tag{2.1c}$$

$$\nabla \times \mathbf{E} = -\frac{\partial \mathbf{B}}{\partial t} \tag{2.1d}$$

Where ρ_{ext} and $\mathbf{J}_{\text{ext}}$ are the external charge and current densities, respectively, $\mathbf{E}$ and $\mathbf{D}$ are the macroscopic electric field and macroscopic displacement field, respectively, $\mathbf{B}$ and $\mathbf{H}$ are the macroscopic magnetic field and macroscopic magnetising field, respectively, and t denotes time. Note that according to this definition we distinguish between external quantities which drive the system (ρ_{ext}, $\mathbf{J}_{\text{ext}}$) and internal quantities that respond to the external stimuli (ρ, $\mathbf{J}$). Thus, the total charge and current densities are given by $\rho_{\text{tot}} = \rho_{\text{ext}} + \rho$ and $\mathbf{J}_{\text{tot}} = \mathbf{J}_{\text{ext}} + \mathbf{J}$, respectively. [81]

The macroscopic form of these equations implies that $\mathbf{E}$ and $\mathbf{D}$, and $\mathbf{B}$ and $\mathbf{H}$, are related through the following (nonlocal) relations

$$\mathbf{D}(\mathbf{r}, \omega) = \epsilon_0 \int \mathrm{d}\mathbf{r}' \epsilon(\mathbf{r}, \mathbf{r}', \omega) \mathbf{E}(\mathbf{r}', \omega) \tag{2.2a}$$

$$\mathbf{B}(\mathbf{r}, \omega) = \mu_0 \int \mathrm{d}\mathbf{r}' \mu(\mathbf{r}, \mathbf{r}', \omega) \mathbf{H}(\mathbf{r}', \omega) \tag{2.2b}$$

where (ϵ_0) ϵ and (μ_0) μ are the (vacuum) permitivity and permeability, respectively.

When combined with appropriate boundary conditions, the combination of Newton's second law of motion, the *Lorentz* force equation, eqs. (2.1) and (2.2) provide a complete description of the classical dynamics of charged particles interacting with electromagnetic fields. [57]

The nonlocal characteristics of eq. (2.2) have already been touched upon in section 1.2. The boundary conditions required to obtain a closed form solution of eq. (2.1) in the local limit are well known: continuity of the parallel components of the electric and magnetic fields fully specify the system in the local limit. [57] On the other hand, as we will show in section 2.3.3, once nonlocal effects are considered a third boundary condition is required.

2.2 The finite element method

Closed form analytical solutions to *Maxwell*'s equations are only known for certain special geometries. These include infinite surfaces, spheres, cylinders and their arrays [68; 89]. However, advances in nano-fabrication have lead to interest in the electromagnetic properties of structures with more complex shapes. In recent years, numerical techniques for the solution of *Maxwell*'s equations in such systems [59; 136] have become feasible as a result of increasing computational power.

In this context, the Finite Element Method (FEM) offers a powerful numerical technique for the solution of arbitrary Partial Differential Equation (PDE) and integral equation based boundary value problems, both in frequency and time domain. The method has emerged in the 1940s and 1950s, when it was used initially for aircraft design. However, the general nature of FEM means that it has been used since in problem domains spanning multiple disciplines, including radio frequency analysis, structural mechanics, heat propagation, laminar and turbulent fluid flows, and acoustics. Another powerful application of FEM comes in its ability to bridge different problem domains by coupling together the equation systems that govern them. One particularly successful software platform implementing the above problem domains and many more, as well as the ability to obtain standalone and coupled solutions thereof, is *Comsol Multiphysics*.[1] Besides providing already implemented versions of sets of equations and boundary conditions commonly used in physics and engineering, this commercial software package also allows the user to specify arbitrary sets of coupled PDE, together with a variety of flexible boundary conditions. An open source alternative to *Comsol Multiphysics* is the *Elmer FEM solver*[2].

FEM poses a suitable avenue for the solution of *Maxwell*'s equations (eq. (3.18)) in cases where analytical solutions are infeasible. The method solves the fields in the frequency domain, assuming an $e^{i\omega t}$ frequency dependence of the fields. This limitation makes the method unsuitable for the analysis of nonlinear phenomena, where the interaction of photons with different energies needs to be modelled. That said, in the absence of nonlinear effects, FEM is particularly well suited for the treatment of multi-scale problems, as it is based on a discretisation of the computational domain into finite elements, on which the solutions are specified using so called shape functions. The flexibility of the method comes from the users ability to choose finite element geometries that go beyond a simple rectangular grid arrangement. For example, in Two-Dimensional (2D) systems, meshing algorithms that lead to a triangular mesh can be used, providing a discretisation of the computational domain that can efficiently adapt to the sub-nanometric features that are crucial for the physics of many challenging plasmonic systems, such as

[1] http://www.comsol.com
[2] http://www.csc.fi/english/pages/elmer

the narrow gaps that are formed between infinitely long kissing nanowires. [71] Similarly, in Three-Dimensional (3D) geometries, tetrahedral meshes can be used to resolve accurately the rapidly varying Electromagnetic (EM) solutions between kissing metallic spheres [35] and at the apex of sharp plasmonic tips. [148] In all these cases, it is necessary to resolve the solutions to the problems under study over a computational domain that includes regions where the slope of these solutions changes sign several times over the span of less than 1 nm, and other regions where their effective wavelength is of the order of 1 μm or more (far field radiation/illumination regions). The adaptive meshing algorithms commonly used in FEM are able to efficiently bridge both these physical regimes.

A comprehensive introduction to the theoretical underpinnings and applications of FEM in the context of electromagnetics is given by *Jin*. [59]

2.3 Dielectric functions

Once a suitable solution strategy for *Maxwell*'s equations (eq. (2.1)) has been chosen for a given problem geometry, it is necessary to inject the electromagnetic material properties into the model via the response functions in eq. (2.2). In this thesis we usually assume a non-magnetic material, which implies a magnetic permeability that is characterised by $\mu = 1$. On the other hand, the form of the electric permittivity ϵ is in general more complicated, taking a constant real value proportional to the refractive index for dielectric media, and incorporating non-vanishing imaginary parts once the damping that occurs in polarisable media is taken into account. In this section we begin by introducing a simple *Drude* dielectric function appropriate for metals such as silver, and conclude by presenting an extension to the *Drude* description that incorporates nonlocal response.

2.3.1 Drude dielectric function

Out of all the approaches used to describe the electromagnetic material properties of metals today, one of the simplest, and yet surprisingly accurate, models was proposed over 100 years ago by *Paul Drude*, who used it to describe the dynamics of free electrons. [26; 27] The introduction of this so called "*Drude* model" that we provide in this section will serve as a basis for extensions that will be introduced in later sections to more accurately treat the electron dynamics in metals.

The *Drude* model, which we here summarise following the treatment by *Ashcroft and Mermin* [6] treats metals as a dense gas of electrons of charge $-e$[3], undergoing ballistic scattering when they encounter protons of equal but opposite charge, which are assumed

[3] We define the charge e to be a positive number

to be stationary. In addition to the assumption that protons are fixed scattering targets for the electrons, the *Drude* model is built on the following assumptions:

1. Independent electron approximation. Electrons are taken to only interact during collisions. When they are not touching, electrons are assumed to follow, a straight line trajectory governed by Newton's second law of motion, which is only diverted if electrons are deflected by an external field. Similarly, electron-ion interactions are neglected (free electron approximation).

2. Collisions between electrons and ions are assumed to be instantaneous events that alter the path of electrons, with all scattering directions being equally likely. The exact mechanism of the collision is ignored, but the mean free time between collisions for an electron is assumed to be τ, thus the probability of a collision per unit time is $1/\tau$.

3. The speed of electrons after collisions is chosen to maintain local thermal equilibrium.

The current density vector $\mathbf{j} = -ne\mathbf{v}$ for an electron density n points in the direction of the flow of charge, and its magnitude gives the amount of charge that is flowing per unit time through a unit area situated perpendicular to this flow. If no external field is applied to a metal, the distribution of electron charge velocity vector directions $\mathbf{v}$ will be random and so the net charge density will be zero. In the presence of a spatially homogeneous Direct Current (DC) external electric field $\mathbf{E}$ the change in the velocity that an electron experiences between collisions is related to the acceleration it experiences between collisions from the external electric field. The *Drude* model assumes that electrons emerge from a collision in a random direction, so the average velocity of electrons is given by on $v_{\text{avg}} = -e\mathbf{E}\tau/m_e$. Thus we can relate $\mathbf{j}$ and $\mathbf{E}$ via

$$\mathbf{j} = \sigma\mathbf{E} \tag{2.3}$$

where we have defined

$$\sigma_0 = \frac{ne^2\tau}{m_e} \tag{2.4}$$

as the *Drude* DC conductivity[4].

Next, we derive an equation for the electron dynamics in the presence of (spatially homogeneous) time varying electromagnetic fields. Noting that the average velocity per electron is $\mathbf{v} = \mathbf{p}/m$ we can write the current density as

$$\mathbf{j}(t) = -ne\frac{\mathbf{p}(t)}{m_e} \tag{2.5}$$

[4]In the general case where the current and the electric field are not parallel σ will be a tensor

To arrive at an equation of motion of the electrons, we now calculate the momentum of an electron with momentum $\mathbf{p}(t)$ after an infinitesimal time dt later. The probability of an electron to undergo a collision after time dt is dt/τ, and after the collision the electron will emerge at a random direction, with average momentum zero in the absence of an external force, and with momentum $\mathbf{f}(t)dt + O(dt)^2$ in the presence of an external electromagnetic force $\mathbf{f}$. Similarly, the probability of an electron to travel for a time dt without collision is $1 - dt/\tau$, and the momentum the electron has acquired after this interval is $\mathbf{p}(t) + \mathbf{f}(t)dt + O(dt)^2$. Putting these two together, and retaining only terms to first order in dt, we obtain

$$\mathbf{p}(t + dt) = \mathbf{p}(t) - \frac{dt}{\tau}\mathbf{p}(t) + \mathbf{f}(t)dt + O(dt)^2 \tag{2.6}$$

Rearranging and dividing by dt, this equation becomes

$$\frac{d\mathbf{p}(t)}{dt} + \frac{\mathbf{p}(t)}{\tau} = \mathbf{f}(t) \tag{2.7}$$

The force term on the right hand side includes in its simplest form the *Lorentz* force resulting from an external electromagnetic field

$$\mathbf{f}(t) = -e(\mathbf{E} + \mathbf{v} \times \mathbf{B}) \tag{2.8}$$

but we note here that in principle it could include other forces acting on the electrons, such as a pressure force resulting from inhomogeneities in the electron gas, as we will discuss later in the context of spatial nonlocality. We also note that the magnetic term can usually be ignored because it is by a factor $v/c \sim 10^{-10}$ smaller than the electric field, based on the assumption of a typical electron drift velocity of 0.1 cm/sec. [6]

Eq. 2.4 gives the *Drude* conductivity for spatially and temporally homogeneous fields. Relaxing the second of these two assumptions, we now allow for a time harmonic electric field of the form $\mathbf{E}(t) = Re[\mathbf{E}(\omega)e^{-i\omega t}]$. Thus, we can Fourier transform Eq. 2.7 to obtain an equation of the form

$$\mathbf{j}(\omega) = \sigma(\omega)\mathbf{E}(\omega) \tag{2.9}$$

where we have defined the *Drude* Alternating Current (AC) conductivity as

$$\sigma(\omega) = \frac{\sigma_0}{1 - i\omega\tau} \tag{2.10}$$

Eq. 2.10 was derived under the assumptions of a negligible magnetic field and a spatially homogeneous electric field. Assessing now the suitability for this equation to be used in modelling electromagnetic waves in metals, we note that even though the first assumption (negligible magnetic field) is justified, the assumption of a spatially homogeneous electric field poses a more serious problem. This is because the electric field in

plasmonic structures is in general not uniform, as a result of surface and bulk electromagnetic modes which, depending on geometry, are often deep subwavelength.

One of the fundamental assumptions of the *Drude* model is that collisions modify the directions of electrons in a stochastic way, so that the average momentum of an electron is zero after a collision. For this reason, an external electric field can only modify the electron dynamics during the time period τ in between collisions, a time that characterises the mean free path of the electron. Thus, as long as the electric field is constant over distances comparable to the mean free path (~ 0.1 nm in noble metals such as gold or silver [6]) the assumption of a spatially homogeneous field is justified even for fields that may not be spatially homogeneous on a larger length scale. This is a reassuring result, as it confirms that nonlocal effects emerge only due to charge fluctuations that occur inside the length scale set by the *Fermi-Thomas* wavelength (~ 0.1 nm for noble metals [6].) The *Fermi-Thomas* wavelength gives the distance beyond which charge disturbances are screened effectively, and therefore it is a key magnitude in determining the impact of nonlocality in plasmonic devices.

Thus, given the proviso of an effective Electromagnetic (EM) wavelength that remains large compared with the *Fermi-Thomas* wavelength, we can include a spatial dependence in eq. (2.9), which then reads

$$\mathbf{j}(\mathbf{r},\omega) = \sigma(\omega)\mathbf{E}(\mathbf{r},\omega) \tag{2.11}$$

It is in cases where the assumption of a constant electric field over distances comparable to the *Fermi-Thomas* screening length is no longer justified that we need to resort to a nonlocal description.

For the moment we proceed under the local assumption, combining *Maxwell*'s equations (Eq. 2.1) and eq. (2.11) to give the *Maxwell* wave equation

$$\nabla^2\mathbf{E}(\mathbf{r},t) = -\frac{\omega^2}{c^2}\epsilon(\omega)\mathbf{E}(\mathbf{r},t) \tag{2.12}$$

with

$$\epsilon(\omega) = 1 - \frac{4\pi i\sigma(\omega)}{\omega} \tag{2.13}$$

Or equivalently, using eq. (2.4) and eq. (2.10)

$$\epsilon(\omega) = 1 - \frac{\omega_p^2}{\omega(\omega + i\gamma)} \tag{2.14}$$

In summary, we have introduced the *Drude* model and the central assumptions on which it is based, namely the independent electron approximation, the free electron approximation, and ballistic scattering in a random direction of the electrons after a mean free path characterised by the time interval τ. Importantly, we have shown how

the latter gives an intuitive bound for the applicability of the local approximation in electromagnetics, which, at least in the context of the *Drude* model, is valid as long as the electromagnetic fields do not vary significantly over distances comparable to the *Fermi-Thomas* wavelength.

2.3.2 Hydrodynamic model

The *Drude* model for the dynamics of free electrons in metals, summarised in section 2.3.1, is limited in several ways. Importantly, it is only able to provide a good fit with experimental data in energy ranges where the electronic response is governed by quasi-free conduction electrons, as it does not include terms that take into account energy dissipation associated to inter-band transitions, which for gold begin already in the visible spectrum. Fortunately, this limitation is not detrimental for the applicability of the *Drude* model in plasmonics, as there are numerous cases where inter-band transitions are not significant in the energy range of interest. One such case is silver, where the *Drude* model is able to give a remarkably close fit to experimental data (see Appendix 1) for energies across the visible spectrum and almost up to the surface plasma frequency (given by the condition $\mathrm{Re}[\epsilon(\omega)] = -1$)

Another limitation of the *Drude* model is that it was derived within the local approximation. This approximation begins to no longer hold once electric fields begin to vary over spatial length scales comparable to the *Fermi-Thomas* wavelength (~ 0.1 nm in noble metals such as gold or silver.) In the simplest picture, this length scale sets the average distance among electrons in the conduction band. In this section we present one commonly used approach to address this limitation by introducing a new term into the equation for the *Drude* free electron dynamics, with the aim of capturing the phenomenology introduced by nonlocality (or spatial dispersion.)

In the hydrodynamic model, the force term in the equation of motion for the free electrons (with number density n) no longer only consists of the *Lorentz* force, but now also contains a term for the pressure p, added to capture the inhomogeniety of n. This pressure emerges from the fermionic nature of electrons, which prevents them from occupying the same quantum state and leads to an effective interaction among electrons. With this addition, eq. (2.7) becomes [14; 130; 126]

$$m_e\ddot{\mathbf{x}} + m_e\gamma\dot{\mathbf{x}} = -e(\mathbf{E} + \dot{\mathbf{x}} \times \mathbf{B}) - \frac{\nabla p}{n} \tag{2.15}$$

where $\dot{\mathbf{x}} = \dot{\mathbf{x}}(\mathbf{r}, t) = \mathbf{v}(\mathbf{r}, t)$ is the electron fluid velocity, n is the local number density of electrons, m_e is the mass of the electrons, and $\gamma = 1/\tau$ is the *Drude* damping coefficient. The field and electronic position vectors are assumed to have a harmonic time dependence with the fields, i.e. $\mathbf{x}(\mathbf{r}, t) = \mathbf{x}_0(\mathbf{r})e^{-it\omega}$ and $\mathbf{E}(\mathbf{r}, t) = \mathbf{E}_0(\mathbf{r})e^{-it\omega}$. The final term on the right hand side of eq. (2.15) captures the inhomogeneity in the density

of the electron gas. Specifically, ∇p introduces the *Fermionic* character of electrons, which implies a spread in kinetic energy of electrons that leads to a non-vanishing rate of change in the average local electron velocity. Our aim is to rewrite ∇p in terms of quantities that will allow us to evaluate eq. (2.15) in the context of *Maxwell*'s equations, which means expressing it in terms of one of the electromagnetic fields or currents. In the following, we assume that $p(r,t)$ $(n(r,t))$ consist of a homogeneous, static part p_0 (n_0), and a small out of equilibrium contribution δp (δn), which is a function of r and t. Thus, we can write [126]

$$\nabla p = \frac{\partial \delta p}{\partial \delta n} \nabla \delta n \tag{2.16}$$

In this context the nonlocality parameter β is commonly defined as [50]

$$\beta^2 = \frac{1}{m_e} \frac{\partial \delta p}{\partial \delta n} \tag{2.17}$$

In a free electron gas, the continuity equation for the electron density reads

$$\dot{n}_e(\mathbf{r},t) + \nabla[n_e(\mathbf{r},t)\dot{\mathbf{x}}(\mathbf{r},t)] = 0 \tag{2.18}$$

Inserting the first order expansion of n we obtain

$$\frac{d(n_0 + \delta n(\mathbf{r},t))}{dt} + \nabla \cdot [(n_0 + \delta n(\mathbf{r},t))\dot{\mathbf{x}}(\mathbf{r},t)] = 0 \tag{2.19}$$

However, assuming that the electron density varies more slowly than the electron velocity both in space and in time (we keep only lowest order correction in the electron density distribution), and making use of our earlier assumption that the background electron density is assumed to be homogeneous in space and time, this reduces to

$$\delta n(\mathbf{r},t) + n_0 \nabla \cdot [\mathbf{x}(\mathbf{r},t)] = 0 \tag{2.20}$$

Inserting eq. (2.20) into eq. (2.15) using eq. (2.16) we obtain

$$m_e \ddot{\mathbf{x}}(t) + m_e \gamma \dot{\mathbf{x}}(t) = -e(\mathbf{E} + \mathbf{v} \times \mathbf{B}) + \beta^2 m_e \nabla \cdot [\nabla \mathbf{x}] \tag{2.21}$$

Defining a current $\mathbf{J} = -en\dot{\mathbf{x}}$ which is time harmonic ($\mathbf{J}(\mathbf{r},t) = \mathbf{J}_0(\mathbf{r})e^{-it\omega}$), and neglecting magnetic effects, we obtain the nonlocal transport equation for the electron current

$$\beta^2 \nabla \cdot [\nabla \mathbf{J}] + \omega(\omega + i\gamma)\mathbf{J} = i\epsilon_0 \omega \omega_P^2 \mathbf{E} \tag{2.22}$$

where the bulk plasma frequency is defined as $\omega_P^2 = e^2 \epsilon_0 n_e / m_e$.

Equation (2.22) can be solved simultaneously with *Maxwell*'s equations using a variety of methods, including Finite Element Method (FEM) and analytical approaches. For analytical solutions, it is convenient to derive longitudinal and transverse dielectric

function components implied by eq. (2.21). To this end, we perform a *Fourier* transform of eq. (2.21) into k-space using the convention $\mathbf{f}(\mathbf{k},t) = \int d\mathbf{r}\ \mathbf{f}(\mathbf{r},t)e^{-i\mathbf{k}\cdot\mathbf{r}}$. Ignoring magnetic effects, we obtain [24]

$$\omega\left(\omega\mathbf{x} + \gamma i\mathbf{x}\right) - \beta^2\mathbf{k}\cdot(\mathbf{k}\cdot\mathbf{x}) = \frac{e}{m_e}\mathbf{E} \tag{2.23}$$

Thus, if $\mathbf{k}$ is parallel to $\mathbf{E}$ (longitudinal EM waves) the polarisation field, defined as $\mathbf{P} = -en\mathbf{x}$, becomes

$$\mathbf{P}_{\text{long}} = -\frac{\epsilon_0\omega_P^2}{\omega(\omega + i\gamma) - \beta^2k^2}\mathbf{E} \tag{2.24}$$

On the other hand, if $\mathbf{k}$ is perpendicular to $\mathbf{E}$ (transverse EM waves) the polarisation field reduces to the usual local result

$$\mathbf{P}_{\text{trans}} = -\frac{\epsilon_0\omega_P^2}{\omega(\omega + i\gamma)}\mathbf{E} \tag{2.25}$$

Therefore, after relating the polarisation field $\mathbf{P}$ to the displacement field $\mathbf{D}$ via $\mathbf{D} = \epsilon_0\mathbf{E} + \mathbf{P}$, with $\mathbf{D} = \epsilon\mathbf{E}$, we can extract the longitudinal and transverse elements of the dielectric tensor as

$$\epsilon_{\text{long}} = \epsilon_0 - \frac{\epsilon_0\omega_P^2}{\omega(\omega + i\gamma) - \beta^2k^2} \tag{2.26}$$

$$\epsilon_{\text{trans}} = \epsilon_0 - \frac{\epsilon_0\omega_P^2}{\omega(\omega + i\gamma)} \tag{2.27}$$

2.3.3 Additional boundary conditions

In the local limit, solutions to *Maxwell*'s equations can be found by imposing the usual Maxwell Boundary Conditions (MBCs), which specify the continuity of the surface parallel components of the electric and magnetic fields at metallo-dielectric boundaries. This approach fully specifies the EM fields in the absence of spatial dispersion, however these boundary conditions are no longer sufficient in the nonlocal regime, where spatial dispersion leads to the emergence of longitudinal EM waves within the metal bulk. The emergence of these waves results in an additional degree of freedom, which manifests itself in the form of a coefficient that specifies the amplitude of longitudinal waves within the metal. To specify this parameter an Additional Boundary Condition (ABC) is required [120]. Discussion relating to the form of the ABC that is appropriate in this context has resulted in a number of contributions from various authors over the past years. [58; 52; 49; 120; 105]

Most recently, *Mortensen et al.* have argued that the appropriate boundary condition is the continuity of the normal component of the current $\mathbf{J}$, which follows from the continuity equation for the electron density. [93; 153; 115] On the other hand, continuity of $\mathbf{J}$ has been questioned in the past by other others. [120]

The ABC can be equivalently imposed on **J** or **E**. In the case of a material described by a *Drude* dielectric function of the form

$$\epsilon(\omega) = \epsilon_\infty - \frac{\omega_p^2}{\omega(\gamma i + \omega)} \tag{2.28}$$

There are two cases of interest: the case where $\epsilon_\infty = 1$ and the case where ϵ_∞ is chosen different from 1 in order to account for the contribution of bound charges to the dielectric function. In the former case, imposing continuity of the normal component of the electric field **E** is equivalent to imposing continuity of the normal component of the current **J**. However, restricting ϵ_∞ only leaves us with two free parameters, γ and ω_p, with which to fit the dielectric function to experimental data. To obtain a better fitting there are several approaches. For example, ϵ_∞ can be used as a (in general frequency dependent) free parameter that can be chosen to better approximate the experimental data. Another approach is to add additional Lorentzian terms to 2.28 to represent the contribution of bound electrons. Specifically, a single Lorentzian term, added to the *Drude* term of 2.28 (with $\epsilon_\infty = 1$), is sufficient to obtain a reasonably exact representation for the experimentally measured dielectric function of silver. [126]

In the following we will restrict our analysis to a single (*Drude* like) resonance term, however allowing for $\epsilon_\infty \neq 1$. This choice of $\epsilon(\omega)$ results in a complication when choosing the ABC, as continuity of the normal component of **E** and **J** are no longer equivalent. To identify the appropriate boundary condition to be used in this situation we argue from a phenomenological perspective. The hydrodynamic model, on which our analysis is based, is a simplification of the underlying physics that sacrifices quantitative correctness of results in favour of ease of implementation and low computational cost (compared to full quantum ab initio calculations). However, despite the simplifications that are inherent in the hydrodynamic model, the model has been successful in predicting trends in the far field behaviour of plasmonic systems affected by nonlocal response in accordance with experimental results. [116; 23] Thus, in choosing a boundary condition, which necessarily modifies the near-fields, we again seek to make a choice that at least qualitatively reproduces the physics relevant at these length scales (in particular the behaviour of the electric field across the metal-dielectric interface).

In noble metals such as gold or silver, the magnitude of the *Fermi-Thomas* wavelength is very similar to the lattice constant. [6] Therefore, both the variation in the conduction electron and the variation in the core residual permittivities happens over a similar length scale, and are abrupt/not abrupt over this shared scale. The former is dictated by the *Fermi-Thomas* wavelength, the latter by the lattice constant. Thus, to ensure that both the conduction electrons and the core residual permittivities are terminated smoothly at the metallic boundary, we impose continuity of the normal component of **E** as the ABC. We have arrived at this phenomenological choice of the ABC in order to capture the electronic behaviour at material boundaries. However, we note that care must be

taken in imposing a boundary condition for the hydrodynamic model when considering materials other than noble metals. For example, full quantum calculations have revealed that in the case of alkali clusters a spill out of the electronic charge into the vacuum region is expected [139], which the hydrodynamic model in the form used here is unable to capture. Addressing this deficiency, recent work by *Mortensen et al.* [92] attempts to represent this physics through a generalized non-local optical response theory, which is based on a complex valued nonlocality parameter β.

2.4 Nonlocal analytical solutions

The transverse (eq. (2.27)) and longitudinal (eq. (2.26)) components of the hydrodynamic nonlocal *Drude* dielectric function, derived in section 2.3.2, together with the Additional Boundary Condition (ABC) from section 2.3.3 can be used to derive analytical solutions to the problem of nonlocal Electromagnetic (EM) wave propagation in many geometries that are of interest to current developments in plasmonics. The solution strategy is straightforward, and begins with the determination of a dispersion relation for the plasmonic modes that are supported by the system under study. Such a dispersion relation can be obtained in the usual way familiar from local electromagnetics, by postulating trial solutions to *Maxwell*'s equations for all the geometrically distinct regions of the system and then determining the amplitude factors of these trial solutions by imposing the Maxwell Boundary Conditions (MBCs) and an appropriate ABC at material boundaries. This procedure can be used to derive dispersion relations for a variety of simple geometries, including Two-Dimensional (2D) Metal-Insulator-Metal (MIM) and Insulator-Metal-Insulator (IMI) stacks (section 3.1.2) and their rotationally symmetric equivalents in Three-Dimensional (3D) space (section 3.3.2).

In certain simple geometries, such as in the case of an infinite metallic half-space, the dispersion relations can then be inserted directly into the trial solutions for the electric and magnetic fields to obtain a full field solution that gives the value of the fields at any point in space. For more complex waveguiding geometries, the dispersion relations are used in the context of more intricate solution schemes, including *Wentzel-Kramers-Brillouin* (WKB) theory [134; 148], and transformation optics. [37]

In this section we present nonlocal analytical dispersion relations for three geometries: an infinite metallic half space, infinite metallic cylinders, and metal insulator metal wedges. In the results section (chapter 3) we will use these equations to gain further physical insights into the nonlocal modes supported by these geometries, before proceeding to utilise them to construct WKB full field EM solutions for tapered modifications of the above simple geometries (nanofocusing plasmonic tips and metal-insulator-metal waveguides) that will enable us to investigate the characteristics of nonlocal EM fields propagation in these systems.

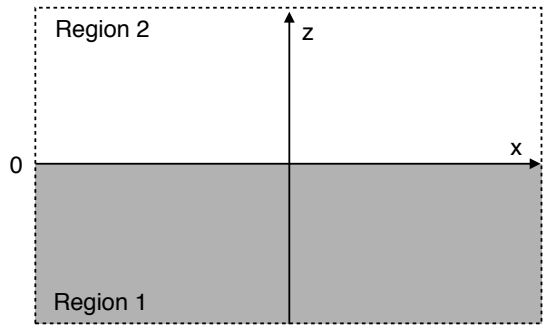


FIGURE 2.1: Infinite metallic half space.

2.4.1 Infinite metallic half-space

Nonlocal calculations can be performed analytically for some simple geometries, including flat surfaces [124] and cylindrical waveguides [123]. In this section, we first calculate the well known (local) surface plasmon dispersion relation for a Surface Plasmon Polariton (SPP) propagating on the surface of an infinite metallic half space (see Fig. 2.1). Following Ref. [124] we then show how this calculation can be modified to include nonlocal effects.

The *Maxwell*'s equations (eq. (2.1)), and the constitutive relations given by eq. (2.2) can be combined to give:

$$\nabla \times \ \nabla \times \ \mathbf{E} = -\mu_0 \frac{\partial^2 \mathbf{D}}{\partial t^2} \tag{2.29}$$

where we have assumed a non-magnetic ($\mu = 1$) material with no external stimuli ($\mathbf{J}_{\text{ext}} = 0$.) The Left Hand Side (LHS) of eq. (2.29) can be rewritten using the vector identity $\nabla \times \ \nabla \times \ \mathbf{E} = \nabla(\nabla \cdot \ \mathbf{E}) - \nabla^2 \mathbf{E}$. This, together with the product rule $\nabla \cdot (\epsilon \ \mathbf{E}) = \epsilon \ \nabla \cdot \mathbf{E} + \mathbf{E} \cdot \ \nabla \epsilon$ and the fact that $\nabla \cdot \mathbf{D} = 0$, results in

$$\nabla \left(-\frac{1}{\epsilon} \mathbf{E} \cdot \nabla \epsilon \right) - \nabla^2 \mathbf{E} = -\mu_0 \epsilon_0 \epsilon \frac{\partial^2 \mathbf{E}}{\partial t^2} \tag{2.30}$$

This expression can be simplified by assuming that ϵ varies slowly over distances smaller than one wavelength, giving the following wave equation for the electric field

$$\nabla^2 \mathbf{E} - \frac{\epsilon}{c^2} \frac{\partial^2 \mathbf{E}}{\partial t^2} = 0 \tag{2.31}$$

For a time harmonic field the wave equation becomes

$$\nabla^2 \mathbf{E} - k_0^2 \epsilon \ \mathbf{E} = 0 \tag{2.32}$$

We now look for waves of the form $\mathbf{E}(x,y,z) = \mathbf{E}(z)e^{ik_x x}$, i.e. waves that are propagating in the x direction. Such waves satisfy

$$\frac{\partial^2 \mathbf{E}(z)}{\partial z^2} + \left(k_0^2\epsilon - k_x^2\right)\mathbf{E} = 0 \tag{2.33}$$

This equation, on it's own, has many solutions. However, we know that any valid solution also needs to satisfy *Maxwell*'s equations. Thus, we identify two solution sets of transverse waves: Transverse Magnetic (TM) and Transverse Electric (TE). In this way, we find that TM waves satisfy

$$E_x = -i\frac{1}{\omega\ \epsilon_0\epsilon}\frac{\partial H_y}{\partial z} \tag{2.34}$$

$$E_z = -\frac{k_x}{\omega\ \epsilon_0\epsilon}H_y \tag{2.35}$$

$$\frac{\partial^2 H_y}{\partial z^2} + \left(k_0^2\epsilon - k_x^2\right)H_y = 0 \tag{2.36}$$

and that TE waves satisfy

$$H_x = -i\frac{1}{\omega\ \mu_0}\frac{\partial E_y}{\partial z} \tag{2.37}$$

$$H_z = \frac{k_x}{\omega\ \mu_0}E_y \tag{2.38}$$

$$\frac{\partial^2 H_y}{\partial z^2} + \left(k_0^2\epsilon - k_x^2\right)E_y = 0 \tag{2.39}$$

We now consider waves propagating at the interface of an infinite metallic half space, as depicted in Fig. 2.1. It can be shown that TE waves do not excite surface plasmons. [79] For this reason we consider here only TM modes. Just above the interface, Eqs. 2.34 and 2.35 specify the amplitudes of a TM mode as

$$\mathbf{H}_T^{(2)}(z) = \hat{\mathbf{y}}A_2 e^{ik_x\ x}e^{-k_{z,2}z} \tag{2.40}$$

and

$$\mathbf{E}_T^{(2)}(z) = (\hat{\mathbf{x}}\frac{iA_2k_{z,2}}{\omega\ \epsilon_0\epsilon_2} - \hat{\mathbf{z}}\frac{A_2k_{x,2}}{\omega\ \epsilon_0\epsilon_2})e^{ik_x\ x}e^{-k_{z,2}z} \tag{2.41}$$

Similarly, just below the interface we find

$$\mathbf{H}_T^{(1)}(z) = \hat{\mathbf{y}}A_1 e^{ik_x\ x}e^{k_{z,1}z} \tag{2.42}$$

and

$$\mathbf{E}_T^{(1)}(z) = -(\hat{\mathbf{x}}\frac{iA_1k_{z1}}{\omega\ \epsilon_0\epsilon_1} + \hat{\mathbf{z}}\frac{A_1k_{x,1}}{\omega\ \epsilon_0\epsilon_1})e^{ik_x\ x}e^{k_{z,1}z} \tag{2.43}$$

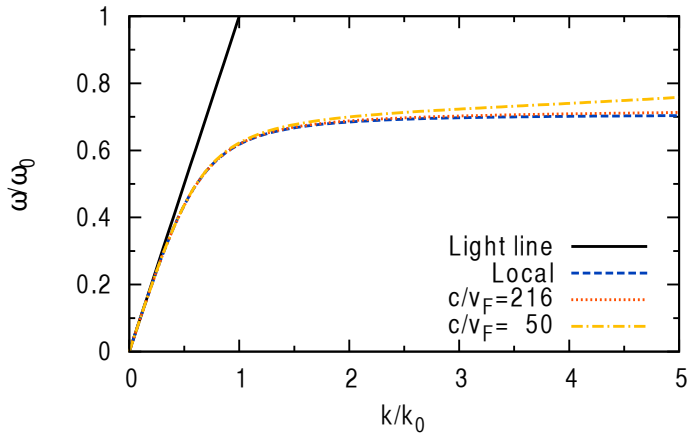


FIGURE 2.2: Dispersion relation for SPP propagating on an infinite metallic metallic half space.

Noting the continuity of k_x ($k_{x,1} = k_{x,2} \equiv k_x$

$$\begin{pmatrix} 1 & -1 \\ \frac{ik_{z,1}}{k_0\epsilon_1} & \frac{ik_{z,2}}{k_0\epsilon_2} \end{pmatrix} \begin{pmatrix} A_1 \\ A_2 \end{pmatrix} = 0 \tag{2.44}$$

with $k_0 = \omega/c$. The solution has to satisfy Eq. 2.36, which implies $k_z^2 = k_x^2 - k_0^2\epsilon$ for both half spaces. A solution to Eq. 2.44 exists if the determinant of the matrix on the LHS is zero. Thus, we obtain the dispersion relation for the SPPs

$$\frac{\sqrt{k_x^2 - k_0^2\epsilon_2}}{k_0\epsilon_2} + \frac{\sqrt{k_x^2 - k_0^2\epsilon_1}}{k_0\epsilon_1} = 0 \tag{2.45}$$

Normalising to the plasma wavevector $k_p = \omega_p c$ we retrieve

$$\epsilon_1\sqrt{\kappa_x^2 - \kappa_0^2\epsilon_2} + \epsilon_2\sqrt{\kappa_x^2 - \kappa_0^2\epsilon_1} = 0 \tag{2.46}$$

with $\kappa_x = k_x/k_p$ and $\kappa_0 = k_0/k_p$.

The solution to 2.44 may be written in the more familiar form [79]

$$k_x = k_0\sqrt{\frac{\epsilon_1\epsilon_2}{\epsilon_1 + \epsilon_2}} \tag{2.47}$$

which is the well known dispersion relation for a SPP propagating at the surface of a metallic half space with a frequency dependent dielectric function ϵ_1, adjacent to a dielectric half space with dielectric constant ϵ_2.

Using a local undamped dielectric function for the bulk metal

$$\epsilon(\omega) = 1 - \frac{\omega_p^2}{\omega^2} \tag{2.48}$$

we may plot the dispersion relation from Eq. 2.46, as reproduced in Fig. 2.2.

As previously done by *Ruppin* [124] we now consider the nonlocal case, which differs from the local calculation in the sense that we have to allow for the excitation of longitudinal plasmons, as shown analytically by *Fuchs* [39] and numerically by *McMahon*'s nonlocal Finite Difference Time Domain (FDTD) calculations [84].

The nonlocal calculation is similar to the one for the local case. The nonlocal contribution is negligible for the transverse modes, however for the longitudinal modes a nonlocal dielectric function has to be used. [39] Here we use the undamped hydrodynamic model (introduced in section 2.5) to obtain the longitudinal component of the dielectric function

$$\epsilon(k,\omega) = 1 - \frac{\omega_p^2}{\omega^2 - \beta^2 k^2} \tag{2.49}$$

with $\beta^2 = Cv_F/D$. D is the number of dimensions of the system. For low frequencies $C = 1$ and for high frequencies $C = 3D/(D+2)$. [57] v_F is the Fermi velocity.

The longitudinal modes must satisfy $\nabla \times \mathbf{E} = 0$. The direction of the electric field of these modes is in the direction of propagation, which allows us to write the modes as

$$\mathbf{E}_{L,1} = A_3 \left(\hat{\mathbf{x}} + i\frac{k_{z,1}}{k_x}\hat{\mathbf{z}} \right) e^{k_{z,1}z} e^{ik_x x} \tag{2.50}$$

which follows simply by stipulating a wave whose amplitude is in the direction of the wavevector.

In the hydrodynamic model (eq. (2.49)) the dispersion relation for the bulk plasmons ($\epsilon(k,\omega) = 0$) is given by [57]

$$\omega^2(k) = \omega_p^2 + \beta^2 k^2 = \omega_p^2 + \beta^2 k_0^2 \epsilon \tag{2.51}$$

this allows us to write the wavevector in the z direction in the form

$$\gamma_{z,1} = \sqrt{k_{x,1}^2 + \left(\omega_p^2 - c^2 {k_0}^2\right)\beta^{-2}} \tag{2.52}$$

Eq. 2.1d implies that longitudinal oscillations of the electric field have no associated magnetic field

$$i\mathbf{k} \times \mathbf{E} = \mu_0 \omega \mathbf{H} \tag{2.53}$$

We are now in a position where we can impose the boundary conditions for the fields at the interface between the two media. This, following the discussion from section 2.3.3, we proceed by imposing continuity of the surface parallel electric fields and surface normal magnetic fields (MBC), as well as of the surface-normal electric fields (ABC), obtaining

$$\mathbf{E}_T^{(2)} = \mathbf{E}_T^{(1)} + \mathbf{E}_L^{(1)} \tag{2.54}$$

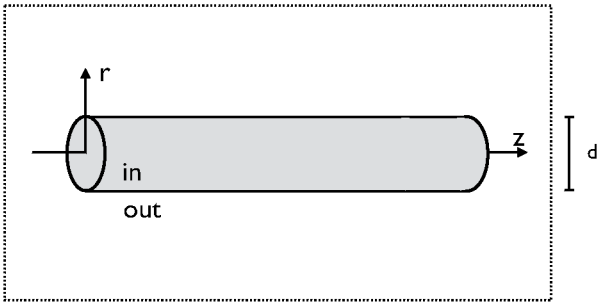


FIGURE 2.3: Infinitely long metallic cylinder of diameter d, embedded in air. The SPP mode is propagating in the z direction.

and

$$\mathbf{H}_T^{(2)} = \mathbf{H}_T^{(1)} \tag{2.55}$$

Writing the resulting system of linear equations in matrix form we obtain the (nonlocal) dispersion relation for SPPs propagating on an infinite metallic half space

$$\begin{pmatrix} 1 & -1 & 0 \\ \frac{ik_{z,1}}{k_0\epsilon_1} & \frac{ik_{z,2}}{k_0\epsilon_2} & \frac{ik_0}{\gamma_{z,2}} \\ -\frac{k_{x,1}}{k_0\epsilon_1} & \frac{k_{x,2}}{k_0\epsilon_2} & \frac{k_0}{k_x} \end{pmatrix} \begin{pmatrix} A_1 \\ A_2 \\ A_3 \end{pmatrix} = 0 \tag{2.56}$$

Setting to zero the determinant of the matrix on the LHS of this equation we obtain the dispersion relation. The solution can be evaluated numerically. In Fig. 2.2 we plot the dispersion relation for $c/v_F = 216$ ($\beta = 0.0036c$), a realistic value for Au assuming $v_F = 1.39 \times 10^6$ m/s. [83] For comparison, plotted alongside is the local case and an extreme case where $c/v_F = 50$ ($\beta = 0.0015c$).

Figure 2.2 shows that there is a clear difference between local and nonlocal results. For a given frequency of the light, we see that introducing nonlocality decreases the wavevector $k_x = 2\pi/\lambda$ of the SPP. This means that the wavelength of the SPP has been increased in the nonlocal case. This is an important result, because in the field of nano-plasmonics we often seek to confine light into small spatial dimensions. For this reason, it is important to be able to investigate the ways in which nonlocality may limit electromagnetic field confinement in nano-scale geometries.

2.4.2 Infinite metallic cylinder

The starting point for our derivation of a hydrodynamic nonlocal dispersion relation for infinite non-magnetic ($\mu = 1$) metallic cylinders embedded in air, depicted schematically in fig. 2.3, begins from eq. (2.32), the wave equation for a time harmonic electric field derived in section 2.4.1, namely

$$\nabla^2\mathbf{E} - k_0^2\epsilon\ \mathbf{E} = 0 \tag{2.57}$$

Moving to cylindrical coordinates we can use *Maxwell*'s equations (eq. (2.1)) to write down the transverse EM fields ($\mathbf{E}_{\text{in,out T}}$, $\mathbf{H}_{\text{in,out T}}$) in terms of the modified *Bessel* functions of the first and second kind. To incorporate nonlocal effects in the metal regions, we further allow for longitudinal waves of the electric field in the cylinder ($\mathbf{E}_{\text{in L}}$) that satisfy the dispersion relation $\omega^2 = \omega_p^2 + \beta^2 k_L^2$, where k_L is the wavevector of the longitudinal waves, ω_p is the bulk plasma frequency of the metal, and β is the nonlocality parameter introduced with the hydrodynamic model in section 2.3.2. Using exponential trial solutions oscillatory in the z direction, and imposing the requirement that fields vanish as $z \to \infty$, we obtain the EM fields inside the cylinder

$$\mathbf{E}_{\text{in T}}(r,z) = \begin{pmatrix} -\frac{ik}{q_{\text{in T}}} I_1(q_{\text{in T}}, r) \\ 0 \\ I_0(q_{\text{in T}}, r) \end{pmatrix} E_{\text{in T}} e^{ikz} \tag{2.58a}$$

$$\mathbf{H}_{\text{in T}}(r,z) = \begin{pmatrix} 0 \\ -\frac{i\omega\epsilon_0\epsilon_{\text{in T}}}{q_{\text{in T}}} \\ 0 \end{pmatrix} E_{\text{in T}} I_1(q_{\text{in}T}, r) e^{ikz} \tag{2.58b}$$

$$\mathbf{E}_{\text{in L}}(r,z) = 0 \begin{pmatrix} -\frac{iq_{\text{in L}}}{k} I_1(q_{\text{in L}}, r) \\ 0 \\ I_0(q_{\text{in L}}, r) \end{pmatrix} E_{\text{in L}} e^{ikz} \tag{2.58c}$$

$$\mathbf{H}_{\text{in L}}(r,z) = 0 \tag{2.58d}$$

and outside the cylinder

$$\mathbf{E}_{\text{out T}}(r,z) = \begin{pmatrix} -\frac{ik}{q_{\text{out T}}} K_1(q_{\text{out T}}, r) \\ 0 \\ K_0(q_{\text{out T}}, r) \end{pmatrix} E_{\text{out T}} e^{ikz} \tag{2.59a}$$

$$\mathbf{H}_{\text{out T}}(r,z) = \begin{pmatrix} 0 \\ -\frac{i\omega\epsilon_0\epsilon_{\text{out T}}}{q_{\text{out T}}} \\ 0 \end{pmatrix} E_{\text{out T}} K_1(q_{\text{in}T}, r) e^{ikz} \tag{2.59b}$$

$$\mathbf{E}_{\text{out L}}(r,z) = 0 \tag{2.59c}$$

$$\mathbf{H}_{\text{out L}}(r,z) = 0 \tag{2.59d}$$

where we have defined $q_{\text{in,out}} = (k^2 - k_0^2 \epsilon_{\text{in,out}})^{1/2}$, $q_{\text{out}L} = k^2 + (\omega_p^2 - \omega^2)/\beta^{2^{1/2}}$ alongside a *Drude* dielectric function of the form $\epsilon_{\text{in}} = \epsilon_{\infty\text{ in}} - \omega_{p\text{ in}}^2/(\omega(\omega + i\gamma_{\text{in}}))$, $\epsilon_{\text{out}} = 1$.

Next, by imposing continuity of the normal electric and normal displacement fields at the cylinder boundary ($r = R$) we obtain the dispersion relation for the azimuthally

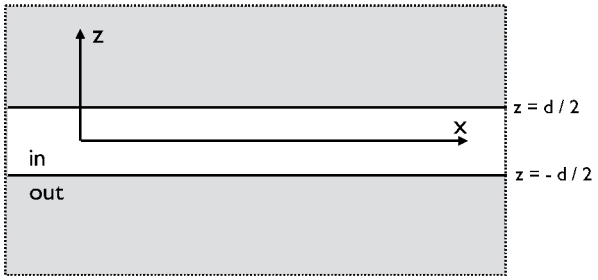


FIGURE 2.4: Infinite 2D MIM waveguide with insulator thickness d, The SPP modes are propagating in the x direction.

independent SPP modes sustained by a nonlocal metallic cylinder embedded in vacuum

$$\begin{vmatrix} 1 & -\frac{I_0(q_{\mathrm{inT}}R)}{K_0(q_{\mathrm{outT}}R)} & -\frac{I_0(q_{\mathrm{inL}}R)}{K_0(q_{\mathrm{outT}}R)} \\ 1 & \frac{\epsilon_{\mathrm{inT}}q_{\mathrm{outT}}I_1(q_{\mathrm{inT}}R)}{q_{\mathrm{inT}}K_1(q_{\mathrm{outT}}R)} & 0 \\ 1 & \frac{q_{\mathrm{outT}}I_1(q_{\mathrm{inT}}R)}{q_{\mathrm{inT}}K_1(q_{\mathrm{outT}}R)} & \frac{(q_{\mathrm{outT}}q_{\mathrm{inL}})I_1(q_{\mathrm{inL}}R)}{k^2K_1(q_{\mathrm{outT}}R)} \end{vmatrix} = 0 \tag{2.60}$$

which can equivalently be written as

$$\frac{k^2 I_0\left(q_{\mathrm{inL}}R\right)\left(\epsilon_{\mathrm{inT}}-1\right)}{q_{\mathrm{inL}}I_1\left(q_{\mathrm{inL}}R\right)} + \frac{\epsilon_{\mathrm{inT}}q_{\mathrm{outT}}K_0\left(q_{\mathrm{outT}}R\right)}{K_1\left(q_{\mathrm{outT}}R\right)} + \frac{q_{\mathrm{inT}}I_0\left(q_{\mathrm{inT}}R\right)}{I_1\left(q_{\mathrm{inT}}R\right)} = 0 \tag{2.61}$$

In section 3.3 we plot results obtained by evaluating this equation, enabling us to predict the way in which nonlocality affects the SPP modes propagating along infinite metallic nanocylinders. We will then proceed to use this dispersion relation in a WKB solution of the electric field of the symmetric SPP modes propagating towards the apex of plasmonic tips, which will enable us to investigate the effect that nonlocal effects have on the nanofocussing performance of the device.

2.4.3 Infinite metal-insulator-metal waveguide

The starting point for our derivation of a hydrodynamic nonlocal dispersion relation for infinite non-magnetic ($\mu = 1$) MIM waveguides, depicted schematically in fig. 2.4, begins again from eq. (2.32), the wave equation for a time harmonic electric field derived in section 2.4.1, namely

$$\nabla^2\mathbf{E} - k_0^2\epsilon\ \mathbf{E} = 0 \tag{2.62}$$

We use *Maxwell*'s equations (eq. (2.1)) to write down the transverse EM fields ($\mathbf{E}_{\mathrm{in,out\ T}}$, $\mathbf{H}_{\mathrm{in,out\ T}}$) from exponential trial solutions oscillatory in the x direction. To incorporate nonlocal effects in the metal regions, we further allow for longitudinal waves of the electric field in the cylinder ($\mathbf{E}_{\mathrm{in\ L}}$) that satisfy the dispersion relation $\omega^2 = \omega_p^2 + \beta^2 k_L^2$, where k_L is the wavevector of the longitudinal waves, ω_p is the bulk plasma frequency of the metal, and β is the nonlocality parameter introduced with the hydrodynamic model in section 2.3.2. Imposing the requirement that fields vanish as $z \to \infty$, we obtain

the EM fields for the symmetric and anti-symmetric SPP mode in the inner (dielectric) region

$$\mathbf{E}_{\text{in T}}(r,z) = \begin{pmatrix} e^{q_{\text{in T}}z} \pm e^{-q_{\text{in T}}z} \\ 0 \\ -\frac{ik}{q_{\text{in T}}}\left(e^{q_{\text{in T}}z} \mp e^{-q_{\text{in T}}z}\right) \end{pmatrix} E_{\text{x in T}} e^{ikx} \tag{2.63a}$$

$$\mathbf{H}_{\text{in T}}(r,z) = \begin{pmatrix} 0 \\ \frac{ik_0\epsilon_{\text{in T}}}{q_{\text{in T}}} e^{q_{\text{in T}}z} \mp e^{-q_{\text{in T}}z} \\ 0 \end{pmatrix} E_{\text{x in T}} e^{ikx} \tag{2.63b}$$

$$\mathbf{E}_{\text{in L}}(r,z) = 0 \tag{2.63c}$$

$$\mathbf{H}_{\text{in L}}(r,z) = 0 \tag{2.63d}$$

and in the outer (metallic) regions

$$\mathbf{E}_{\text{out T}}(r,z) = \begin{pmatrix} e^{-q_{\text{outT}}z} \\ 0 \\ -\frac{ik}{q_{\text{outT}}} e^{-q_{\text{outT}}z} \end{pmatrix} E_{\text{x out T}} e^{ikx} \tag{2.64a}$$

$$\mathbf{H}_{\text{out T}}(r,z) = \begin{pmatrix} 0 \\ -\frac{ik_0\epsilon_{\text{outT}}}{q_{\text{outT}}} e^{-q_{\text{outT}}z} \\ 0 \end{pmatrix} E_{\text{x out T}} e^{ikx} \tag{2.64b}$$

$$\mathbf{E}_{\text{out L}}(r,z) = \begin{pmatrix} e^{-q_{\text{outL}}z} \\ 0 \\ -\frac{q_{\text{outL}}}{ik} e^{-q_{\text{outL}}z} \end{pmatrix} E_{\text{x out L}} e^{ikx} \tag{2.64c}$$

$$\mathbf{H}_{\text{out L}}(r,z) = 0 \tag{2.64d}$$

where we have defined $q_{\text{in,out}} = (k^2 - k_0^2\epsilon_{\text{in,out}})^{1/2}$, $q_{\text{out}L} = (k^2 + (\omega_p^2 - \omega^2)/\beta^2)^{1/2}$ alongside a *Drude* dielectric function of the form $\epsilon_{\text{in,out}} = \epsilon_{\infty\ \text{in,out}} - \omega_{p\ \text{in,out}}^2/(\omega\,(\omega + i\gamma_{\text{in,out}}))$.

Next, by imposing continuity of the normal electric and normal displacement fields at the metal boundaries ($z = \pm d/2$) we obtain the dispersion relation for a nonlocal MIM waveguide in air in matrix form

$$\begin{vmatrix} \frac{e^{2q_{\text{inT}}d/2} \pm 1}{e^{2q_{\text{inT}}d/2} \mp 1} & 1 & 1 \\ \frac{\epsilon_{\text{inT}}}{q_{\text{inT}}} & -\frac{\epsilon_{\text{outT}}}{q_{\text{outT}}} & 0 \\ -\frac{1}{q_{\text{inT}}} & \frac{1}{q_{\text{outT}}} & \frac{q_{\text{inL}}}{k^2} \end{vmatrix} = 0 \tag{2.65}$$

which can equivalently be written as

$$\frac{\left(1 \pm e^{2q_{\text{inT}}d/2}\right) q_{\text{inT}}\epsilon_{\text{outT}}}{1 \mp e^{2q_{\text{inT}}d/2}} - q_{\text{outT}}\epsilon_{\text{inT}} - \frac{k^2\left(\epsilon_{\text{outT}} - \epsilon_{\text{inT}}\right)}{q_{\text{inL}}} = 0 \tag{2.66}$$

Here the top signs describe the high energy anti-symmetric mode, whereas the bottom signs give the low energy symmetric mode. In section 3.1 we plot results obtained by

evaluating this equation, enabling us to predict the way in which nonlocality affects the symmetric SPP modes propagating along MIM waveguides. We will then use results obtained from this dispersion relation in a WKB solution of the electric fields of the symmetric SPP modes propagating on the surfaces of plasmonic hourglass waveguides. A comparison to nonlocal Finite Element Method (FEM) results of the EM fields will also be provided, offering insights into the way SPP modes behave at the waist that separates the two arms of plasmonic hourglass waveguides.

2.5 Nonlocal FEM solutions

The hydrodynamical *Drude* model [38; 122; 41; 115; 148] can not only provide closed form analytical solutions for the nonlocal electromagnetic response of plasmonic nanostructures, but it also lends itself well to solving strategies based on grid or mesh based numerical methods. This dual approach is useful because it offers the speed and physical insight that is offered by analytical methods, whilst also providing an ability to verify analytical solutions using an independent method. In addition, numerical solutions have the potential to provide solutions for arbitrarily complex geometries.

The hydrodynamical equation, which describes the transport of the nonlocal currents, has been successfully tackled using Finite Difference Time Domain (FDTD) by *Mcmahon et al.* [83] for a variety of systems. [86; 84; 85] *Mcmahon*'s use of the hydrodynamical *Drude* model has highlighted the utility of this formalism in the context of plasmonics, where numerical solutions are often desirable due to the complex geometries of plasmonic targets. However, a subsequent study by *Raza et al.* [115] has pointed out that these particular FDTD studies were based on an erroneous mathematical simplification in the implementation of the transport equation for the nonlocal current. As a consequence of this simplification, which we will discuss in more detail towards the end of tis section, the results reported by *Mcmahon et al.* contained unphysical resonances in the visible spectrum.

To our knowledge, an FDTD implementation that takes into account the corrections pointed out by *Raza et al.* [115] has not yet emerged. There are two principal difficulties in applying the FDTD algorithm to sub-nanometric systems. On the one hand, these minuscule geometries require meshes that accurately resolve features on Angstrom length scales characteristic of metals treated in the nonlocal regime. On the other hand, their far fields are still characterised by the length scales characteristic of free space radiation, which is typically in the region 300-900 nm. This requires large rates of change in the mesh density, which makes it difficult to achieve an FDTD simulation that does not suffer from erroneous reflections due to the rapidly varying mesh environment. One commonly used method to overcome this problem is Finite Element Method (FEM), which is often used to treat singular plasmonic geometries both in Two-Dimensional (2D) [8; 71] and

even in Three-Dimensional (3D) geometries, [35] which highlights the potential of the FEM approach in situations where fine meshing is required.

Even though a sound implementation of the hydrodynamic method in FDTD is still lacking, a method inspired by the work of *Mcmahon et al.* was proposed by *Toscano et al.*, [141] who implemented the hydrodynamic method using FEM. This is the approach we will adopt for our numerical studies of nonlocality, and we will now give a brief introduction of this method. At the end of this derivation we will also expand upon the erroneous simplification made by *Mcmahon et al.* [83; 115] and illustrate how it leads to unphysical resonances in the visible spectrum.

Working towards an electromagnetic wave equation for the electric field in the frequency domain, we begin by combining the *Maxwell*'s equations (eq. (2.1)), and the constitutive relations given by eq. (2.2) to yield

$$\nabla \times (\nabla \times \mathbf{E}) = -\mu_0 \frac{\partial^2 \mathbf{D}}{\partial t^2} \tag{2.67}$$

where we have assumed a non-magnetic ($\mu = 1$) material with no external stimuli ($\mathbf{J}_{\text{ext}} = 0.$)

Next, we define

$$\mathbf{D} = \epsilon_0 \epsilon_\infty \mathbf{E} + \mathbf{D}_{\text{cond}} \tag{2.68}$$

which decomposes the displacement field into two parts, with $\epsilon_0 \epsilon_\infty$E representing the contribution from ionic background and core electrons and $\mathbf{D}_{\text{cond}}$ denoting the contribution to the displacement field originating from conduction electrons.

After substituting eq. (2.68) into eq. (2.67) and defining a displacement current $\mathbf{J}_{\text{d}} = \partial \mathbf{D}/\partial t$ we assume a harmonic time dependence for all the fields (e.g. $\mathbf{J} \sim e^{-i\omega t}$), which enables us to write the time harmonic electric field associated with the Surface Plasmon Polariton (SPP) modes supported by an arbitrary metal nanostructure in the frequency domain, $\mathbf{E}(\omega)$, in terms of the following inhomogeneous *Maxwell* wave equation

$$\nabla \times (\nabla \times \mathbf{E}) = \frac{\omega^2}{c^2} \epsilon_\infty \mathbf{E} + i\omega\mu_0 \mathbf{J}_{\text{d}} \tag{2.69}$$

where the first and second source terms describe the positive background charge due to the ion cores and the nonlocal displacement current, respectively. Within the hydrodynamical *Drude* model, which we introduced in section 2.3.2, the transport equation for this nonlocal current $\mathbf{J}_{\text{d}}$ reads

$$\beta^2 \nabla[\nabla \cdot \mathbf{J}_{\text{d}}] + \omega(\omega + i\gamma)\mathbf{J}_{\text{d}} = i\omega\omega_{\text{P}}^2 \epsilon_0 \mathbf{E}. \tag{2.70}$$

Equation (2.70) governs the dynamics of the electron density in the nonlocal metal. The first term describes the spread in electron velocities and the remaining ones are

the usual *Drude* terms for a noninteracting electron gas. The nonlocal parameter β is, except for an adimensional factor, equal to the Fermi velocity of the metal. [15] It is closely related to the decay length δ_{LP} of the longitudinal plasmons excited in the metal structure due to spatial dispersion. Thus, at frequencies well below the plasma frequency, ω_{P}, we can write $\beta \approx \delta_{\mathrm{LP}}\omega_{\mathrm{P}}$. [37] Note that in the limit $\beta = 0$ eq. (2.70) recovers the local description, which provides us with the fitting parameters for the usual *Drude* permittivity, $\epsilon_{\mathrm{D}}(\omega) = \epsilon_\infty - \omega_{\mathrm{P}}^2/[\omega(\omega + i\gamma)]$.

We follow the approach outlined in Ref. 143 to solve eqs. (2.69) and (2.70) simultaneously on a highly adaptive mesh using *Comsol Multiphysics*, a commercial FEM solver.[5]

The usual *Maxwell* boundary conditions for the continuity of the Electromagnetic (EM) fields are implemented, but they have to be augmented by an Additional Boundary Condition (ABC). Since the lattice constant (interionic distance) is similar to the *Coulomb* screening length (interelectronic distance) for noble metals such as gold or silver, the appropriate additional condition for our problem is the continuity of the normal component of the electric field.

For the special case $\epsilon_\infty = 1$ the condition at the boundary is given by the *Pekar* ABC, which requires the continuity of the normal component of $\mathbf{J}_{NL}$ at the boundaries [105]. We implement the *Pekar* ABC by imposing a *Neumann* boundary condition [1] at the metal-dielectric interfaces

$$\mathbf{n} \cdot (\beta^2 \nabla \mathbf{J}_{NL}) = 0 \tag{2.71}$$

This boundary condition forces the flux of $\mathbf{J}_{NL}$ in the direction normal to the boundaries to zero, which imposes the *Pekar* ABC. This scheme is also applicable to the general case where $\epsilon_\infty \neq 1$, as any *Drude* dielectric function of the form $\epsilon'(\omega) = \epsilon_\infty - \omega_p^2/\omega\,(\omega + i\gamma)$ can be rewritten in terms of a *Drude* dielectric function with a pair of frequency dependent fitting parameters $\omega_p'(\omega)$ and $\gamma'(\omega)$. Using these parameters the dielectric function may be cast in the form $\epsilon'(\omega) = 1 - \omega_p'^2(\omega)/\omega\,(\omega + i\gamma(\omega))$.

We note that in the local limit, where $\beta = 0$, eq. (2.70) yields the *Drude* dielectric function [79]

$$\epsilon_D(\omega) = \epsilon_\infty - \frac{\omega_p^2}{\omega\,(\omega + i\gamma)} \tag{2.72}$$

where ω_p is the bulk plasma frequency, ϵ_∞ is added to describe the polarisation due to free electrons and γ is a damping factor. For noble metals such as gold or silver, these constants can be determined by fitting to experimental data. [103; 60]

This concludes our exposition of the nonlocal hydrodynamical FEM model, as the simultaneous solution of eqs. (2.69) and (2.70), together with the ABC in eq. (2.71) is sufficient to determine the nonlocal EM fields both in 2D and in 3D.

[5] For suitable geometries we may take advantage of the rotational symmetry of systems to map a three-dimensional problem into a two-dimensional one, which offers significant computational advantages.

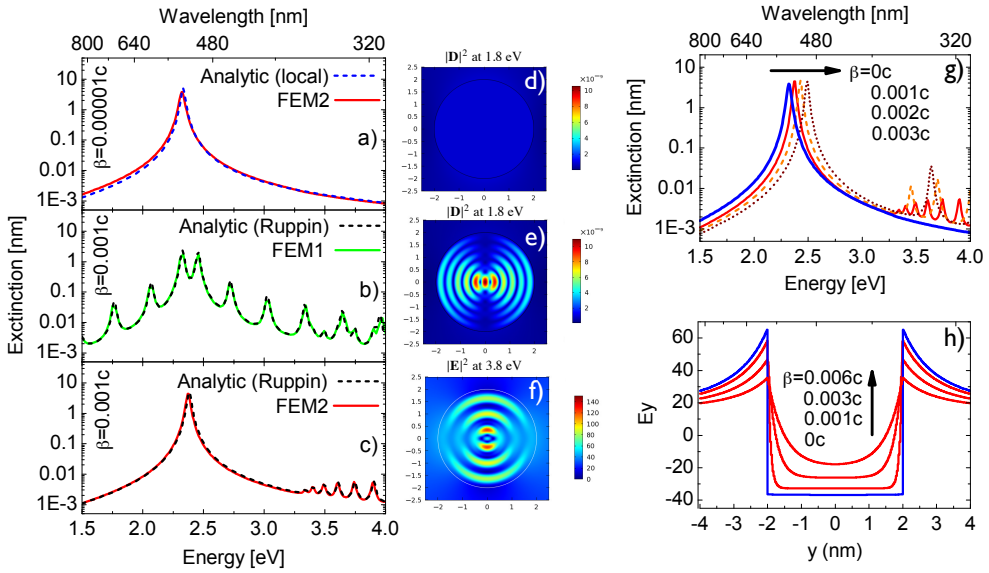


FIGURE 2.5: Results for an $R = 2$ nm silver nanowire with $\epsilon_\infty = 1$, $\omega_p = 3.3$ eV and $\gamma = 0.01\omega_p$. (a) Local analytic (dashed line) and local FEM (solid line) absorption cross section. (b) nonlocal curl-free analytic [121] (dashed line) and nonlocal curl-free FEM (solid line) absorption cross section. (c) nonlocal analytic [122] (dashed line) and nonlocal FEM (solid line) absorption cross section. (d) field plot corresponding to a. (e) field plot corresponding to (b). (f) field plot corresponding to (c). (g) nonlocal FEM (solid line) absorption cross section for different degrees of nonlocality. (h) E field along a line cutting through the cylinder of the incident field for different β.

Finally, we now proceed by illustrating how the closely related work by *Mcmahon et al.* [83], mentioned at the beginning of this section, can lead to unphysical resonances in the visible spectrum. The derivation given by *Mcmahon et al.* assumes that, when operating within the curl-free assumption $\nabla \times \mathbf{E} = 0$, together with eq. (2.70) implies that $\nabla \times \mathbf{J} = 0$. [115] Thus $\nabla(\nabla \cdot \mathbf{J}) = \nabla \times \nabla \times \mathbf{J} + \nabla^2 \mathbf{J} = \nabla^2 \mathbf{J}$, which allows us to simplify eq. (2.70), yielding

$$\beta^2 \nabla^2 \mathbf{J}_\mathrm{d} + \omega(\omega + i\gamma)\mathbf{J}_\mathrm{d} = i\omega\omega_\mathrm{p}^2 \epsilon_0 \mathbf{E}. \tag{2.73}$$

With this simplification, the *Fourier* transform of this equation into k-space is trivial, leading to

$$\mathbf{J}_d(\mathbf{k}, \omega) = -\frac{i\omega\epsilon_0\omega_p^2}{\omega(\omega + i\gamma) - \beta^2\mathbf{k}^2}\mathbf{E}(\mathbf{k}, \omega) \tag{2.74}$$

From this it is possible to identify the nonlocal contribution $\epsilon_{NL}(\mathbf{k}, \omega)$ to the dielectric function as

$$\epsilon_{NL}(\mathbf{k}, \omega) = -\frac{\omega_p^2}{\omega(\omega + i\gamma) - \beta^2\mathbf{k}^2} \tag{2.75}$$

Fig. 2.5 validates our nonlocal FEM implementation against exact analytic solutions by other authors. In panel (a) we show the local limit. As expected we find that theory and simulation results match very well in that case. The corresponding contour field plot (panel (d)) shows that there are no standing **D** field waves in the bulk. In panels (b) and

(e) we show results obtained by applying the curl-free assumption to the hydrodynamic equation. In doing so we follow the methodology first proposed by *Mcmahon et al.* [83]. We find excellent agreement with the analytical solution derived by *Ruppin* [121] which imposes the same curl-free assumption on the electric field.

The above scheme, based on the curl-free assumption, has recently been shown to be unphysical. [115] specifically, the optical resonances which it predicts below the bulk plasma frequency are erroneous in the context of the hydrodynamic model. This conclusion follows directly from the dispersion relation of the bulk plasmons (eq. (2.51)), which gives $k(\omega) = \sqrt{(\omega^2 - \omega_p^2)/\beta^2}$, which implies a partly imaginary wavevector $k(\omega)$ for frequencies ω below the bulk plasma frequency ω_p. The imaginary part of k means that the bulk resonances are damped out in the regime $\omega < \omega_p$, and thus the results obtained by *Mcmahon et al.*, which include strong resonances in this regime, are seen to be in contradiction with the hydrodynamical *Drude* model.

Following the approach by *Toscano et al.*, [143] we have implemented the hydrodynamic equation in our nonlocal FEM scheme without making the curl-free assumption. Results from this implementation are shown in fig. 2.5 (c) and fig. 2.5f. We find excellent agreement with an analytic nonlocal solution by *Ruppin.* [122] In what follows we will now always use the nonlocal scheme which is based on the full hydrodynamic equation.

In fig. 2.5 (g) and fig. 2.5 (h) we begin to explore the effects of nonlocality. In Figs. fig. 2.5 (g) the absorption cross section of a metallic cylinder is shown for different degrees of nonlocality. It is seen that more nonlocality leads to a blueshift of the Localised Surface Plasmon Resonance (LSPR) of a metallic cylinder. In addition, the nonlocal resonances above the bulk plasma frequency increase in amplitude and shift to higher energies as the degree of nonlocality is increased. In fig. 2.5 (h) we plot the electric field along a line that cuts through the cylinder in the polarisation direction of the incident field for different degrees of nonlocality. We observe that nonlocality removes the discontinuity in the component of the electric field normal to the metallo-dielectric interfaces. This effect occurs alongside EM fields that are seen to penetrate into the bulk of the nanowire to an increasing extent as the degree of nonlocality is increased.

2.6 Calculating dispersion relations

The calculation of dispersion relations is often a crucial component in the analysis of plasmonics systems. The dispersion relation for Surface Plasmon Polaritons (SPPs), which can be obtained by imposing the appropriate boundary conditions at metal surfaces, provides the relationship between the frequency ω at which a particular set of plasmonic modes are driven, for example by an external light source, and the wavevector k_{SPP} that characterises their effective wavelength ($k_{\mathrm{SPP}} = 2\pi/\lambda_{\mathrm{SPP}}$). In some cases, such as

the one of a non-magnetic infinite metallic half space, the dispersion relation can be obtained as a closed formed analytical expression:

$$k_{\mathrm{SPP}}(\omega) = k_0(\omega)\sqrt{\frac{\epsilon(\omega)}{1+\epsilon(\omega)}} \tag{2.76}$$

where $k_0(\omega) = \omega/c$ is the free space wavevector and $\epsilon(\omega)$ is the dielectric function of the infinite metallic half space, truncated by an infinite vacuumous half space with dielectric constant $\epsilon(\omega) = 1$.

However, in other cases, such as in that of an infinite metallic nanowire of radius R, closed form solutions for $k_0(\omega, R)$ lead to a transcendental equation, which can only be solved using a numerical approach. [134] In such cases, a lookup table can be constructed for $k_0(\omega, R)$. The solving strategy we use to obtain such a lookup table is as follows.

First, we equate the dispersion relation to zero and take the absolute value of both sides of the equation, which results in an equation of the form

$$0 = |f[k_0(\omega, R), \omega, R]| \tag{2.77}$$

where f represents a general function of all the parameters involved in the dispersion relation.

Next, we arrange the independent variables, here ω and R, on a grid of size N by M, with elements (ω_i, R_j), where $0 < i \leq N, i \in \mathbb{Z}$ and where $0 < j \leq M, j \in \mathbb{Z}$. For each element, we determine the real and imaginary parts of $k(\omega_i, R_j)$ through a numerical solution [19] of eq. (2.77). The numerical solution requires an initial estimate for $k(\omega_i, R_j)$. We obtain this estimate from the light line for $k(\omega_0, R_N)$, and from neighbouring grid points thereafter.

This calculation can be performed once for a given dispersion relation, and the result cached in a lookup table for future use.

Chapter 3

Results

In the proceeding sections we have given a brief outline of the current state of the field of plasmonics, motivating our interest in nonlocal effects in particular. After surveying the literature for techniques and strategies that can be used to model nonlocality in the context of the physics of nano-sculpted structures in plasmonics, we have identified the hydrodynamical *Drude* model as a promising candidate to model the effects of spatial dispersion [15]. We have then introduced this method, providing two complementary solving strategies that allow us to model suitable physical systems both from a theoretical perspective (using full field analytical solutions) and also from a numerical perspective (using a Finite Element Method (FEM) approach).

Our choice of the hydrodynamical *Drude* model to model nonlocal response is grounded in a number of successful studies that have recently emerged based on this method. These previous studies were largely limited to 2D structures, and both the finite difference time domain method [83; 84] and FEM [143; 115] approaches were used to solve the underlying sets of equations. These schemes have been successfully tested against analytical descriptions which exist for simple geometries such as isolated nanoparticles [120; 38; 122], and more recently, separated [41; 25] and touching dimers [37].[1]

Thus, although there has been an enormous advance in the theoretical description of nonlocal effects in plasmonics, many experimentally relevant structures still remain unexplored. In this Chapter and the containing Sections we therefore put the theoretical tools developed in chapter 2 to use, applying them to a variety of experimentally relevant geometries, with a view to clarifying the role that spatial dispersion plays in the physics of plasmonic devices.

Our selection of studies in this Thesis, schematically summarised in fig. 3.1, was guided in part by the expectation that diminutive metallic features are characteristic of structures

[1] Note that quantum treatments of the optical properties of nanoparticle dimers can be also found in the literature [156; 82], but their range of applicability is restricted to extremely small structures due to their highly demanding computational requirements.

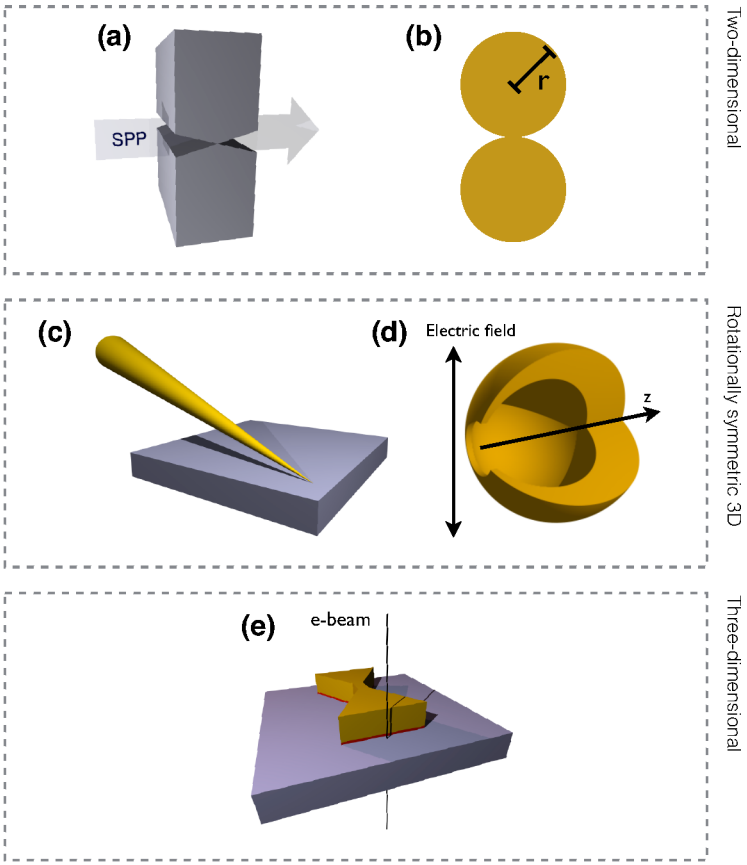


FIGURE 3.1: Schematic renderings of plasmonic structures investigated: (a) 2D hourglass MIM waveguides under end-fire excitation, (b) 2D kissing metallic nanowires under plane wave illumination, (c) rotationally symmetric 3D nanofocusing metallic tips under end-fire excitation, (d) rotationally symmetric 3D nanocrescent light harvesters under plane wave illumination, and (e) coupled metallic nanoprisms under electron beam excitation, separated from a dielectric substrate by a thin chromium adhesion layer.

where nonlocal effects are significant. The size of structures is relevant because it dictates the effective wavelength of plasmonic modes. We expect from our preliminary theoretical considerations in section 2.3.1 that effects of spatial dispersion will become significant when this effective wavelength begins to approach the length scales characteristic of the *Fermi-Thomas* screening length. For this reason, our first study in this chapter considers a plasmonic MIM hourglass geometry, schematically depicted in fig. 3.1 (a), which we have selected because of its ability to efficiently compress plasmonic modes into deep sub- wavelength volumes. This geometry will also enable us to investigate the behaviour of Surface Plasmon Polaritons (SPPs) as they approach geometrical singularities, such as the one that is present at the hourglass waist.

Subsequent studies in this chapter are arranged to build on each other thematically, gradually exploring related but more intricate geometries. Following on from hourglass waveguides, we consider kissing metallic cylinders (fig. 3.1 (b)), which just like hourglass waveguides offer the possibility for SPPs to tunnel through a singularity, but in addition

this geometry also allows for self-interference from circulating surface modes. Next, we move into rotationally symmetric three dimensional space, starting with conical plasmonic tips (fig. 3.1 (c)), which offer a promising platform for nanofocusing. After exploring the effects of surface roughness in this tip geometry, we then consider nanofocusing in axially symmetric three-dimensional nano-crescent light harvesters, schematically depicted in fig. 3.1 (d). Finally, moving beyond the constraints imposed by rotational symmetry, we investigate sets of bow-tie antaennas on dielectric substrates under Electron Energy Loss Spectroscopy (EELS) excitation (fig. 3.1 (e)). The intricate geometry considered there (consisting of an electron beam driving blunted gold targets on top of a thin chromium adhesion layer) precludes an analytical solution, however it allows us to compare our findings to recent experimental results by other authors.

3.1 Nonlocality induced tunneling of surface plasmons through singular contacts

3.1.1 Introduction

Nanofocusing devices [96; 134] are attracting research attention due to their many potential applications in current on-chip photonic technology [67]. The ability of these plasmonic structures to concentrate light at the nanoscale has strong implications in areas as different as long-range waveguiding [22], quantum optics [21], and nanometrology [138]. Lately, this research field has been driven by enormous advances in nano fabrication, which make it possible to shape metallic structures with unprecedented precision [125; 128; 147]. The classical electrodynamics description of the optical modes supported by these devices predicts a strong reduction of the effective plasmonic wavelength as the metal size shrinks. Within this local approximation, Electromagnetic (EM) fields vary significantly over length scales comparable to the characteristic *Thomas-Fermi* wavelength of conduction electrons (~ 0.1 nm in noble metals such as gold or silver [6]). The occurrence of these rapid spatial EM oscillations means that the usual free electron description of the metal permittivity (*Drude* model) is no longer justified. Thus, in order to reflect the emergence of strong electronic interactions at this sub-nanometer length scale, the implementation of nonlocal dielectric functions for the metal regions is required.

In this section we consider a linearly tapered Metal-Insulator-Metal (MIM) waveguide, where spatial dispersion in the metal regions is taken into account within the hydrodynamical approach [38; 122; 41; 115; 148]. First, we develop an analytical *Wentzel-Kramers-Brillouin* (WKB) treatment of the Surface Plasmon Polaritons (SPPs) propagation along linearly tapered waveguides, valid only for small taper angles. Next, we briefly outline a finite element hydrodynamic nonlocal solution of *Maxwell*'s equations

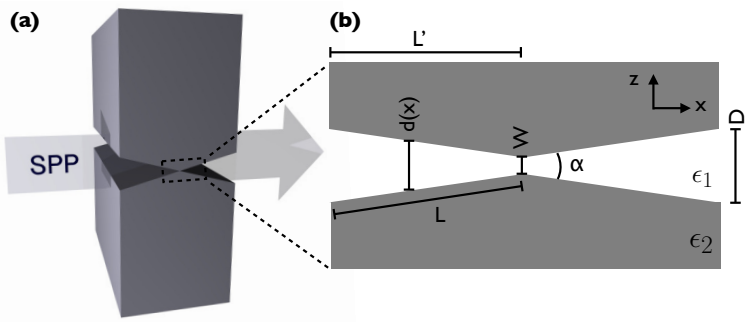


FIGURE 3.2: (a) 3D rendering of a linearly tapered MIM hourglass waveguide with translational invariance in the direction normal to the page (y-direction). The arrow indicates the direction of SPP propagation. (b) Schematic xz-plane view of the structure depicted in panel (a), with input gap thickness D, hourglass waist thickness W, arm length L', SPP path length L, and gap (metal) permittivity ϵ_1 and (ϵ_2). The hourglass angle α is measured wall to wall. Note that the x and z axes are displaced for clarity. The coordinate origin is located at the center of the hourglass waist.

suitable for arbitrary MIM geometries. Then, we use these theoretical tools to extend our investigation to hourglass structures, in which two tapered waveguides with opposite orientations are merged. Our theoretical results show that spatial dispersion drastically modifies the propagation characteristics of SPPs along tapered waveguides and geometric singularities [148; 37]. Remarkably, our predictions indicate that nonlocal effects makes the tunnelling of surface plasmons through thin metal contacts (~ 0.5 nm) possible.

3.1.2 Methods

First, we present an analytical WKB description [134; 148] of the SPP propagation along the hourglass waveguide schematically depicted in fig. 3.2 (a). The hourglass parameters used in our study, defined in fig. 3.2 (b), describe a tapered MIM stack of length $2L'$ and angle α (measured wall to wall). The gap thickness is reduced (increased) linearly from D to W (from W to D) in the region $-L' < x < 0$ ($0 < x < L'$). The length of the two waveguide arms along the x-direction, $L = L'\sec(\alpha/2)$, is chosen to ensure that the SPP optical path is of identical length for all taper angles α. The resultant x-dependent modulation of the gap thickness $d(x)$ can be expressed as $d(x) = 2\,|x|\tan(\alpha/2)$.

Our WKB description assumes that the reduction of the slab thickness along the direction of surface mode propagation in this hourglass waveguide takes place in a length scale much longer than the SPP effective wavelength. Within the WKB approximation, the electric field associated with the lowest plasmonic mode supported by the metal void can be expressed as [134]

$$E_z(x) = A(x)e^{i\phi(x)} \tag{3.1}$$

where $\phi(x) = \int_{-L'}^{x} k(x')dx'$ is a line integral corresponding to the phase accumulated by the SPPs along their optical path and $A(x)$ is a slowly varying amplitude factor ensuring power flow conservation. Within the WKB approximation, the propagation wavevector

$k(x')$ experiences only a small variation over a distance dx' (i.e., $|dk(x')^{-1}/dx'| \leq 1$) [45]. Therefore, for each position x, $k(x)$ can be obtained from the dispersion relation of an infinite, spatially dispersive, plasmonic MIM geometry with gap thickness $d(x)$. Treating nonlocality within the hydrodynamical *Drude* model we can calculate the dispersion relation of the lowest SPP mode supported by MIM waveguides, obtaining [114]

$$\tanh\left[q_1(x)d(x)/2\right] q_1(x)\epsilon_2 + q_2(x)\epsilon_1 + \frac{k(x)^2(\epsilon_2-\epsilon_1)}{q_3(x)} = 0 \tag{3.2}$$

where $q_i(x)$ $(i = 1, 2, 3)$ are the various normal wavevectors associated to the SPP mode: $q_1(x) = \left[k(x)^2 - \epsilon_1(\omega/c)^2\right]^{1/2}$ and $q_2(x) = \left[k(x)^2 - \epsilon_2(\omega/c)^2\right]^{1/2}$ correspond to the transverse wavevector components into free space and metal, respectively, and $q_3(x) = \left[k(x)^2 + [\omega_{\mathrm{P}}^2 - \omega(\omega + i\gamma)]/\beta^2\right]^{1/2}$ is the longitudinal plasmon wavevector into the metal. The permittivities of air and metal regions are respectively given by $\epsilon_1 = 1$ and $\epsilon_2 = \epsilon_{\mathrm{D}}(\omega)$, where $\epsilon_{\mathrm{D}}(\omega) = \epsilon_\infty - \omega_{\mathrm{P}}^2/[\omega(\omega + i\gamma)]$ denotes the local permittivity of the *Drude* metal with bulk plasma frequency ω_{P} and damping constant γ. c is the velocity of light. Note that in the limit $\beta = 0$, eq. (3.2) recovers the local dispersion relation [79]

$$\tanh\left[q_1(x)d(x)/2\right] q_1(x)\epsilon_2 = -q_2(x)\epsilon_1 \tag{3.3}$$

The amplitude factor in eq. (3.1) is fixed to satisfy energy conservation along the propagation direction. Thus, we have $A(x) \propto (\int_{-\infty}^{\infty} \langle S_x(z,x)\rangle\, dz)^{-1/2}$, where the time-averaged Poynting vector within the metal is given by

$$\langle S_x(z,x)\rangle \propto -\mathrm{Re}\{k(x)\epsilon_2^* e^{-2\mathrm{Re}\{q_2(x)\}z}\} \left| \frac{\epsilon_1}{\epsilon_2} \frac{e^{q_1(x)d(x)/2} + e^{-q_1(x)d(x)/2}}{e^{-q_2(x)d(x)/2}} \frac{1}{q_1(x)} \right|^2 \tag{3.4}$$

Similarly, the time-averaged Poynting vector outside the metal is given by

$$\langle S_x(z,x)\rangle \propto 2\mathrm{Re}\{k(x)\epsilon_1^* \left[\cosh(2\mathrm{Re}\{q_1(x)\}z) + \cosh(2\mathrm{Im}\{q_1(x)\}z)\right]\} \left| \frac{1}{q_1(x)} \right|^2 \tag{3.5}$$

The WKB description presented here does not take into account reflection and scattering effects experienced by the SPPs in their propagation along the surfaces of the metal void. This makes our description valid only for hourglass angles, α, which are consistent with the geometric assumptions presented above.

To overcome the limitations of the WKB approach we employ a Finite Element Method (FEM) solving strategy, based in the same hydrodynamical model for the metal permittivity. Within this nonlocal FEM numerical approach, which was introduced in more detail in section 2.3.2, the time harmonic electric field $\mathbf{E} = \mathbf{E}(\omega, \mathbf{r})$ associated with the SPP modes supported by an arbitrary metal nanostructure is described by the following set of coupled equations

$$\nabla \times (\nabla \times \mathbf{E}) = \frac{\omega^2}{c^2}\epsilon_\infty \mathbf{E} + i\omega\mu_0 \mathbf{J}_{\mathrm{d}} \tag{3.6}$$

$$\beta^2 \nabla[\nabla \cdot \mathbf{J}_\mathrm{d}] + \omega(\omega + i\gamma)\mathbf{J}_\mathrm{d} = i\omega\omega_\mathrm{P}^2 \epsilon_0 \mathbf{E}. \tag{3.7}$$

where the first and second source terms on the right hand side of the inhomogeneous *Maxwell* wave equation (eq. (3.6)) describe the positive background charge due to the ion cores and the nonlocal displacement current $\mathbf{J}_\mathrm{d} = \mathbf{J}_\mathrm{d}(\omega, \mathbf{r})$, respectively. We solve this wave equation simultaneously with eq. (3.7), the transport equation that governs the dynamics of the electron density in the metal. In this hydrodynamical approach, the first term of eq. (3.7) describes the effect of non-uniform electron density and the remaining ones are the usual *Drude* terms for a noninteracting electron gas. The nonlocal parameter β, which measures the impact of nonlocality, is proportional to the Fermi velocity in the metal [15]. It is closely related to the decay length δ_LP of the longitudinal plasmons excited in the metal structure due to spatial dispersion. Specifically, at frequencies well below the plasma frequency, ω_P, we can write $\beta \approx \delta_\mathrm{LP}\omega_\mathrm{P}$ [37]. Equation (3.7) can be used to derive nonlocal expressions for the longitudinal and transverse components of the dielectric function used in the derivation of eq. (3.2) [24]. Note that in the limit $\beta = 0$ eq. (3.7) recovers the local description, which provides us with the fitting parameters for the usual *Drude* permittivity.

Our FEM solving strategy for eqs. (3.6) and (3.7) follows the approach outlined in [143]. Utilising highly adaptive meshes resolving geometrical features as small as 0.1 nm, we solve these equations using *Comsol Multiphysics*, a state-of-the-art commercial FEM solver. In order to fully specify the coupled set of equations, the usual *Maxwell* boundary conditions for the continuity of the surface parallel EM fields have to be augmented by an additional boundary condition. Since the lattice constant (interionic distance) is similar to the *Coulomb* screening length (inter electronic distance) for noble metals such as Ag or Au, the appropriate additional condition for our problem is the continuity of the normal component of the electric field.

We note that both our WKB solution and our FEM approach omit electron tunnelling effects. Recent theoretical [156; 32; 82] and experimental [125; 127] studies have reported that plasmonic enhancement is significantly affected by electron tunnelling effects in the close encounter between metallic nanoparticles at optical frequencies.

3.1.3 Results and discussion

Figure 3.3 (a) plots the dispersion relation for the plasmonic modes supported by an infinite silver-air-silver MIM geometry of gap thickness d schematically depicted in fig. 3.3 (b). $\omega(k)$ only for the lowest SPP modes is shown. Note that the modal frequency and wavevector are normalized to the surface plasmon frequency, defined as $\mathrm{Re}(\epsilon_\mathrm{D}(\omega_\mathrm{SPP})) = -1$. Results for various gap thicknesses ranging from 1 nm to 50 nm are rendered. SPP bands obtained within the local ($\beta = 0$) and the nonlocal ($\beta = 0.0036c$)

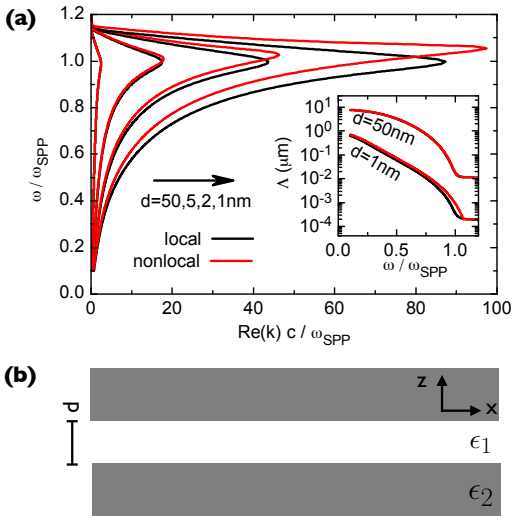


FIGURE 3.3: (a) Dispersion relation for the lowest SPP mode supported by a silver-air-silver MIM waveguide with gap thickness d, ranging from 1 nm to 50 nm. Black dashed (red solid) lines show local (nonlocal, $\beta = 0.0036c$) results. The inset renders the modal propagation length as a function of frequency. (b) Schematic of the infinite MIM geometry used in panel (a), fully characterised by the gap thickness d, gap permittivity ϵ_1 and metal permittivity ϵ_2. Reprinted with permission from Ref. [149]. Copyright 2013 by The Optical Society of America.

descriptions are plotted in black solid and red dashed lines, respectively. In all calculations, the local *Drude* constants were taken from the fitting to Ag experimental data [103] used in [148], and a realistic value of the parameter β for silver was considered in the nonlocal treatment [23]. Figure 3.3 shows that the reduction of the waveguide size red-shifts the SPP bands. At a fixed frequency, this band lowering with decreasing d can be interpreted as an increase of the mode binding to the structure surfaces [36]. This fact makes hourglass waveguides generated by the adiabatic reduction of d very suitable for light localisation purposes. Note that the insets of fig. 3.3 demonstrate the long propagation lengths ($\Lambda = (2\mathrm{Im}\{k\})^{-1}$) of these plasmonic modes over a wide spectral window, which reach many SPP wavelengths even for very small waveguide dimensions.

The comparison between local and nonlocal results in fig. 3.3 indicates that spatial dispersion blue-shifts the SPP frequencies in hourglass waveguides. This is a well-known nonlocal feature reported in the past for simple plasmonic waveguides [124] and nanoparticle geometries [122]. Note that the increase in $\omega(k)$ due to spatial dispersion is more pronounced for smaller d, where the thickness of the gap approaches the longitudinal plasmon decay length ($\delta_{\mathrm{LP}} \approx 0.1$ nm for realistic Ag parameters.)

Figure 3.4 renders the real part of the z-component of the electric field, E_z/E_0, along the surface of the waveguide defined in fig. 3.2 (b), with $L = 1000$ nm, $D = 60$ nm, $W = 0$ nm, and $\alpha = 3.44°$. Note that these parameters imply a geometrical singularity at the point $(x, y) = (0, 0)$. The fields have been normalized to the incident amplitude E_0. Both local (black) and nonlocal (red) results are rendered at $0.7\omega_{\mathrm{SPP}}$, where the modes depicted in fig. 3.3 (a) exhibit a convenient balance between confinement and

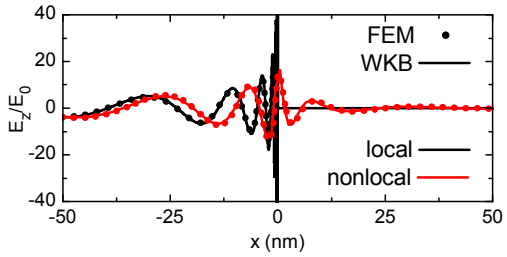


FIGURE 3.4: Real part of the electric z-field component (E_z/E_0) evaluated at $0.7\omega_{\mathrm{SPP}}$, plotted along the surface of a silver-air-silver plasmonic hourglass waveguide with $L = 1000$ nm, $D = 60$ nm and $W = 0$ nm. Dots and solid lines render FEM and analytical WKB calculations, respectively. Local (nonlocal) results are plotted in black (red). Reprinted with permission from Ref. [149]. Copyright 2013 by The Optical Society of America.

propagation length. This balance arises because, whilst the binding of modes to the metal surfaces is tighter at high frequencies, the propagation length increases towards lower mode energies due to the reduced absorption damping (see fig. 3.3 (a)). Excellent agreement between WKB analytical (lines) and FEM numerical (dots) results is obtained. Remarkably, we observe that in the nonlocal description SPPs are able to tunnel through the geometrical singularity located at $x = 0$ nm, penetrating into the non-illuminated side of the waveguide in the region $x > 0$. This is in contrast to the local limit, where SPPs are stopped adiabatically as they approach this singularity. Similar effects have been already reported theoretically in other singular MIM geometries that support EM surface modes. For example, as we have demonstrated in [37], the nonlocality enabled tunneling of SPPs has important consequences for kissing nanowire geometries, where it leads to a set of discrete nonlocal resonances that emerge below the surface plasma frequency. This tunnelling effect can be understood as a result of the smearing of the charge density in the nonlocal approximation, which prevents localizations of fields at very small distances (of the order of the *Thomas-Fermi* wavelength) [148].

In accordance with the band blue-shifting identified in fig. 3.3, fig. 3.4 reveals an increase in the effective wavelength of plasmonic modes in the nonlocal description, which is accompanied by a reduction in the field amplification that can be achieved. Both these nonlocal effects are strongest around $x = 0$ nm, and vanish in regions where the metal surfaces are far apart.

Up to this point we have restricted our study to waveguides at a fixed operating frequency. In fig. 3.5 (a) we lift this restriction by plotting the frequency dependent z-field amplitude $|E_z/E_0|$ at the waist of the hourglass waveguide as a function of frequency, for waist diameters ranging from 0.1 nm to 5 nm ($\alpha = 3.44°$). Note that we plot the component in the direction perpendicular to the metal surfaces (z-direction) as it is the one that undergoes the highest amplification. Local (black) and nonlocal (red) results are rendered, and good agreement between WKB analytical (lines) and FEM numerical

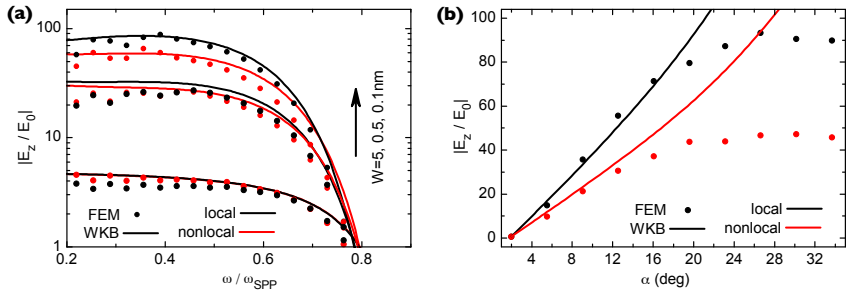


FIGURE 3.5: (a) Frequency dependent electric z-field amplitude enhancement $|E_z/E_0|$ evaluated at the waist of the waveguide, for different hourglass waist thicknesses W, for fixed $L = 1000$ nm and $\alpha = 3.44°$. Good agreement between WKB analytical (lines) and FEM numerical (dots) results is observed. Nonlocal and local predictions are shown in red and black, respectively (b) $|E_z/E_0|$ for $\omega = 0.7\omega_{\mathrm{SPP}}$, plotted as a function of the hourglass angle α. The hourglass waist is fixed to $W = 0.1$ nm, with all other parameters taking the same values as in panel (a). Reprinted with permission from Ref. [149]. Copyright 2013 by The Optical Society of America.

(dots) results is observed. Both descriptions yield a reduction of the field amplification at the hourglass waist at larger frequencies, which comes as a result of the increased metal absorption damping. The difference between local and nonlocal results is most pronounced for $W = 0.1$ nm, the narrowest hourglass waist thickness considered in fig. 3.5. In such diminutive junctions, the real part of the nonlocal wavevector in the SPP propagation direction decreases significantly due to spatial dispersion, which results in lower field enhancements due to the weaker SPP binding to the metal surfaces.

Next, we investigate the sensitivity of the device performance to variations in the hourglass angle α. In fig. 3.5 (b) we plot the α-dependent electric field, evaluated at $0.7\omega_{\mathrm{SPP}}$, at one of the walls of the hourglass waist for $W = 0.1$ nm (the smallest waist considered in fig. 3.5 (a)). Local (nonlocal) results are rendered in black (red). As α increases, a trend towards larger field enhancements is observed due to the significantly increased propagation length Λ of modes sustained by straight MIM geometries with large gap thicknesses (see the inset of fig. 3.3 (a)).

Note that we have fixed the SPP optical path, L, to 1000 nm for all α. Only this way, the effect of the tapering angle on the losses experienced by the SPP modes can be investigated. The comparison between WKB analytical results (lines) and FEM numerical results (dots) reveals good agreement between the two approaches for hourglass angles as large as $\alpha \sim 15°$. At larger angles, the WKB assumption of a reflection-free SPP propagation towards the hourglass waist breaks down, with significant reflection taking place as the modes accommodate to the rapidly changing geometry.

The dependence of the field enhancement at the hourglass waist on the taper angle is governed by two competing effects. On the one hand, increasing angles lead to larger propagation lengths, resulting in more efficient energy transfer and light localization. On the other hand, as α increases, the back scattering of SPPs caused by the metal walls

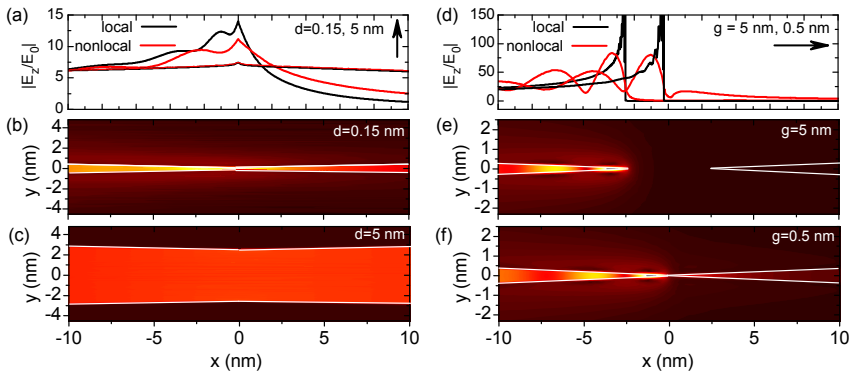


FIGURE 3.6: (a) $|E_z/E_0|$ evaluated at $0.7\omega_{\mathrm{SPP}}$, along the surface of a silver-air-silver plasmonic hourglass waveguide with length $L = 1000$ nm and input gap thickness $D = 60$ nm. Nonlocal (local) FEM numerical results are plotted in red (black). Results for hourglass waist thicknesses of both $W = 0.15$ nm and $W = 5$ nm are rendered. (b) and (c) Nonlocal $|E_z/E_0|$ map for the $W = 0.15$ nm and $W = 5$ nm cases in panel (a). (d) Same as panel (a), but for $W < 0$ ($g = W/(\tan(\alpha/2))$. Results for separation metal thicknesses of $g = 0.5$ nm and $g = 5$ nm are rendered. (e) and (f) Nonlocal $|E_z/E_0|$ map for the $g = 0.5$ nm and $g = 5$ nm cases in panel (d). Reprinted with permission from Ref. [149]. Copyright 2013 by The Optical Society of America.

becomes more pronounced, yielding lower field enhancements at the hourglass waist. Note that the latter effect is not described in our analytical WKB treatment of the system. For the geometric parameters considered in fig. 3.5 (b) the balance of these two effects leads to a maximum field enhancement at an angle $\alpha \sim 28°$ for both local and nonlocal predictions.

Finally, we consider the influence that the hourglass waist geometry has on the ability of SPPs to tunnel into the non-illuminated side of the waveguide ($x > 0$). Figure 3.6 (a)-(c) show results for open hourglass geometries ($W > 0$). Panel (a) plots the local (black) and nonlocal (red) z-field enhancement $|E_z/E_0|$ on the surface of the hourglass waveguide defined in fig. 3.2 (a)-(b), but for hourglass waist thicknesses of $W = 0.15$ nm and $W = 5$ nm. The fields are evaluated at $0.7\omega_{\mathrm{SPP}}$ using the FEM numerical approach. Nonlocal electric field maps for $W = 0.15$ nm and $W = 5$ nm are reproduced in panels (b) and (c), respectively. The comparison between local and nonlocal results in fig. 3.6 (a) reveals that the two models yield extremely similar results for $W = 5$ nm. This result can be understood from the dispersion bands in fig. 3.3 (a), which reveal that, for 5 nm layer width, local and nonlocal predictions for both k and Λ differ by only 0.2% at $\omega = 0.7\omega_{\mathrm{SPP}}$.

Large hourglass waist thicknesses enable efficient transfer of EM energy into the $x > 0$ region of the structure. This energy transfer is less efficient for smaller W, which in turn yield much larger field enhancement values. Figure 3.6 (a) shows these two effects for $W = 0.15$ nm, where the fields at the point $x = 10$ nm, located in the non-illuminated side of the waveguide, have dropped to less than half of the amplitude when compared to the $W = 5$ nm case. Interestingly, the nonlocal field amplitudes are larger than the local ones for most of the $x > 0$ region. This inversion results from absorption losses,

which are increased in the local case due to the significantly larger local SPP wavevectors (shorter effective wavelengths $\lambda_{\mathrm{SPP}} = 2\pi/k$). At $x = 0$ nm the effective wavelength of local and nonlocal SPPs are 5.3 and = 9.0 nm, respectively, which is in agreement with the periodicity observed in the reflection induced beating of $|E_z/E_0|$ apparent in fig. 3.6 (a).

Whilst the thinnest waist thicknesses considered in fig. 3.6 are interesting from a theoretical perspective, we note that the atomic spacing is on the same length scale (~ 0.1 nm) as the thinnest waists considered and so only an atomistic model will ultimately be able to provide quantitative results for this geometry.

Next, in fig. 3.6 (d)-(f), we consider the case of overlapping hourglass walls, characterised by $W < 0$. As W becomes negative, a metallic separation layer of thickness $g = W/\tan(\alpha/2)$ emerges in between the two arms of the waveguide, occupying the region $-g/2 < x < g/2$. Figure 3.6 (d) plots $|E_z/E_0|$ at $0.7\omega_{\mathrm{SPP}}$ along the hourglass walls of the same geometry considered in fig. 3.6 (a), but for negative values of W.

Structures with two metallic contact thicknesses, $g = 0.5$ nm and 5 nm, are considered. For of $g = 5$ nm the thick stopping layer is seen to be effective in terminating the SPP propagation within both the local (black lines) and nonlocal (red lines) descriptions. Interestingly, the thin metallic stopping layer ($g = 0.5$ nm) results in a behaviour which is both quantitatively and qualitatively different. As in the case of the singular geometry studied in fig. 3.4, we observe here that, whereas local SPPs are adiabatically stopped as they approach the hourglass waist, SPPs treated within the nonlocal model are able to tunnel across this metallic contact, as evidenced by the non-zero nonlocal field amplitude for $x > 0$ in fig. 3.6 (d) and (f). This result can be understood by considering the SPP group velocity, which in the local limit always approaches zero at the singularity. Thus, even for metallic stopping layers whose thickness is thinner than the skin depth, SPPs are unable to tunnel across adjacent metallic contacts, irrespective of their thickness. On the other hand, within the nonlocal description, the electronic charge distribution is smeared out across the metal boundaries, which increases the effective thickness of the dielectric region and, in turn, leads to a non-zero SPP group velocity even at geometrical singularities. This nonlocal smearing of surface charges is measured by the longitudinal plasmon decay length, which for the parameters considered in our calculations is $\delta_{\mathrm{LP}} \sim 0.1$ nm. This value sets the metal thicknesses g, for which nonlocal tunnelling of SPPs in tapered MIM waveguides takes place.

3.1.4 Conclusion

We have developed a nonlocal WKB solution for the propagation of SPPs along linearly tapered plasmonic hourglass waveguides. Effects of nonlocality were included using the hydrodynamical *Drude* model, and good agreement of these WKB analytical results

with a fully retarded nonlocal FEM numerical solution of the underlying equations was obtained. This formalism has enabled us to study the nanofocusing performance of plasmonic hourglass waveguides both analytically and numerically. Our results indicate that for a waist thickness of 0.1 nm spatial dispersion limits the field enhancements that can be achieved at the waist of metallic hourglass waveguides by up to a factor of two. Therefore, we can conclude that in terms of their nanofocusing performance, these devices are less sensitive to nonlocal effects than three dimensional metallic tips.[148] Interestingly, we have found that spatial dispersion enables SPPs to tunnel across metallic contacts as thick as 0.5 nm, which contradicts the usual vanishing surface plasmon group velocity predicted at sharp metallic contacts obtained within the local approximation. This effect is general and has ramifications for all singular metallic geometries that support SPPs, including kissing metallic nanowires [37], wedges [140] and nanocrescents. [34]

Finally, our nonlocal description of EM fields propagation provides a powerful tool for the determination of the parameters which optimize the light-concentration performance of tapered and hourglass plasmonic waveguides.

3.2 Nonlocal resonances in kissing plasmonic nanowires

3.2.1 Introduction

In the previous section we have found that Surface Plasmon Polaritons (SPPs) are able to tunnel through a singularity that exists at the waist of plasmonic hourglass waveguides. A related geometry is obtained when two metallic nanowires are brought into contact, as schematically depicted in fig. 3.7 (a). The physics of kissing metallic nanowires has been studied extensively using transformation optics [8; 71]. However, previous studies of this geometry were all done within the local approximation. In the local approximation SPP modes are excited on the surfaces of the two cylinders and propagate towards the touching point. As in the case of the metallic hourglass geometry investigated in the previous section, their group and phase velocities both tend to zero as they approach the singularity between the two cylinders, which means that the modes stop before reaching the singularity. This results in the characteristic (local) broadband absorption spectrum depicted by the grey line in fig. 3.9. In this case electromagnetic energy is only lost through scattering or absorption in the metal, with absorption being the dominant loss mechanism for small structures.

The fact that energy is mainly lost through absorption, combined with the restriction that the SPPs can at the most propagate for a distance equal to the circumference of one nanowire before they are adiabatically stopped at the touching point, leads to extremely large field amplitudes near the touching point (see for example the grey line in fig. 3.8). Specifically, the maximum field amplitude predicted by local results occurs always at a

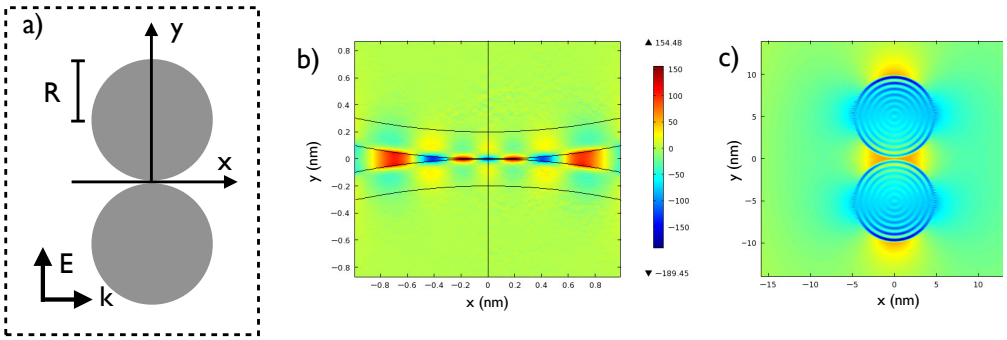


FIGURE 3.7: (a) Sketch of kissing metallic nanowires enclosed in vacuum with the incident field polarised along the dimer axis. (b) FEM results for nonocal E_y at around the touching point and at 7 eV. (c) nonocal E_y in the bulk of the nanowires at 8.5 eV. All results are for for a *Drude* metal with $\epsilon_\infty = 1$, $\omega_p = 8$ eV, $\gamma = 0.01\omega_p$ and $\beta = 0.001c$. The fields are normalised so that the pointing vector of the incident plane wave is unity.

finite distance away from the touching point. This point separates the regime of growing fields from the regime of decaying fields. There are two variables which control whether fields grow or decay in a nanofocusing waveguide: large angles and low energies lead to growing fields, whereas small angles and high energies lead to decaying fields. In the case of two touching nanowires, whether fields grow or decay is determined by the local gradient of the nanowire surfaces.

3.2.2 Methods

Our study of the system of two touching nanowires takes into account nonlocal effects using the hydrodynamical *Drude* model. Results are calculated using the nonlocal Finite Element Method (FEM) implementation presented in section 2.3.2, and these results are compared against a nonlocal transformation optics description developed by *Fernandez-Domingez et al.* [37].

3.2.3 Results and discussion

When studying a system of two touching metallic cylinders[2] with our nonlocal FEM method the nearfields are modified from the local predictions in two critical ways: Firstly, for energies above the bulk plasma frequency (depicted in fig. 3.7 (b)) characteristic longitudinal bulk modes appear. As in the case of a single nanowire, these bulk modes lead to additional peaks in the absorbtion cross sections above the bulk plasma frequency (not explicitly shown here). Secondly, in the local case fields adiabatically stop at the touching point without ever propagating past this geometrical singularity. Our nonlocal

[2]We use *Drude* fitting parameters which ensure a very close fit to the experimental data for silver obtained by Palik. The parameters we have determined are $\omega_{\text{Palik}} = 3.82\text{eV}$, $\epsilon_\infty = 3.46 + 0.256i$, $\omega_p = 2.248\omega_{\text{Palik}}$, $\gamma = 0.02\omega_{\text{Palik}}$, $\omega_{\text{SPP}} = 4.06\text{eV}$.

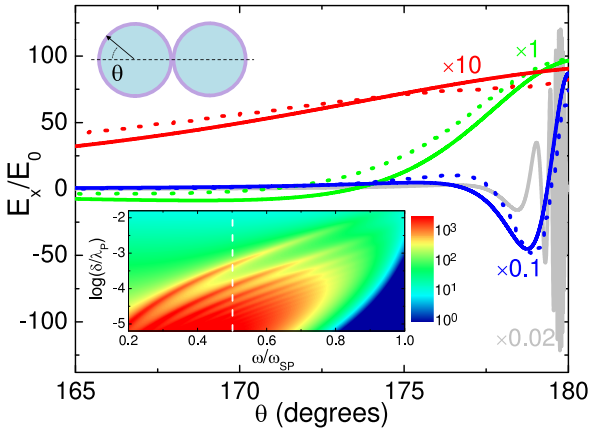


FIGURE 3.8: Field enhancement in the vicinity of the touching point of two 10 nm radii Ag nanowires at $\omega = 0.5\omega_{\mathrm{SP}}$ and different degrees of nonlocality, $\delta/\lambda_{\mathrm{P}}$: 10^{-4} (blue), 10^{-3} (green) – this is a realistic value for Ag – and 10^{-2} (red). Solid (dotted) lines show transformation optics [37] (numerical) results. Grey line plots Ex/E0 under the local description. The inset displays $|E_x/E_0|$ at the touching point as a function of the incident frequency, $\omega/\omega_{\mathrm{SP}}$ and $\delta/\lambda_{\mathrm{P}}$. The white dashed line indicates the operating frequency in the main panel. Reprinted with permission from Ref. [37]. Copyright 2012 by the American Physical Society.

FEM result (fig. 3.7 (b)) shows a nonzero field amplitude at the touching point. This suggests that in the nonlocal case SPPs can sneak past the touching point and propagate round and round the structure. In effect, the smearing of the charge density over the metal surface which is implicit in our nonlocal scheme leads to an effective separation of the two cylinders, making their broadband response qualitatively similar to that of two nearly touching nanowires [9].

The extent to which longitudinal fields can penetrate into the metal regions is dependent on the degree of nonlocality. Below the bulk plasma frequency the longitudinal modes are always damped out and their decay length is of the order of a few angstroms. We can give an estimate of the decay length by considering the dispersion relation for the longitudinal plasmons

$$k_{\perp}^2 = k_{\parallel}^2 + \frac{1}{\beta^2}\left[\omega_{\mathrm{P}}^2 - \omega(\omega + i\gamma)\right], \tag{3.8}$$

For frequencies well below the bulk plasma frequency the decay length $\delta = 1/k_L$ can be written

$$\delta = \frac{\beta}{\omega_P} = \frac{\beta\lambda_p}{c} \tag{3.9}$$

In this section we will indicate the degrees of nonlocality not in terms of the hydrodynamic parameter β but in terms of δ/λ_p.

In fig. 3.8 we show the fields near the touching point explicitly. We see that nonlocality leads to a non-zero amplitude of the fields at the touching point. This means that SPPs are able to propagate past the touching point and circulate round the cylinders for one or more revolutions. Figure 3.8 also shows a reduction in the maximum field enhancement

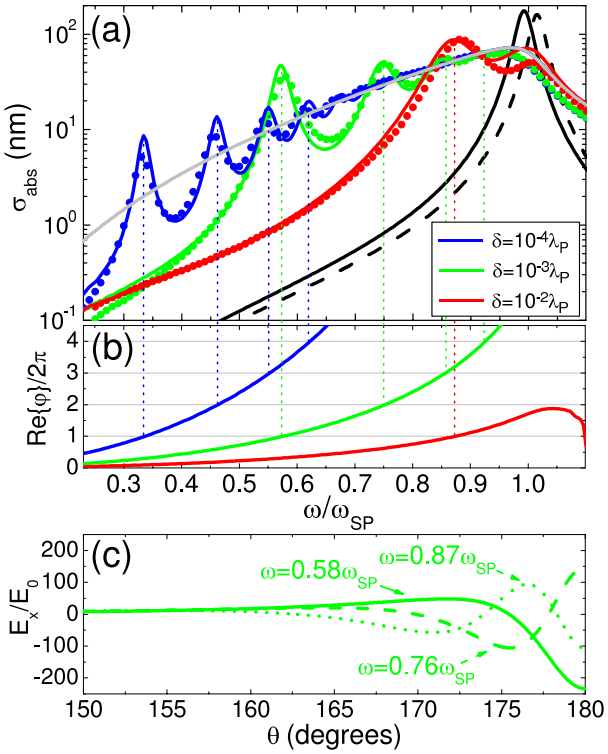


FIGURE 3.9: Theoretical [37] (solid lines) and numerical (dots) absorption spectra for 10 nm radii nonlocal nanowires, together with the cross section obtained within the local approximation (grey dashed line). σ_{abs} for a local (nonlocal, $\delta = 10^{-2}\lambda_{\text{P}}$) single nanowire is also plotted in solid (dashed) black line. Panel (b): Real part of the phase accumulated by the circulating surface plasmon modes in one loop around the nanowires. (c) Field enhancement close to the touching point at the three lowest nonlocal resonances for $\delta = 10^{-3}\lambda_{\text{P}}$ (value appropriate for silver). Reprinted with permission from Ref. [37]. Copyright 2012 by the American Physical Society.

as the degree of nonlocality is increased, with the green line rendering the result for a realistic degree of nonlocality.

Figure 3.8 shows excellent agreement between my FEM results (dots) and the transformation optics results obtained by *Fernandez-Domingez et al.* (lines). The advantage of a transformation optics approach in this context is that it allows for the exploration of large parameter spaces which would be difficult to explore by running often very time consuming FEM simulations. For example, the insert of fig. 3.8 shows transformation results for the nonlocal field enhancement at the touching point as a function of frequency and the degree of nonlocality. Keeping the frequency fixed, we clearly identify a resonant behaviour, with field maxima occurring at distinct degrees of nonlocality.

To investigate the origin of the resonant behaviour identified in the insert of fig. 3.8 we look for characteristic fingerprints of these resonances in the absorption cross section. Figure 3.9 (a) shows the absorption cross section for a pair of touching nanowires within the local approximation (grey line) and for different degrees of nonlocality (colour lines). The black lines show results for a single cylinder in the local approximation (solid line)

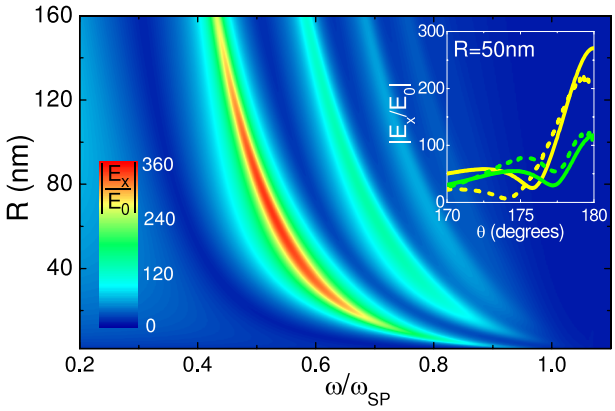


FIGURE 3.10: Absolute value of the field enhancement at the touching point as a function of ω/ω_{SP} and R. Solid (dashed) lines in the inset render theoretical [37] (numerical) —Ex/E0— at the two lowest enhancement maxima for R = 50 nm: $0.55\omega_{SP}$ (yellow), $0.72\omega_{SP}$ (green). Results are for for Ag with $\beta = 3.6\times10^{-3}$c. Reprinted with permission from Ref. [37]. Copyright 2012 by the American Physical Society.

and when taking into account nonlocality (dashed line). Figure 3.8 (b) shows transformation optics results for the phase accumulated by the SPPs after one revolution. This explains the origin of the nonlocal resonances which were predicted by our FEM results. Nonlocality allows SPPs to sneak past the touching point, leading to resonance peaks in the absorption cross section whenever the phase accumulated by the SPP during one revolution is equal to a multiple of 2π.

One of the important conclusions of our study is that the inclusion of nonlocality enables us to predict an optimal size parameter for maximum field enhancement with touching nanowires. Radiative losses become larger as the radii of the touching nanowires is increased. For this reason local predictions suggest that decreasing radii would lead to increasing field enhancements without bound, leading to the erroneous conclusion that an infinitely small set of nanowires would offer the highest field enhancements. However, our results show that nonlocal effects limit field enhancement in small structures, thus providing the physical ingredient which was necessary for the determination of an optimal size parameter for nanofocusing with touching nanowires. In Figure 3.10 we plot transformation optics results for the nonlocal field enhancement at the touching point between two nanowires as a function of frequency and radius. The results are validated through FEM results in the insert. Importantly, fig. 3.10 shows that the inclusion of nonlocality leads to the prediction that the maximum field enhancement obtainable with a set of touching silver nanowires is achieved for radii between 20 nm and 100 nm.

3.2.4 Conclusion

In section 3.1 we have used the geometry of a Two-Dimensional (2D) metallic hourglass to show that, in the nonlocal case, SPPs are able to tunnel through a geometrical singularity which terminates them in the local case. In this section, we have taken this

result to inspire our study of kissing nanowires, where it has lead us to identify a set of new nonlocal resonances in the visible spectrum. These resonances are sensitive to the degree of nonlocality and our tests show that they are robust in large structures of up to approximately $R = 200$ nm.

3.3 Nonlocal effects in the nanofocusing performance of plasmonic tips

3.3.1 Introduction

In the previous sections we have considered nonlocal effects in two geometries that were translationally invariant in the z-direction. In this section we go beyond this restriction, investigating how nonlocal effects alter the nanofocusing performance of three-dimensional plasmonic tips operating in the optical regime. First, we present a three-dimensional Finite Element Method (FEM) nonlocal solution of *Maxwell*'s equations that exploits the rotational symmetry of the system. Then, we derive an analytical *Wentzel-Kramers-Brillouin* (WKB) (or eikonal [17]) description of the Electromagnetic (EM) fields propagation along perfectly shaped conical tips. The combination of both approaches enables us to extend the validity of previous local calculations [134; 80] into the sub-nanometer length scale, which is crucial for light localization purposes. Moreover, our FEM model allows us to analyze more complex, experimentally relevant, geometries where the WKB treatment is not applicable. In particular, we investigate how spatial dispersion modifies the EM fields sensitivity to the presence of roughness in the tip surface and the bluntness of its apex end, which are inevitable features in realistic devices. We demonstrate that nonlocal effects modify drastically the nanofocusing performance of plasmonic tips when the size of the structure imperfections are comparable to the *Coulomb* screening length.

3.3.2 Methods

We summarise first the fundamentals of our nonlocal FEM model, which was introduced in more detail in section 2.3.2. The time harmonic electric field associated with the SPP modes supported by an arbitrary metal nanostructure, $\mathbf{E}(\omega)$, is described by the inhomogeneous wave equation

$$\nabla \times (\nabla \times \mathbf{E}) = \frac{\omega^2}{c^2}\epsilon_\infty \mathbf{E} + i\omega\mu_0 \mathbf{J}_\mathrm{d} \tag{3.10}$$

where the first and second source terms describe the positive background charge due to the ion cores and the nonlocal displacement current, respectively. Within the hydrodynamical *Drude* model, the transport equation for the nonlocal current $\mathbf{J}_\mathrm{d}$ reads

$$\beta^2\nabla[\nabla\cdot\mathbf{J}_\mathrm{d}]+\omega(\omega+i\gamma)\mathbf{J}_\mathrm{d}=i\omega\omega_\mathrm{P}^2\epsilon_0\mathbf{E}. \tag{3.11}$$

Equation (3.11) governs the dynamics of the electron density. The first term describes the effect of non-uniform electron density and the remaining ones are the usual *Drude* terms for a noninteracting electron gas. The nonlocal parameter β is equal, except for an adimensional factor, to the Fermi velocity of the metal [15]. It is closely related to the decay length δ_LP of the longitudinal plasmons excited in the metal structure due to spatial dispersion. Thus, at frequencies well below the plasma frequency, ω_P, we can write $\beta\approx\delta_\mathrm{LP}\omega_\mathrm{P}$ [37]. Note that in the limit $\beta=0$ eq. (3.11) recovers the local description, which provides us with the fitting parameters for the usual *Drude* permittivity, $\epsilon_\mathrm{D}(\omega)=\epsilon_\infty-\omega_\mathrm{P}^2/[\omega(\omega+i\gamma)]$.

We follow the approach outlined in Ref. 143 to solve eqs. (3.10) and (3.11) simultaneously on a highly adaptive mesh using *Comsol Multiphysics*, a commercial FEM package. We take advantage of the rotational symmetry of the system (note that both the metallic tip and the EM fields are azimuthally independent) to map our three-dimensional problem into a two-dimensional one. The usual *Maxwell* boundary conditions for the continuity of the EM fields have to be augmented by an additional boundary condition. Since the lattice constant (interionic distance) is similar to the *Coulomb* screening length (interelectronic distance) for noble metals such as Ag or Au, the appropriate additional condition for our problem is the continuity of the normal component of the electric field. This completes our nonlocal FEM implementation.

Our analytical WKB description of the Surface Plasmon Polariton (SPP) propagation along a conical plasmonic tip assumes that the reduction of its cross sectional area along the direction of propagation (z direction) takes place in a length scale much longer than the SPP effective wavelength. Under this approximation, the electric field associated with the azimuthally independent plasmonic mode supported by the metal tip can be expressed as [134]

$$E(z)=A(z)e^{i\phi(z)} \tag{3.12}$$

where $\phi(z)=\int_0^z k(z')dz'$ corresponds to the SPP optical path and $A(z)$ is a slowly varying amplitude factor ensuring power flow conservation. Within the WKB approximation, the propagation wavevector $k(z)$ experiences only a small variation over a distance dz' (i.e., $|dk^{-1}/dz'|\leq 1$) [45]. Therefore, for each position z, $k(z)$ can be obtained from the dispersion relation of an infinitely long, spatially dispersive, metallic wire of radius $R=R(z)$ [124]

$$\frac{h^2}{q_3}\frac{I_0\left(q_3R\right)}{I_1\left(q_3R\right)}\left(\epsilon_D-1\right)+\epsilon_D q_1\frac{K_0\left(q_1R\right)}{K_1\left(q_1R\right)}+q_2\frac{I_0\left(q_2R\right)}{I_1\left(q_2R\right)}=0 \tag{3.13}$$

where I_0 and I_1 (K_0 and K_1) denote the modified Bessel functions of the first (second) kind, and q_i ($i = 1, 2, 3$) are the various normal wavevectors associated with the SPP mode: $q_1 = \sqrt{k^2 - (\omega/c)^2}$ and $q_2 = \sqrt{k^2 - \epsilon_{\mathrm{D}}(\omega)(\omega/c)^2}$ (where c is the velocity of light) correspond to the transverse wavevector components into free space and metal, respectively, and $q_3 = \sqrt{k^2 + [\omega_{\mathrm{P}}^2 - \omega(\omega + i\gamma)]/\beta^2}$ is the longitudinal plasmon wavevector into the tip. Note that in the limit $\beta = 0$ eq. (3.13) recovers the local dispersion relation for the azimuthally independent plasmon modes in cylindrical metallic wires [36].

As mentioned above, the amplitude factor is fixed to satisfy energy conservation along the z direction. Thus, we have $A(z) \propto 1/\sqrt{\int_0^R \langle S_z(r,z)\rangle\, dr}$, where the time-averaged Poynting vector within the cylindrical wire is given by $\langle S_z(r,z)\rangle \propto \mathrm{Re}(k)\,|I_1(q_2 r)/q_2|^2$. Note that the analytical description presented here does not take into account reflection and scattering effects experienced by the plasmonic mode in its propagation along the metal tip. This makes our description valid only for acute apex angles, α, which is consistent with the WKB assumptions presented above.

3.3.3 Results and discussion

Figure 3.11 plots the dispersion relation for the plasmonic modes supported by a silver slab (panel a) and a cylindrical shaped silver wire (panel b). $\omega(k)$ for only symmetric (azimuthally independent) SPP modes is shown in the former (latter) panel. Note that the modal frequency and wavevector are normalized to the surface plasmon frequency, defined as $\mathrm{Re}(\epsilon_{\mathrm{D}}(\omega_{\mathrm{SPP}})) = -1$. Results for various slab thicknesses and wire diameters (both labelled as d) ranging from 1 nm to 50 nm are rendered. SPP bands obtained within the local ($\beta = 0$) and the nonlocal ($\beta = 0.0036c$) descriptions are plotted in black solid and red dashed lines, respectively. In all calculations, the local *Drude* constants were taken from the fitting to Ag experimental data [103] (see Appendix A1), and a realistic value of the parameter β for silver was considered in the nonlocal treatment [115]. Figure 3.11 shows that the reduction of the waveguide size red-shifts the SPP bands for both geometries. At a fixed frequency, this band lowering with decreasing d can be interpreted as an increase of the mode binding to the structure surface [36]. This fact makes wedges and conical tips generated by the adiabatic reduction of d in these two geometries very suitable for nanofocusing purposes. Note that the insets of fig. 3.11 demonstrate the long propagation lengths ($\delta = 1/\mathrm{Im}(k)$) of these plasmonic modes over a wide spectral window, which reach many SPP wavelengths even for very small waveguide dimensions.

The comparison between local and nonlocal results in fig. 3.11 indicates that, for both structures, spatial dispersion blue-shifts the SPP frequencies. This is a well-known nonlocal feature reported in the past for simple plasmonic waveguides [124] and nanoparticle geometries [122]. Importantly, the impact of spatial dispersion is larger in the nanowire geometry, which is a direct consequence of the larger $\mathrm{Re}(k)$ (note the different

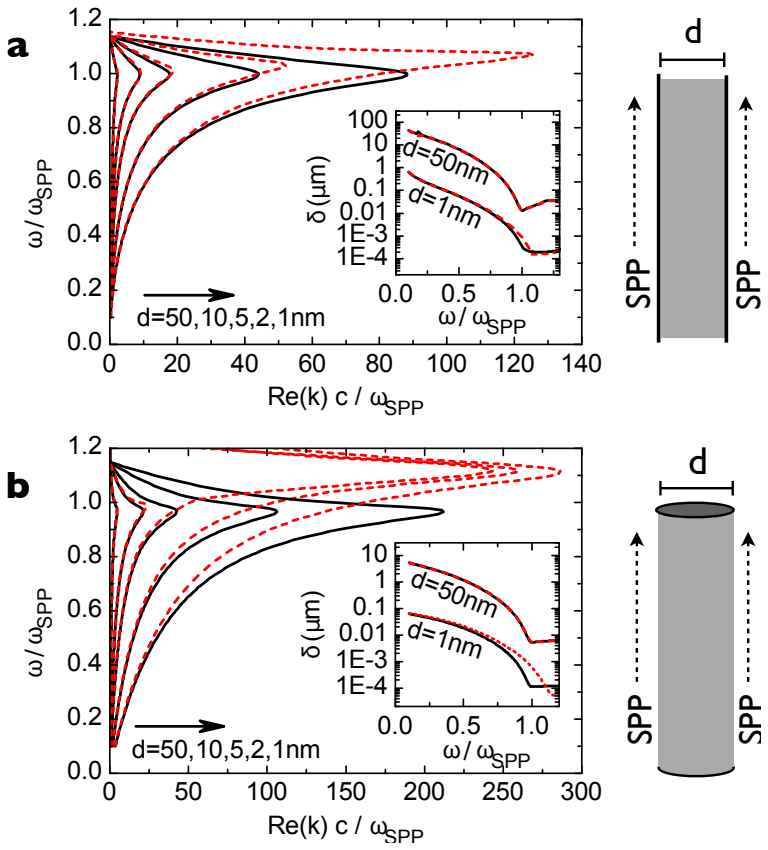


FIGURE 3.11: (a) Dispersion relation for the symmetric SPP mode supported by silver slabs of thickness d. Black solid (red dashed) lines show local (nonlocal, $\beta = 0.0036c$) results. The inset renders the modal propagation length as a function of frequency. (b) The same as (a) but for the azimuthally independent SPP mode suported by silver cylinders of diameter d. In both panels, the SPP frequency and wavevector are normalized to the surface plasmon frequency, defined as $\mathrm{Re}(\epsilon_{\mathrm{D}}(\omega_{\mathrm{SPP}})) = -1$. Reprinted with permission from Ref. [148]. Copyright 2012 by the American Chemical Society.

horizontal scales in fig. 3.11) and hence, the higher confinement of the modes in this structure. Thus, the fact that conical tips are more efficient nanofocusing devices than wedges, also makes them more sensitive to nonlocal effects. Note as well that the increase in $\omega(k)$ due to spatial dispersion is more pronounced for smaller d, as the diameter of the nanowire approaches the longitudinal plasmons decay length ($\delta_{\mathrm{LP}} \approx 0.16$ nm for realistic Ag parameters).

Figure 3.12 (a) shows the radial component of the electric field,E_r, along the surface of a silver conical tip of length $L = 1.5\mu$m and apex angle $\alpha = 6°$. E_r is evaluated at $\omega = 0.6\omega_{\mathrm{SPP}}$, where the SPP bands infig. 3.11 show a convenient balance between absorption damping and field confinement. We have chosen the radial component (normal to the tip surface at the apex position) in analogy with recent studies on the light-harvesting properties of touching nanoparticles [8; 35]. Predictions for the local (black) and nonlocal (red) model of the silver tip permittivity are displayed, and both WKB analytical (solid lines)and FEM simulated (crosses) results are shown. Note that the electric fields are

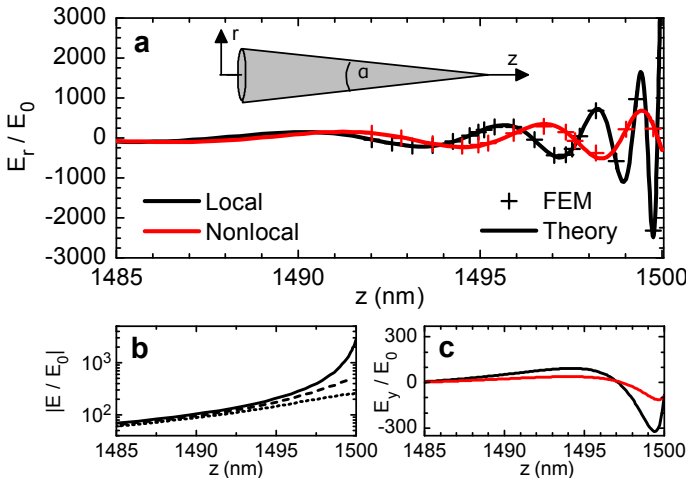


FIGURE 3.12: (a) Enhancement in the radial component of the electric field along the surface of a plasmonic Ag tip with $L = 1.5\mu$m and $\alpha = 6°$ evaluated at $\omega = 0.6\omega_{\rm SPP}$. WKB (lines) and FEM (crosses) calculations are shown for both a local (black) and nonlocal (red) description of the tip dielectric response. (b) Absolute value of the electric field in the same geometry as in panel (a) within the local approximation (solid line) and for two values of β: $0.0036c$ (dashed line) and $0.01c$ (dotted line). (c) Normal component of the electric field along the surface of a Ag wedge of the same dimensions as (a) and (b) at $\omega = 0.6\omega_{\rm SPP}$. Panels (b) and (c) show WKB results. In all panels, the EM fields are normalized to the input amplitude E_0. Reprinted with permission from Ref. [148]. Copyright 2012 by the American Chemical Society.

normalized to their input value E_0. Remarkably, our theoretical solutions are in excellent agreement with numerical calculations without the introduction of any fitting parameter.

In agreement with the modal wavevector reduction predicted by fig. 3.11, the introduction of nonlocal effects in the field enhancement calculations in fig. 3.12 (a) gives rise to a stretching of the effective SPP wavelength (defined as $2\pi/k$). This effect frustrates the extremely efficient nanofocusing ability of the plasmonic modes, as they are no longer able to accommodate to the tip geometry in their propagation towards its apex end. This leads to a field enhancement reduction at this position which, at the frequency of operation in fig. 3.12 (a), is about one order of magnitude. To further analyze this effect, we study analytically in fig. 3.12 (b) how the electric field amplitude along the tip surface is modified when the nonlocal parameter is varied from $\beta = 0$ (local, solid line) to$\beta = 0.0036c$ (realistic value, dashed line) and $\beta = 0.01c$ (overestimation, dotted line). WKB field enhancement calculations for a plasmonic wedge with the same dimensions and the same operating frequency are rendered in fig. 3.12 (c). This panel indicates that, as we had already anticipated, the nanofocusing efficiency in wedge geometries is less pronounced than in the conical tips.

The effective wavelength stretching and field amplitude reduction illustrated in fig. 3.12 are the two most prominent nonlocal effects taking place in plasmonic tips. In order to gain further physical insight into their origin, we analyze in fig. 3.13 the different components of the electric field along the same conical tip at $0.6\omega_{\rm SPP}$. Panels (a) (top)

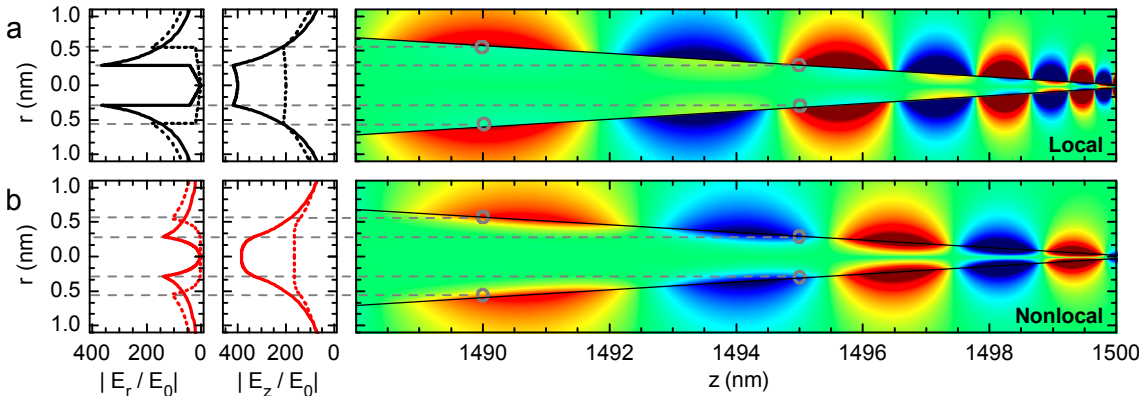


FIGURE 3.13: Local (a) and nonlocal (b) electric fields at $\omega = 0.6\omega_{SPP}$ along the conical tip geometry considered in fig. 3.12 (a). The right contour plots show E_r maps within the symmetry plane of the structure. The left panels plot the radial and parallel components of the electric field 5nm (solid lines) and 10nm (dotted lines) away from the apex. In all cases, fields are normalized to the input amplitude, E_0. The saturated color scale in the contour plots ranges from -100 (blue) to 100 (red). Reprinted with permission from Ref. [148]. Copyright 2012 by the American Chemical Society.

show local results and panels (b) (bottom) render nonlocal calculations, both obtained from FEM simulations. The right contour plots displayE_r within the symmetry plane of the structure, whereas the left linear plots render the radial and parallel components of the electric field evaluated 5 (solid lines) and 10 nm (dotted lines) away from the tip apex. Figure 3.13 shows clearly the fundamental fingerprint of spatial dispersion on SPP waves, the smoothing of the associated electric field across themetal-dielectric interface. Although this effect modifies slightly the parallel component of the electric field, its impact is more apparent in the radial component (which is discontinuous in the local approximation). The comparison between the local and nonlocal radial electric field profiles in fig. 3.13 demonstrates that the introduction of spatial dispersion removes the electric field discontinuity at the boundaries of the plasmonic tip. Importantly, the E_r maps show that, as a consequence of this increased field penetration into the metal structure, the effective wavelength of the SPPs does not shrink as efficiently as in the local description in the travel towards the tip end.

So far, we have focused our analysis on the impact that nonlocal effects have in the SPP-assisted concentration of light taking place in a fixed tip geometry at a given operating frequency. In fig. 3.14, we expand our study by investigating how the nanofocusing efficiency depends on these two aspects, which enables us to optimize the performance of the device. The main panel of fig. 3.14 (a) shows WKB (solid lines) and FEM (crosses) results for the amplitude enhancement, $|E/E_0|$,at the apex of the conical tip in fig. 3.13 ($L = 1.5\mu$m,$\alpha = 6°$) as a function of frequency. Local (black) and nonlocal (red) results are shown. Both descriptions yield a reduction of the field enhancement at larger frequencies, caused by the increase of metal absorption damping. Interestingly, the difference between local and nonlocal predictions (which is of one order of magnitude at low

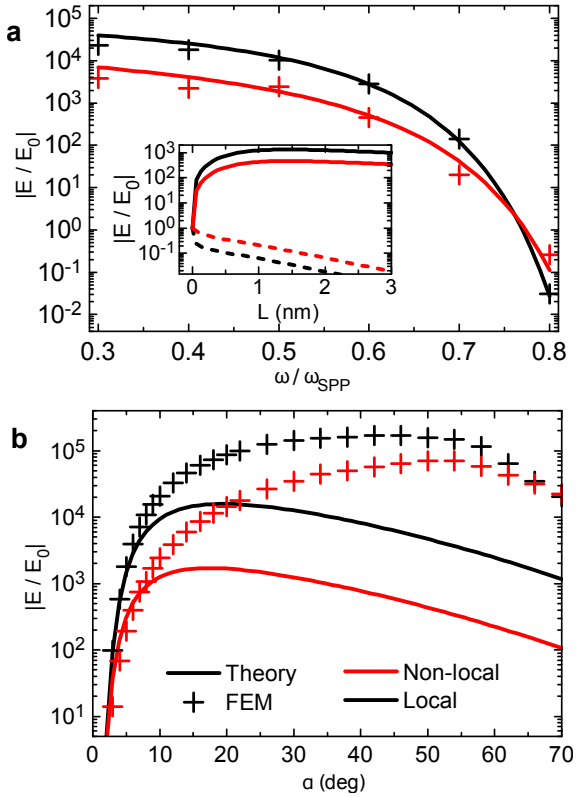


FIGURE 3.14: (a) Absolute value of the field enhancement, $|E/E_0|$, at the tip end as a function of the operating frequency for $L = 1.5\mu$m and $\alpha = 6°$. The inset renders local (black) and nonlocal (red) $|E/E_0|$ obtained from WKB calculations at $0.6\omega_{\mathrm{SPP}}$ (solid lines) and $0.8\omega_{\mathrm{SPP}}$ (dashed lines) as a function of the tip length ($\alpha = 6°$). (b) Electric field enhancement as a function of the tip angle evaluated at $\omega = 0.6\omega_{\mathrm{SPP}}$. Reprinted with permission from Ref. [148]. Copyright 2012 by the American Chemical Society.

frequencies) decreases with frequency. At $\omega \approx 0.75\omega_{\mathrm{SPP}}$, the inclusion of spatial dispersion in the silver permittivity seems to benefit the focusing efficiency, and the nonlocal values for $|E/E_0|$ exceed the local ones. This originates from the blue-shift experienced by the nonlocal SPP bands in fig. 3.11 (b), which effectively widens the operation bandwidth of the device. Therefore, the inclusion of spatial dispersion effectively improves the nanofocusing performance of plasmonic tips at frequencies approaching the surface plasmon frequency.

The inset of fig. 3.14 (a) plots analytical $|E/E_0|$ evaluated at the end of the tip ($\alpha = 6°$) as a function of the device length. Solid and dashed lines correspond to operating frequencies of $0.6\omega_{\mathrm{SPP}}$ and $0.8\omega_{\mathrm{SPP}}$, respectively. Colors indicate the local/nolocal character of the results as in the main panel. These WKB calculations demonstrate that metal losses reduce drastically the focusing efficiency as the frequency approaches ω_{SPP}. Note that, for all tip lengths, the nonlocal enhancement is larger than the local result at$0.8\omega_{\mathrm{SPP}}$. As mentioned above, the impact of absorption losses in the field enhancement at the tip apex is the same in both descriptions. This is due to the fact that we are using a hydrodynamic model with a real β parameter. This is a excellent approximation

for silver in the optical regime, as the collision frequency γ is much smaller than the operation frequency ω [50].

The apex angle is the geometric parameter that governs the tip performance. This is demonstrated in fig. 3.14 (b), which shows the field enhancement at the tip end as a function of α for $L = 1.5\mu$m and $\omega = 0.6\omega_{\mathrm{SPP}}$. Notice that, whereas the WKB (solid lines) and FEM (crosses) results agree at small angles ($\alpha \leq 10^{\circ}$), they yield very different predictions for obtuse α. This discrepancy indicates the breakdown of the WKB solutions, which occurs at angles in which the variation of the tip radius along the direction of propagation is faster than the EM fields oscillation. This causes the scattering into free space of the SPP modes in their travel towards the tip end, which is not included in the WKB picture. Figure 3.14 (b) demonstrates that the inclusion of this effect increases $|E/E_0|$ for both local (black) and nonlocal (red) descriptions. This is an anti-intuitive result, as one would expect that the radiation damping would diminish the nanofocusing efficiency. However, for the parameters considered here, the forward scattering suffered by the SPP modes effectively reduces their sensitivity to absorption losses, hence increasing the field enhancement at the tip end.

The forward scattering of the SPP modes also explains why WKB calculations predict a heavier impact of spatial dispersion in the device performance in fig. 3.14 (b). This is due to the fact that the binding of the EM fields is tighter in this case than in the more accurate FEM simulations. The interplay between radiation, absorption and nonlocal effects give rise to an optimum apex angle, α_{opt} which maximizes $|E/E_0|$. In accordance with our interpretation, our WKB approach underestimates this angle, which FEM simulations place at $\alpha_{\mathrm{opt}} \approx 50^{\circ}$. Note that the local and nonlocal FEM predictions for α_{opt} are very similar. Remarkably, while local field enhancements are 10 times larger for sharper tips, both descriptions yield a maximum enhancement of $|E/E_0| \approx 10^5$. This enables us to conclude that the effect of spatial dispersion in the performance of plasmonic tips is minimized if the device is operating at optimum conditions.

The introduction of nonlocal effects makes possible a more realistic description of the light concentration in plasmonic tips. However, up to here we have restricted our study to idealized perfectly shaped conical geometries. In the following, we explore numerically the consequences of two of the most relevant structural imperfections in these devices: the apex bluntness and surface roughness. We consider first bluntness effects, which are known to have strong influence on the plasmonic response of sharp nanostructures [75]. Figure 3.15 (a) plots the absolute value of the electric field along the z direction (see inset) in the surroundings of the tip end ($L = 1.5\mu$m and$\alpha = 10^{\circ}$) at $\omega = 0.6\omega_{\mathrm{SPP}}$. It shows a characteristic evanescently decaying SPP tail at increasing distances from the structure apex. Three different blunt geometries are considered, characterized by the apex diameterD_{out} (0.1, 0.5 and 1 nm). Local (black) and nonlocal(red) fields are normalized to their value at the surface of the tip end, which clarifies the dependence of the fields confinement on D_{out}. The bluntness of the apex leads to a spill outof the EM

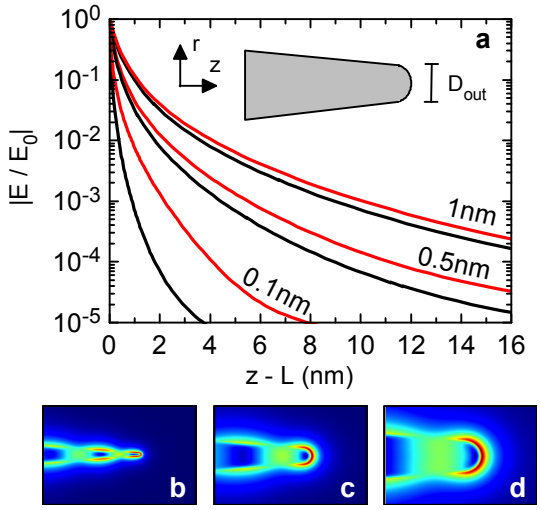


FIGURE 3.15: (a) Absolute value of the electric field ($\omega = 0.6\omega_{\mathrm{SPP}}$) in the vicinity of three different blunt plasmonic tips ($L = 1.5\mu$m, $\alpha = 10^{\circ}$) characterized by the apex diameter D_{out}. Local (black) and nonlocal (red) FEM calculations are shown. In all cases, the fields are normalized to their value at the tip surface. Panels (b), (c) and (d) display nonlocal near field amplitude maps for $D_{\mathrm{out}} = 0.1$, 0.5, and 1 nm, respectively. Reprinted with permission from Ref. [148]. Copyright 2012 by the American Chemical Society.

fields into free space. This spreading of the SPP tail is more pronounced in the nonlocal calculations. This is another consequence of the weaker binding of the EM fields and the metal boundary smoothing induced by spatial dispersion already discussed in fig. 3.13. As expected, the discrepancies between local and nonlocal descriptions increase as D_{out} shrinks and approaches the longitudinal plasmon decay length, δ_{LP}. The three lower insets of fig. 3.15 display nonlocal near field amplitude maps in the vicinity of the tip ends considered in panel (a).

Finally, we explore the effect that the presence of a sub-nanometer roughness decorating the plasmonic tip surface has on its nanofocusing performance. It is well known that subwavelength structural imperfections, inevitable in any waveguiding device, increase the radiation damping experienced by SPP waves [112]. We investigate here how the presence of spatial dispersion in the dielectric response of silver affects the robustness of bound EM fields against this additional scattering mechanism. We consider the same tip geometry as in fig. 3.15, and model the tip roughness through the introduction of a random modulation of the metal boundary with a 0.25 nm average period and a height ranging from -0.25 to 0.25 nm (realistic profile for current nano fabrication capabilities). Figure 3.16 (a) plots the field enhancement at the tip end as a function of the frequency for both the local (black) and nonlocal (red) models. Our analysis on smooth tips indicated that local $|E/E_0|$ are higher than nonlocal ones at low frequencies. However, according to fig. 3.16 (a), once surface imperfections are taken into account, nonlocal calculations exceed local results for any operating frequency. Again, this is a clear manifestation of the smearing out of the metal-vacuum interface associated with

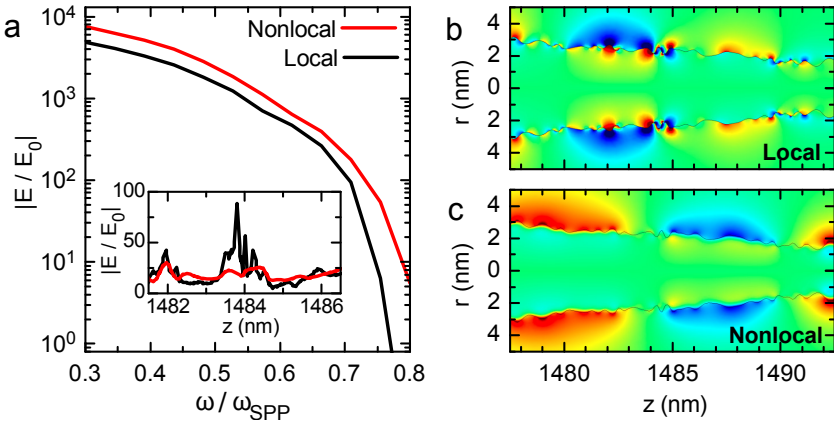


FIGURE 3.16: (a) Absolute value of the local (black lines) and nonlocal (red lines) electric field on the surface of a silver cone of length $L = 1500$ nm and angle $\alpha = 10$ deg. The surface roughness is achieved by radially displacing points on the surface every 0.25 nm by a random number in the range -0.25 nm to $+0.25$ nm. The inset renders the fields on the surface of the cone. (b) Contour plot of the local radial electric field at $\omega = 0.8\omega_{\mathrm{SPP}}$ for the cone used in panel a. (c) Contour plot of the nonlocal radial electric field ($\omega = 0.8\omega_{\mathrm{SPP}}$) for the cone used in panel a. Reprinted with permission from Ref. [148]. Copyright 2012 by the American Chemical Society.

the excitation of longitudinal plasmons in the nonlocal description. As we have seen, this reduces the binding of the SPP modes to the metal surface and decreases their sensitivity to geometric irregularities.

The comparison between fig. 3.16 and fig. 3.14 allows us to quantify the impact that surface roughness scattering has on the focusing efficiency of SPP modes, both within the local and nonlocal descriptions. Remarkably, the former yields a field enhancement reduction by a factor of 4.7 at $0.6\omega_{\mathrm{SPP}}$, whereas this factor drops to only 1.04 in the nonlocal case. In order to gain insight into this result, we plot $|E/E_0|$ along the tip surface in the inset of fig. 3.16 (a) ($\omega = 0.6\omega_{\mathrm{SPP}}$). It shows the emergence of sharp intense electric field maxima in the local model which are smoothed and lowered once nonlocal effects are taken into account. This strong interaction with the surface imperfections leads to the formation of strong radiation foci in the local case. This is demonstrated in fig. 3.16 (b) and fig. 3.16 (c), which display the local and nonlocal electric field amplitude maps within the same tip region. The upper panel shows the presence of these strongly radiating hot- spots which interrupt the waveform of the SPP mode and act as strong radiation centres, preventing the EM fields from propagating towards the tip. In contrast, these hot-spots are removed in the lower panel, proving that the introduction of spatial dispersion restores the SPP waveform along the plasmonic tip surface, resembling closely the electric field map in fig. 3.13. The robustness of the nonlocal description to surface roughness is due to the fact that the corrugation size is comparable to the decay length of the longitudinal plasmons, δ_{LP}.

Up to this point we considered a surface roughness based on a pitch of 0.5 nm. We

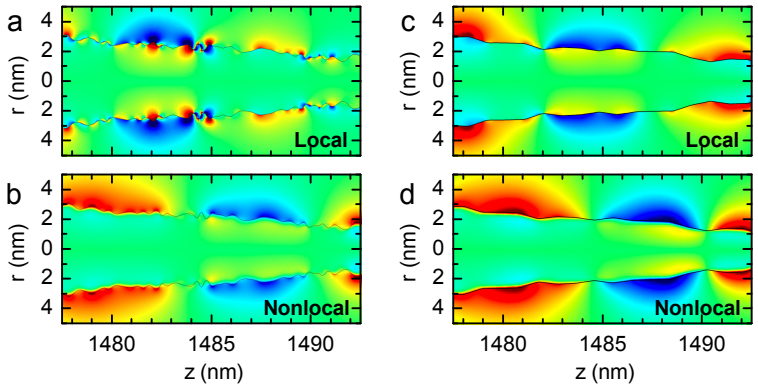


FIGURE 3.17: Contour plots of the local (top) and nonlocal (bottom) radial electric fields at $\omega = 0.8\omega_{\mathrm{SPP}}$ in an Ag tip with $L = 1500$ nm and $\alpha = 10°$. In all cases, the surface roughness is achieved by radially displacing points on the surface by a random number in the range -0.25 nm to $+0.25$ nm. Panels (a) and (b) show results based on points spaced 0.25 nm away from each other along the surface. In panels (b) and (c) the spacing between points on the surface was increased to 1 nm. The points form the basis of the cubic spline interpolation which defines the metal dielectric interface. The saturated color scale ranges from $E_r/E_0 = -35$ (blue) to $E_r/E_0 = 35$ (red). Reprinted with permission from Ref. [148]. Copyright 2012 by the American Chemical Society.

now explore increased surface roughness, showing that the local and nonlocal descriptions result in similar behaviour of the fields when the characteristic length scale of the corrugation is much larger than the penetration length of the longitudinal plasmons.

First, in fig. 3.17 (a) and (b), we plot results for a smaller corrugation size than in the text above (the pitch of the surface roughness is decreased to 0.25 nm and the height modulation is from -0.25 nm to $+0.25$ nm). The maps of the radial electric fields show the emergence of strong radiation foci in the local model, which are smoothed and lowered once nonlocal effects are considered.

In contrast to this, fig. 3.17 (c) and (d) render results for a large corrugation size (the pitch of the surface roughness is increased to 1 nm and the height modulation is from -0.25 nm to $+0.25$ nm). In this case the interaction with the surface imperfections is weakened, leading to the removal of the radiation foci already in the local case.

3.3.4 Conclusion

We have studied theoretically how spatial dispersion in the dielectric response of metals modifies the nanofocusing ability of plasmonic tips. We have shown that nonlocal effects diminish significantly the field enhancement taking place at the apex of sharp structures. At more obtuse geometries, the device efficiency is optimized and the impact of nonlocality is strongly inhibited. Finally, we have also demonstrated that spatial dispersion increases the robustness of plasmonic tips performance against structural imperfections such as apex bluntness and surface roughness.

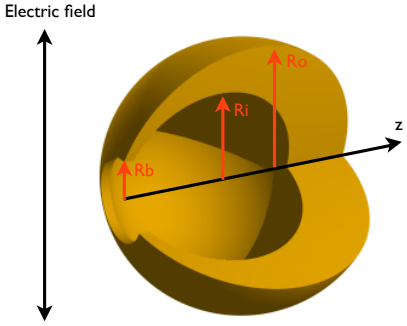


FIGURE 3.18: Schematic depiction of a metallic nanocrescent, rotationally symmetric around the z-axis, with outer radius R_o and inner radius R_i. The structure is blunted through a hole of radius R_b which is cut at the thin end of the crescent. Plane wave illumination, polarised perpendicular to the z-axis, is incident from the thin side of the crescent.

3.4 Nonlocal effects in three-dimensional nanocrescent light harvesters

3.4.1 Introduction

In the previous section we have used the geometry of tapered plasmonic tips to illustrate how Localised Surface Plasmons (LSPs) have the ability to beat the diffraction limit, which allows them to collect and concentrate light into deeply subwavelength volumes with extreme efficiency [97]. In this section we consider metallic nanocrescents (schematically depicted in fig. 3.18), which present a related but more intricate platform for nanofocusing.

The remarkable field localisation ability of Surface Plasmon Polaritons (SPPs) supported by nanofocusing devices, which is a clear manifestation of their hybrid electromagnetic-wave and surface-charge nature, is strongly dependent on the geometry, material characteristics and environment of the metallic structures sustaining them. The exploitation of the sensitivity of LSPs to all these circumstances has made possible an unprecedented control of light and light-matter interactions at the nanoscale. This fact has driven the emerging field of plasmonics [79] and has already yielded a wide range of novel LSP based photonic devices [7; 98; 53].

Recently, intense research efforts have been devoted to devise, fabricate, and characterize plasmonic nanostructures with different functionalities [43; 47]. Among the profusion of designs investigated, dielectric core, metallic shell nanoparticles (usually termed nanoshells) have stood out for their extreme tunability [48]. The appropriate choice of the inner dielectric material and the core and shell relative sizes allows the tailoring of the nanoshell's LSPs within the whole optical spectrum [137; 11]. From an experimental side, these metallodielectric compounds have proven to be particularly accessible through a broad range of nanofabrication techniques [135; 111]. From a theoretical perspective,

the optical properties of spherical core-shell geometries can be described accurately using *Mie* theory [2], yielding a remarkable agreement with experimental observations [10; 94]. More recently, sophisticated numerical treatments beyond classical electromagnetics have been also developed [110]. All these factors have made possible the realization of nanoshell plasmonic devices in technological areas as diverse as molecular sensing [113], cancer therapy [54], or fluorescence microscopy [131].

Nanoshells present a large effective cross section, which enables them to interact strongly with the incident light. However, their LSP resonances do not yield near-field hot spots as intense as those produced by structures with very small or sharp geometry features, such as dimer or trimer nanoantennas [64]. Lately, a strategy to improve the focusing performance of nanoshells has been proposed. It consists in breaking the symmetry of the nanostructure by displacing the center of the dielectric core and the metal shell [146]. Note that this also adds new structural degrees of freedom, increasing the tunability of the device [20; 69]. Experimental reports indicate that the nanoparticles resulting from this operation (usually termed nanoeggs or nanocups, depending on the inter-center distance relative to the shell radius) exhibit larger near-field enhancements than nanoshells, while retaining similar extinction efficiencies [73; 151; 145]. So far, an analytical treatment of these reduced symmetry nanostructures is still lacking, and only numerical methods make possible a quantitative description of their optical properties [62; 119]. Moreover, whereas the hybridization concept [109] yields a clear physical picture of nanoshell LSPs, its insightfulness diminishes with increasing degree of structural asymmetry.

Recently, a Transformation Optics (TO) approach [106] able to unveil hidden symmetries in complex plasmonic devices has been developed. The method was first devised to describe analytically the optical properties of two-dimensional (2D) nanostructures [8; 77], but it has been also successfully applied to the case of a dimer of touching nanospheres [35]. Recently, this three-dimensional (3D) framework has been extended to crescent-shaped nanoparticles (nanocrescents) [34]. This geometry arises when the displacement of the dielectric core in a nanoshell is such that it leads to a single point where the metal thickness vanishes. This new TO method yields analytical expressions for all the significant electromagnetic magnitudes in nanocrescents, revealing the efficient and tunable (polarization insensitive) light harvesting performance of the device over the whole optical spectrum.

By truncating singular Two-Dimensional (2D) nanostructures, experimentally feasible geometries are obtained which can be described quasi-analitically using TO [75; 76]. In this section we study the equivalent geometry in 3D, demonstrating the robustness of the plasmonic response of blunt, nanocup-like structures against structural defects. We employ numerical calculations, based on the Finite Element Method (FEM) formalism introduced in section 2.5, to investigate the impact of spatial dispersion in sub-nanometer

thick shells. This calculation allows us to quantify the impact of nonlocal effects on the field enhancement and nanofocusing ability of nanocrescents.

3.4.2 Methods

In our nonlocal FEM model, which is exposed in more detail in section 2.3.2, the time harmonic electric field supported by an arbitrary metal nanostructure, $\mathbf{E}(\omega)$, is described by the inhomogeneous *Maxwell* wave equation

$$\nabla \times (\nabla \times \mathbf{E}) = \frac{\omega^2}{c^2}\epsilon_\infty \mathbf{E} + i\omega\mu_0 \mathbf{J}_\mathrm{d} \tag{3.14}$$

where the first and second source terms describe the positive background charge due to the ion cores and the nonlocal displacement current, respectively. Within the hydrodynamical *Drude* model, the transport equation for the nonlocal current $\mathbf{J}_\mathrm{d}$ reads

$$\beta^2 \nabla[\nabla \cdot \mathbf{J}_\mathrm{d}] + \omega(\omega + i\gamma)\mathbf{J}_\mathrm{d} = i\omega\omega_\mathrm{P}^2\epsilon_0\mathbf{E}. \tag{3.15}$$

Equation (3.15) governs the dynamics of the electron density. The first term describes the electron-electron interactions and the remaining ones are the usual *Drude* terms for a noninteracting electron gas. The nonlocal parameter β, which measures the strength of the electronic interactions, is equal, except for an adimensional factor, to the Fermi velocity of the metal [15]. It is closely related to the decay length δ_LP of the longitudinal plasmons excited in the metal structure due to spatial dispersion. Thus, at frequencies well below the plasma frequency, ω_P, we can write $\beta \approx \delta_\mathrm{LP}\omega_\mathrm{P}$ [37]. Note that in the limit $\beta = 0$ Equation (3.15) recovers the local description, which provides us with the fitting parameters for the usual *Drude* permittivity, $\epsilon_\mathrm{D}(\omega) = \epsilon_\infty - \omega_\mathrm{P}^2/[\omega(\omega + i\gamma)]$. In our study, the *Drude* parameters were obtained by fitting to the experimental data for gold [60] at every frequency point and the nonlocality parameter was set to $\beta = 0.0036c$, where c is the speed of light.

We follow the approach outlined in Ref. 142 to solve Equations (3.14) and (3.15) simultaneously on a highly adaptive finite element mesh using *Comsol Multiphysics*. In the special case of crescents which are small compared to the wavelength of the axially polarised illumination, we neglect retardation effects and take advantage of the rotational symmetry of the system (note that both the crescent geometry and the Electromagnetic (EM) fields are azimuthally independent) to map our three-dimensional problem into a two-dimensional one. The usual *Maxwell* boundary conditions for the continuity of the EM fields have to be augmented by an additional boundary condition. Since the lattice constant (interionic distance) is similar to the *Coulomb* screening length (interelectronic distance) for noble metals such as Ag or Au, the appropriate additional condition for our problem is the continuity of the normal component of the electric field.

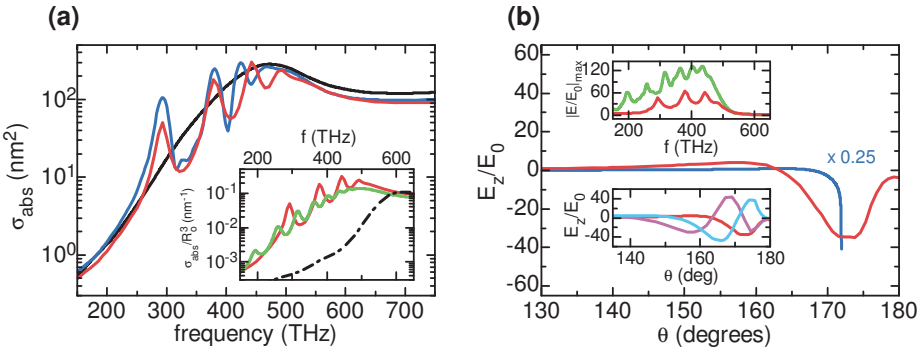


FIGURE 3.19: (a) Absorption cross section of gold nanocrescents with $R_o = 10$ nm and $\tau = 0.85$. The red (blue) line renders the nonlocal (local) spectrum for the singular (blunt) geometry with $R_b = 0$ ($R_b = 1$ nm). For comparison, the singular, local cross section is plotted in black line. The inset shows nonlocal σ_{abs}/R_o^3 for singular crescents with 10 (red) and 40 (green) nm outer radius, together with the nonlocal spectrum for a solid nanosphere (black). (b) Field enhancement versus θ for the lowest absorption maximum in the nonlocal (red) and blunt (blue) spectra in (a). The lower inset shows E_z/E_0 for the three lowest nonlocal resonances in (a). The upper panel plots the maximum $|E_z/E_0|$ versus frequency for $R_o = 10$ (red) and 40 (green) nm crescents within the nonlocal approximation. Reprinted with permission from Ref. [34]. Copyright 2012 by the American Chemical Society.

3.4.3 Results and discussion

Recent studies, based on a spatially dispersive treatment of the dielectric response of plasmonic materials [148; 37], have shown that nonlocal effects can modify the propagation of electromagnetic surface modes in plasmonic structures which are shaped on sub-nanometer length scales. The main effects due to nonlocality are a reduction of the achievable field enhancement, as well as a decrease in the confinement of LSP modes. In this section we investigate the effects of non locality in nano crescents using a quasi-three-dimensional, spatially dispersive, finite element simulation, outlined in section 3.4.2.

Figure 3.19 (a) compares the absorption cross section of a singular crescent treated within the nonlocal model (red curve) with the absorption cross section of the same device treated within the local approximation (black curve). We find that the introduction of spatial dispersion leads to the emergence of discrete resonance peaks in the nonlocal absorption cross section, reminiscent of those found for blunted crescents. For comparison, the blue curve in Figure 3.19 (a) renders the local absorption cross section for a blunted crescent. Interestingly, the result for the blunted crescent (blue curve) shows a qualitative resemblance to the result obtained for the singular crescent within the nonlocal model (red curve). The number of nonlocal resonance peaks increases with the size of the crescent, as illustrated by the inset of Figure 3.19 (a), which compares the normalized absorption cross section for crescents with outer radius $R_o = 10$ nm and $R_o = 40$ nm.

To further analyse the origin of the nonlocal absorption peaks found in Figure 3.19 (a), we plot in Figure 3.19 (b) the electric field on the surface of the crescents. The main panel plots E_z/E_0 at 290 THz, the frequency of the lowest nonlocal resonance. At that frequency, the nonlocal field on the surface of the singular crescent (red curve) changes sign only once as it approaches the thin end of the crescent. The lower inset of Figure 3.19 (a) replots this curve and compares it to the one obtained at the second lowest (blue curve) and third lowest (pink curve) nonlocal resonance. At each resonance, the number of sign changes of the field increases by one, demonstrating that the nonlocal resonances are due to constructive interference from LSPs which are reflected as they approach the geometrical singularity at $\theta = 180°$.

Within our nonlocal model, the non-vanishing charge distribution at the metal surfaces is taken into account through the non locality parameter $\beta \approx \delta_{\mathrm{LP}}\omega_{\mathrm{P}}$. Here δ_{LP} is the decay length of the longitudinal plasmons, whose magnitude is comparable to the coulomb screening length of the metal. This leads to an important difference between the local and the nonlocal description of wave propagation in plasmonic structures. Whereas in the local description SPPs are able to accommodate to arbitrarily thin metallic structures, the decay length of the longitudinal plasmons $\delta_{\mathrm{LP}} \sim 0.1$ nm limits the degree of mode confinement that can be achieved. In the case of an LSP propagating towards the thin end of a nanocrescent this means that the effective wavelength of the SPP decreases in its travel towards the singularity, however at the point where the thickness of the metallic shell is of the order δ_{LP} no further mode confinement is possible and the SPP undergoes reflection. It is this reflection which leads to the nonlocal absorption peaks found in Figure 3.19 (a). For comparison, the blue curve in the main panel of Figure 3.19 (b), corresponding to the blue absorption curve in Figure 3.19 (a), shows the local field on a crescent which was blunted in such a way that the thinnest part of the crescent has a thickness of $2\delta_{\mathrm{LP}}$. Even though the local near field of this blunted crescent is both qualitatively and quantitatively different from that found in a nonlocal singular crescent, comparison of the absorption cross sections in Figure 3.19 (a) shows that the two models lead to comparable behaviours in the far field.

Finally, we investigate the degree to which nonlocal effects limit the field enhancement that can be achieved on the surface of nanocrescent devices. The main panel of Figure 3.19 (b) shows that the field on a blunted crescent with outer radius $R_{\mathrm{o}} = 10$ nm can reach up to $|E_z/E_0| = 160$ at the lowest resonance in the local limit. When a singular crescent of the same size is considered with the inclusion of nonlocal effects, the field enhancement at the lowest resonancedrops to $|E_z/E_0| = 34$. However, as the upper inset of Figure 3.19 (b) shows, the maximum nonlocal field enhancement is frequency dependent, reaching up to $|E_z/E_0|_{\mathrm{max}} = 60$ for a crescent with $R_{\mathrm{o}} = 10$ nm (red curve) and up to $|E_z/E_0|_{\mathrm{max}} = 130$ for a crescent with $R_{\mathrm{o}} = 40$ nm (green curve).

In the main text we have shown how the introduction of spatial dispersion leads to the emergence of discrete resonances in singular nanocrescents with relatively thin metal

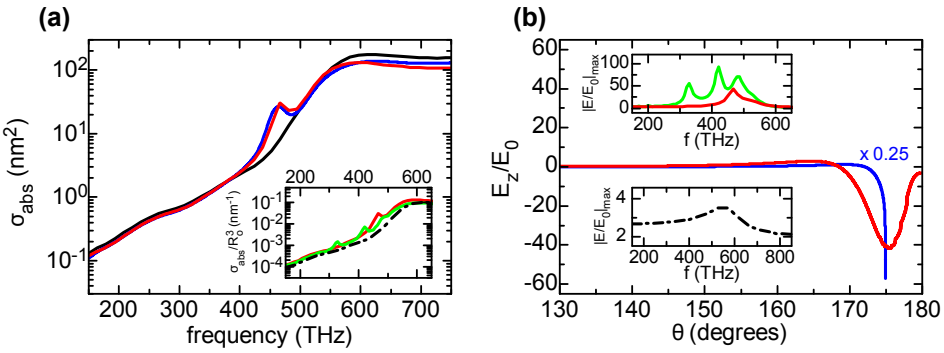


FIGURE 3.20: (a) Absorption cross section of gold nanocrescents with $R_o = 10$ nm and $\tau = 0.5$. The red (blue) line renders the nonlocal (local) spectrum for the singular (blunt) geometry with $R_b = 0$ ($R_b = 0.88$ nm). For comparison, the singular, local cross section is plotted in black line. The inset shows nonlocal σ_{abs}/R_o^3 for singular crescents with 10 (red) and 40 (green) nm outer radius, together with the nonlocal spectrum for a solid nanosphere (black). (b) Field enhancement versus θ for the lowest absorption maximum in the nonlocal (red) and blunt (blue) spectra in (a). The lower inset shows nonlocal $|E/E_0|_max$ for a solid nanosphere (a). The upper panel plots the maximum $|E_z/E_0|$ versus frequency for $R_o = 10$ (red) and 40 (green) nm crescents within the nonlocal approximation. Reprinted with permission from Ref. [34]. Copyright 2012 by the American Chemical Society.

shells ($R_o = 10$ nm and $\tau = 0.85$). In this section we show that the effect is robust to a thickening of the metal shell.

In Figure 3.20 we plot the nonlocal absorption cross section (red curve) for a singular nanocrescent with $\tau = 0.5$, comparing it to the local cross section for the same geometry (black curve). As in the case discussed in the main text, we find that the introduction of spatial dispersion interrupts the broadband absorption behaviour of the device through the emergence of nonlocal resonances (for the case shown here there is a single nonlocal resonance at 450 THz).

For an aspect ratio of $\tau = 0.5$, a bluntness radius of 0.88 nm ensures that the metal thickness at the cup edge is twice the longitudinal plasmon decay length ($\gamma_{LP} \sim 0.1$ nm for gold). The blue curve in Figure 3.20 (a) plots the local absorption cross section for a nanocusp with this bluntness radius. The quantitative and qualitative similarity of this result to the nonlocal singular result (red curve) suggests that nonlocality leads to a reflection of LSPs in the regions where the shell thickness drops below $2\gamma_{LP}$. The inset of Figure 3.20 (a) shows that if the outer radius of the crescent with $\tau = 0.5$ is increased, additional nonlocal resonance peaks emerge. For comparison, the black line plots the nonlocal absorption cross section for a solid nanosphere.

In Figure 3.20 (b) we demonstrate the impact of nonlocality on the field enhancement ability of the device. The main panel shows $|E_z/E_0|$ versus θ for the nonlocal resonance (450 THz) in the nonlocal (red) and blunt (blue) spectra in Figure 3.20 (a). The upper inset of Figure 3.20 (b) plots the maximum field enhancements that can be achieved on crescents of different outer radii (top inset). Despite the relatively thick metal shell

($\tau = 0.5$) these field enhancements are significantly larger than those which can be achieved on the surface of a nonlocal sphere (bottom inset).

3.4.4 Conclusion

Summarizing, we have performed a rotationally symmetric nonlocal FEM study revealing the electromagnetic properties of three dimensional nanocrescents. Our approach incorporates both bluntness effects, inevitable in any nano fabrication strategy, as well as effects of radiative damping, significant in devices where the geometrical cross section leads to scattering of electromagnetic energy into the far field. Applying these methods, we have obtained deep insights into the geometrical and material properties which control the performance of nanocrescent light harvesters. Finally, a spatially dispersive solution of *Maxwell*'s equations on a finite element mesh was used to determine the effects of nonlocality in nanocrescents with subnanometer shells, revealing a set of nonlocal resonances in singular nano crescents, as well as a reduction of the maximum field enhancement. Crucially, we find that despite adverse effects of nonlocality, field enhancements of more than 100 can be achieved in a gold nanocrescent with diameter 80 nm and inner radius 34 nm.

3.5 Probing the nonlocal response using electron beam excitation

3.5.1 Introduction

Up to this point, all the studies presented in this thesis have been restricted to two-dimensional or axially symmetric three-dimensional space. Even though this has allowed us to make significant progress towards the understanding of nonlocal effects in plasmonic nano-structures, there remain many experimentally relevant geometries which are not amenable to such simplifications, requiring instead a full three-dimensional treatment. For example, Electron Energy Loss Spectroscopy (EELS) [30; 31] offers a powerful technique that enables the non-perturbative experimental near-field mapping of the photonic local density of states [40; 55] with sub-nanometer spatial resolution [18; 95]. This capability makes EELS an excellent candidate for the study of the nonlocal response of metallic nanostructures [101; 116; 127; 128]. From the theoretical side, spatial dispersion in electron microscopy of simple metallic geometries has been thoroughly analyzed in the past [29; 154; 108; 117]. However, the interpretation of EELS spectra from complex plasmonic devices has been limited for two reasons: First, even though general solutions of *Maxwell*'s equations have been developed to describe the response of these systems driven by an electron beam [95], their operation was restricted to the local limit. Secondly, in cases where full nonlocal Electromagnetic (EM) solutions were used, the

underlying models were limited to plane wave excitation [116], with the implementation of an EELS excitation source in the nonlocal regime still lacking. Importantly, EELS sources offer access to the whole modal spectrum, whereas optical excitation only probes the so-called bright modes, which couple strongly with radiation. Thus, compared to focused illumination, the exploration of nonlocal effects through EELS promises more complete information about the interplay between nonlocality and geometry.

In this section, we develop for the first time a full three-dimensional hydrodynamic nonlocal solution of *Maxwell*'s equations in the frequency domain [148] that implements the EELS source as a line current. This configuration mimics common experimental setups, and we show that the resultant equations can be readily solved using *Comsol Multiphysics*. We then use our numerical approach to perform a comprehensive study of the emergence of nonlocal effects in connected gold nanoprisms, exploring all the relevant parameters of the system, and revealing the physical implications of spatial dispersion in this geometry. Finally, we use our theoretical model to gain insights into a set of EELS experimental results obtained by other authors. [147] The experimental results we consider were obtained for lithographically-defined gold bowties connected by bridges as narrow as 1.6 nm. This comparison enables us to assess the impact of quantum effects in the EM properties of these plasmonic systems. Our study reveals that the effect of nonlocality on the EELS spectra for the nanoprisms connected by the narrowest (1.6 nm) bridge is masked by quantum confinement and grain boundary electron scattering effects. The experimental results we consider indicate that these effectively show the absorption damping experienced by the plasmon modes supported by the nanostructure.

3.5.2 Theory

In an EELS experiment, electrons with a fixed kinetic energy in the 100 keV range are directed along a linear path passing close to a plasmonic target. These fast electrons excite localized surface plasmons, thereby transferring part of their kinetic energy to the target. The resulting loss in kinetic energy is measured with the EELS detector, which disperses the electrons by energy. Normalising the total number of electrons recorded by the detector, an energy loss probability spectrum is obtained.

Our simulated EELS spectra are calculated following the approach outlined by Ref. 40, which yields the spectrally decomposed energy loss probability, $\Gamma_{\mathrm{EELS}}(\omega)$, for a fast electron moving at constant velocity v along a linear trajectory $\mathbf{r}_e(t)$. The moving electron results in a current density $\mathbf{j}(\mathbf{r},t) = -e\hat{\mathbf{v}}\delta[\mathbf{r}-\mathbf{r}_e(t)]$, where e is the electron charge. Assuming that this current is directed in the z-direction and performing a temporal Fourier transform, we obtain $\mathbf{j}(z,\omega) = -e\hat{\mathbf{z}}\delta[\mathbf{R}-\mathbf{R}_0]e^{i\omega z/v}$, where ω is the angular frequency and $\mathbf{R}_0 = (x_0, y_0)$ is the impact parameter of the electron trajectory.

The moving electron creates a background electric field, $\mathbf{E}_0(\mathbf{r},t)$, which in the presence of a metallic nanostructure results in an induced field, $\mathbf{E}^{\mathrm{ind}}(\mathbf{r},t)$. The energy lost by an electron moving along the path $\mathbf{r}_e(t)$ is then given by

$$W = e\int dt\mathbf{v}\cdot\mathbf{E}^{\mathrm{ind}}[\mathbf{r}_e(t),t]. \tag{3.16}$$

The spectral decomposition of eq. 3.16 can be obtained by writing the energy lost in terms of the energy loss probability as $W=\int\hbar\omega\Gamma_{\mathrm{EELS}}(\omega)d\omega$. Expressing the induced electric field in frequency domain, and rewriting the time integral in eq. 3.16 into a line integral over the electron path $z(t)$, we have

$$\Gamma_{\mathrm{EELS}}(\omega) = \frac{e}{2\pi\hbar\omega}\int dz\mathrm{Re}[e^{-i\omega z/v}E_z^{\mathrm{ind}}(z,\omega)], \tag{3.17}$$

where $E_z^{\mathrm{ind}}(z,\omega)$ is the z-component (parallel to the electron trajectory) of the induced electric field.

Equation 3.17 shows that the energy loss probability can be directly extracted from the induced electric field along the source current. In the following, we discuss briefly how $E_z^{\mathrm{ind}}(z,\omega)$ can be obtained from the frequency domain solution of *Maxwell*'s equations within a nonlocal hydrodynamical model. In this frame, the total electric fields, $\mathbf{E}(\mathbf{r},\omega)=\mathbf{E}_0(\mathbf{r},\omega)+\mathbf{E}^{\mathrm{ind}}(\mathbf{r},\omega)$, within an arbitrary metallic nanostructure (the target in our EELS experiments) are described by the inhomogeneous wave equation

$$\nabla\times[\nabla\times\mathbf{E}(\mathbf{r},\omega)] = \frac{\omega^2}{c^2}\epsilon_\infty\mathbf{E}(\mathbf{r},\omega)+i\mu_0\omega\mathbf{J}_{\mathrm{d}}(\mathbf{r},\omega), \tag{3.18}$$

where the first and second source terms in the right hand side account for the residual response of the positive ion cores and the nonlocal displacement current, respectively. Within the hydrodynamical *Drude* model, the transport equation for the nonlocal current $\mathbf{J}_{\mathrm{d}}(\mathbf{r},\omega)$ reads

$$\beta^2\nabla[\nabla\cdot\mathbf{J}_{\mathrm{d}}(\mathbf{r},\omega)]+\omega(\omega+i\gamma)\mathbf{J}_{\mathrm{d}}(\mathbf{r},\omega) = i\omega\omega_{\mathrm{P}}^2\epsilon_0\epsilon_\infty\mathbf{E}(\mathbf{r},\omega). \tag{3.19}$$

Equation 3.19 governs the dynamics of the electron density within the metal nanostructure. The first term takes into account the electron-electron interactions due to the non-uniform electron density within the hydrodynamic picture, and the remaining terms can be easily recognized as the usual *Drude* ones for a noninteracting electron gas. The nonlocal parameter β, which is a measure of the characteristic speed of an electron, is equal, except for an adimensional factor, to the metal Fermi velocity [15]. Note that in the limit $\beta=0$, eq. 3.19 recovers the local approximation. All the calculations in this work are evaluated at $\beta=0.0036c$, where c is the speed of light, which is a realistic value for gold [23].

The EELS source was implemented as a line current (eq. (3.17)) in *Comsol Multiphysics*, a commercial differential equation solver implementing the finite element method (note that ω is the angular frequency and $\mathbf{R}_0 = (x_0, y_0)$ is the impact parameter of the electron trajectory). Next, the *Maxwell*'s wave equation (eq. 3.18) and the hydrodynamic transport equation (eq. 3.19) were solved simultaneously using a MUltifrontal Massively Parallel Sparse direct Solver (MUMPS) [3].

Highly non-uniform tetrahedral discretization meshes were used to resolve accurately the different length scales involved in the solution of the coupled set of equations. The finest details of the nanostructures were mapped manually using grid spacings as narrow as 0.01 nm. The electron beam, the substrate and the metallic nanostructures were enclosed by a spherically symmetric Perfectly Matched Layer (PML) region that efficiently absorbs scattered EM waves. The convergence of the calculations against simulation volume, EELS line current source length, mesh resolution and PML thickness was checked systematically for variations in each of these parameters.

The gold permittivity in our calculations corresponds to the *Drude* fitting to the experimental data in Ref. 103, with a *Drude* plasma frequency parameter $\omega_P = 4.6$ eV, damping parameter $\gamma = 0.071$ eV, and background permittivity $\epsilon_\infty = 3.46$. The dielectric properties for the chromium adhesion layer were taken from Ref. 118.

For each frequency point, we performed two simulations based on an identical mesh: first, the background electric field, $\mathbf{E}_0(\mathbf{r}, \omega)$, is determined in the absence of the metallic nanostructure. Then, the metallic structure is added and the full field $\mathbf{E}(\mathbf{r}, \omega)$ is calculated. Once these quantities are known, the induced field is straightforwardly evaluated by $\mathbf{E}^{\mathrm{ind}}(\mathbf{r}, \omega) = \mathbf{E}(\mathbf{r}, \omega) - \mathbf{E}_0(\mathbf{r}, \omega)$.

Contrary to the local picture, the simultaneous solution of eqs. 3.18 and 3.19 yields the excitation of longitudinal plasmon modes within the metal bulk below the plasma frequency, ω_{P} [24]. The inclusion of this new field component in the metallic regions requires the introduction of an additional boundary condition, which in our case corresponds to the continuity of the normal component of the electric field [91]. It can be easily demonstrated that eqs. 3.18 and 3.19 gives the following longitudinal plasmon dispersion relation

$$k_\perp^2 = k_\parallel^2 + \frac{1}{\beta^2}\left[\omega_{\mathrm{P}}^2 - \omega(\omega + i\gamma)\right], \tag{3.20}$$

where $k_\perp$ ($k_\parallel$) is the evanescent (propagating) wave-vector along the direction normal (parallel) to the metal surface. In flat geometries and at frequencies much smaller than the plasma frequency, we can use the strongly evanescent nature of longitudinal plasmons to assume $k_\perp \gg k_\parallel$ and write $\delta_{\mathrm{LP}} = k_\perp^{-1} \approx \beta/\omega_{\mathrm{P}}$ for the longitudinal plasmons decay length. This result evidences the role of β as the parameter which controls the nonlocal thickening of the induced charge distribution at the metal boundaries [37; 33].

Finally, in order to obtain the induced electric fields required to evaluate eq. 3.17, we follow a solving strategy similar to the one recently proposed to calculate the electric fields scattered by on-substrate nanoparticles under dark field illumination [90; 70]. We first compute the vacuum electric fields produced by the EELS current in absence of the target, $\mathbf{E}_0(\mathbf{r},\omega)$. Subsequently, we inject these electric fields as the EM source in the simulation domain including the metal nanostructure. Thus, we can retrieve $\mathbf{E}^{\rm ind}(\mathbf{r},\omega)=\mathbf{E}(\mathbf{r},\omega)-\mathbf{E}_0(\mathbf{r},\omega)$ and compute $\Gamma_{\rm EELS}(\omega)$ from eq. 3.17.

3.5.3 Results and discussion

We first apply our nonlocal EELS machinery to the study of single gold nanoprisms. Specifically, we consider nanoparticles with an equilateral triangular cross section of side L ranging from 5 to 200 nm, and height $D=0.3L$. The gold permittivity in our calculations corresponds to the *Drude* fitting to the experimental data in Ref. 103. In order to mimic realistic experimental conditions, we place these plasmonic nanostructures on a SiN_x supporting membrane with dielectric constant $\epsilon=5$. We also introduce a thin (~ 0.5 nm) chromium adhesion layer (with dielectric properties taken from Ref. 118) between target and membrane [28] (note that nonlocal effects in chromium have been neglected in our calculations due to the low value of the Fermi velocity $\sim\beta$, which in chromium is one order of magnitude smaller than in gold [144]). Figure 3.21 (a)-(c) plot the y-component of the electric field induced in an $L=5$ nm triangle by an incident electron beam positioned 0.75 nm away from the center of one of its sides, as indicated by the grey dot in panels (b)-(c). Panel (a) plots $E_y^{\rm ind}$ as a function of the y-coordinate along the nanoprism axis ($x=0$, $z=D/2$). The electric fields are evaluated at the lowest plasmonic resonance supported by the nanostructure, and the black (red) line corresponds to local (nonlocal) predictions. Panels (b) and (c) render the local (1.6 eV) and nonlocal (1.9 eV) $E_y^{\rm ind}$, respectively, within the $z=D/2$ plane. The plots of the y-component of the electric field (normal to one of the long sides of the prisms) in Figure 3.21 (a)-(c) illustrate the central manifestation of spatial dispersion, namely the removal of the discontinuity of the normal component of the electric field at the metal boundaries. This smearing of the EM fields is concomitant with a decrease of the electric field amplitude. Note the two-fold reduction in $E_y^{\rm ind}$ at the prism corner in panel (a).

Figure 3.21 (d) shows $\Gamma_{\rm EELS}(\omega)$ for gold nanoprisms with different L obtained within the local (black) and nonlocal (red) picture. In order to make the system fully scalable, we have set the distance between target and electron beam to $0.15L$. Note that the impact of spatial dispersion is more apparent in the spectral position of the EELS maxima than in its intensity. In panel (e), the evolution of the resonant position for increasing prism side is rendered. The insets display saturated nonlocal charge density plots, $\rho\sim\nabla\cdot\mathbf{E}^{\rm ind}(\mathbf{r},\omega)$, evaluated at 1.9 and 2.4 eV for $L=5$ nm. These plots enable us to classify the two resonances observed in the spectra as in-plane dipole and quadrupole

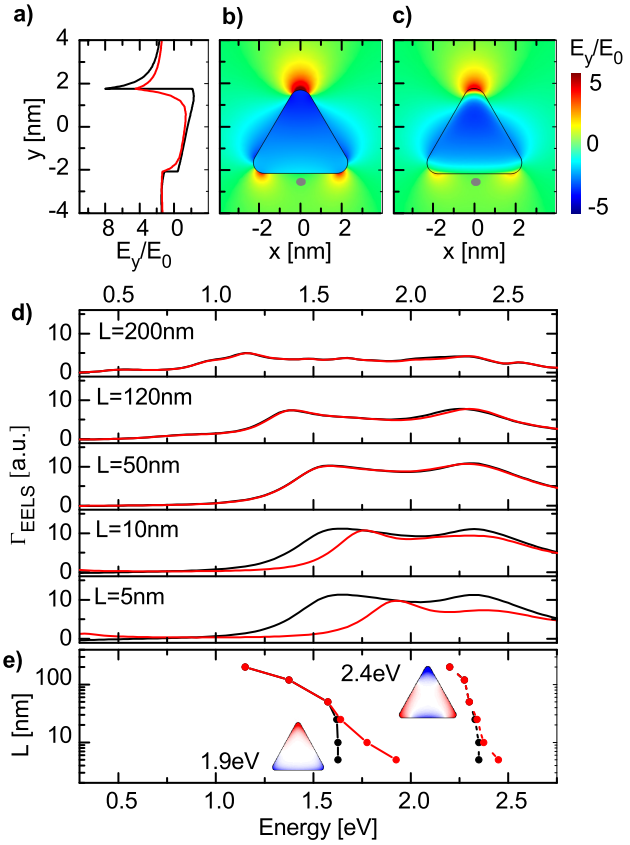


FIGURE 3.21: Simulated EELS response of single gold nanoprisms (height $D = 0.3L$) on a 1 nm chromium adhesion layer, supported by a SiN_x membrane of thickness D. (a) Black and red lines plot local (1.6 eV) and nonlocal (1.9 eV) E_y^{ind} along the y-axis of a nanoprism with $L = 5$ nm. (b) Local E_y^{ind} map within the $z = D/2$ plane at 1.6 eV. (c) The same as (b) but under the nonlocal description and at 1.9 eV. In both panels, the saturated color scale ranges from positive (red) to negative (blue) electric field amplitude, and the position of the electron beam source is indicated by a grey dot. (d) Simulated local (black) and nonlocal (red) EELS spectra for single nanoprisms with various L. In order to make the system fully scalable, we have set the distance between target and source to $0.15L$. (e) Trace of the spectral position of the modes identified in panel (d). The insets show saturated nonlocal charge density maps ($L = 5$ nm) at the energies of the dipole (1.9 eV) and quadrupole (2.4 eV) modes. Reprinted with permission from Ref. [147]. Copyright 2013 by the American Chemical Society.

plasmonic modes, respectively. Figure 3.21 (d) allows us to bracket the point at which local and nonlocal predictions begin to diverge between $L = 10$ nm and $L = 50$ nm, which is in agreement with recent experimental findings on silver nanoparticles [128; 46]. Interestingly, this onset of the nonlocal regime also corresponds to the nanoprism size range where local electrodynamics converges to the so-called quasi-static regime. In this limit, the energy of plasmonic modes is scale-invariant under the local approximation, making the spectral position of the EELS maxima independent of the overall size of the target. Figure 3.21 (e) illustrates how the introduction of spatial dispersion in the metal permittivity gives rise to a continuous blue shifting of the plasmonic modes as L

decreases. This effect can be linked to the continuous increasing of the relative size of the nonlocal surface charge thickening, given by the ratio δ_{SP}/L.

Interestingly, Figure 3.21 shows that the dipolar plasmon mode supported by gold nanoprisms is more sensitive to spatial nonlocality than its quadrupole counterpart. This can be qualitatively understood from the longitudinal plasmon dispersion given by eq. 3.20. Note that, as the spectral position of both plasmonic modes is well below ω_{P}, the second term in the right hand side of this equation acquires very similar values in both cases. However, the insets of Figure 3.21 (e) evidence that the effective wavelength, which is inversely proportional to $k_{\parallel}$ and measures the spatial extent of the EM oscillations along the nanoparticle perimeter, is significantly shorter for the quadrupole mode. By estimating the effective wavelength of the plasmonic resonances through these charge plots, δ_{LP} can be calculated from eq. 3.20. This yields a smaller longitudinal plasmon decay length for the higher order mode, which explains the lower impact that nonlocality has on its spectral position.

Next, we perform a similar study for a structure consisting of a pair of gold nanoprisms of the same dimensions as the ones investigated in Figure 3.21. As illustrated in Figure 3.22, the two prisms are mirrored at their apex and connected through a gold bridge of variable shape. We choose this geometry instead of a separated configuration for two reasons. First, nonlocal effects in gapped nanoparticles have already been investigated lately [142; 33; 25]. Second, whereas relevant quantum tunnelling effects take place in angstrom-sized plasmonic gaps [125; 127], we can expect them to be negligible in conductive junctions, which makes connected geometries a more suitable platform for the analysis of spatial nonlocality. Figure 3.22 shows the various geometric parameters of the EELS target: prism side L, height D, and bridge width and length, d and g, respectively (note that the bridge length is measured from the points where the triangles apexes would have been in a disconnected dimer). We restrict our attention to electron beams impinging in the vicinity of the center of one of the outer sides of the nanoprisms. Again, in order to make the nanostructure scalable, we set the distance target-excitation to $0.15L$.

Figure 3.23 summarizes the findings of our EELS exploration of nonlocal effects in connected gold nanoprisms. Note that the lowest resonance supported by this geometry is a charge transfer plasmonic mode characterized by a large accumulation of positive and negative charges at opposite ends of the dimer. This mode cannot be described by plasmon hybridization [109], as each of the resonant prisms, considered as isolated elements, do not satisfy charge neutrality. Figure 3.23 (a)-(c) render the electric field, E_y^{ind}, at the charge transfer mode, revealing that nonlocal effects diminish significantly the field localization that takes place around the connective bridge within the local picture. The parameters of the structure are $L = 5$ nm, $D = 1.5$ nm, $d = 0.5$ nm, and $g = 0$ nm. Note that our theoretical model does not account for grain boundary and quantum confinement effects at the gold bridges, which are expected to strongly impact

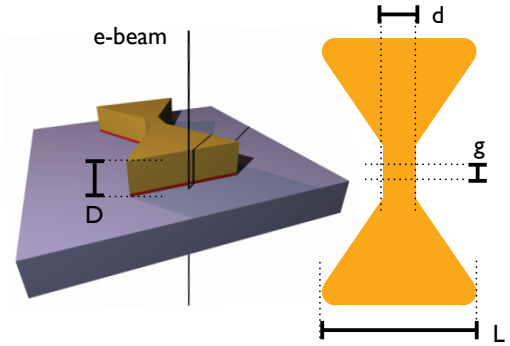


FIGURE 3.22: Geometry considered in our calculations. Two gold nanoprisms of height D and side length L, connected through a bridge of width d and length g (measured apex to apex). The resulting structure is separated from a SiN_x supporting membrane through a 0.5 nm thick chromium adhesion layer. The impact parameter of the electron beam is $0.15L$ nm away from the center of the outer side of the connected nanoprisms.

the electronic response of the smallest geometry in Figure 3.23. We anticipate that these will be introduced in a phenomenological manner in our model at a later stage.

The field enhancement in this geometry is lower than in the single prism case (note that there is no lightning rod effect at the bowtie bridge). However, the relative impact of spatial dispersion is similar to the one observed in Figure 3.21, yielding as well a two-fold reduction in E_y^{ind}. Panel (a) plots the local (black) and nonlocal (red) electric fields as a function of y ($x = 0$, $z = D/2$). Panels (b) and (c) display E_y^{ind} color maps at $z = D/2$ obtained under the local (0.75 eV) and nonlocal (0.8 eV) picture, respectively. These results show that the nonlocal smearing of the electric fields at the metal boundaries leads to a significant reduction of the field enhancement in the vicinity of the bowtie. This effect is particularly pronounced in the region of the narrow connective bridge, where the discrepancy between local and nonlocal predictions is largest.

Figure 3.23 (d) plots $\Gamma_{\mathrm{EELS}}(\omega)$ obtained from nanoprism dimers with side length ranging from 5 to 200 nm. The nanostructure height is set to $D = 0.3L$, and the bridge geometric parameters are $d = 0.1L$ and $g = 0$. Local (nonlocal) results are shown in black (red) lines. Again, the effect of nonlocality is more pronounced in the resonance position than in their intensity. The EELS spectra for the bowties are dominated by the aforementioned charge transfer peak (note that Γ_{EELS} is ~ 10 times larger than all other resonances). In order to make the fingerprint of higher order plasmonic modes in the EELS signal apparent, the vertical axes below 1 eV have been rescaled. Three different EELS resonances can be identified in our theoretical spectra, in agreement with previous studies on similar gold nanostructures. Figure 3.23 (e) renders their spectral position as a function of L. The insets show the charge distribution evaluated at the three EELS maxima for $L = 5$ nm. As anticipated, the low energy peak corresponds to the charge transfer mode. On the other hand, the two broader peaks at higher energies cannot be unambiguously characterized [28]. Both emerge in a frequency range where the structure supports two distinct but nearly degenerate plasmonic modes. Thus, the

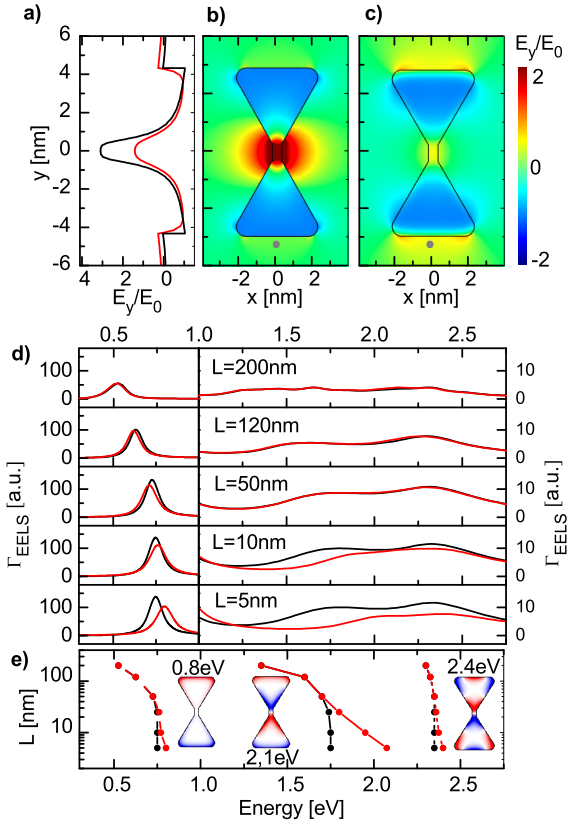


FIGURE 3.23: Simulated $\Gamma_{\mathrm{EELS}}(\omega)$ for connected gold nanoprisms of side length L and height $D = 0.3L$. The bridge width and length are $d = 0.1L$ and $g = 0$, respectively. The nanostructures are placed on top of a 0.5 nm chromium layer, and supported by a SiN_x membrane of thickness D. The distance target-excitation is $0.15L$. (a) Local (black) and nonlocal (red) E_y^{ind} along the y-axis for $L = 5$ nm evaluated at 0.75 and 0.8 eV, respectively. (b) Local E_y^{ind} maps within the $z = D/2$ plane at 0.75 eV. (c) The same as (b) but under the nonlocal description and at 0.8 eV. The position of the electron beam is indicated by a grey dot in both panels. (d) Simulated local (black) and nonlocal (red) $\Gamma_{\mathrm{EELS}}(\omega)$ for connected nanoprisms with L ranging from 5 to 200 nm. (e) Trace of the spectral position of the EELS maxima identified in panel (d). The insets show saturated nonlocal charge density maps for the $L = 5$ nm dimer. Reprinted with permission from Ref. [147]. Copyright 2013 by the American Chemical Society.

maximum between 1.4 and 2.1 eV (2.3 and 2.5 eV) originates from plasmonic modes corresponding to the parallel and antiparallel orientation of the dipole (quadrupole) resonances supported by single nanoprisms. In both cases, the charge configuration most efficiently excited by the incident electron beam is shown in the corresponding inset of Figure 3.23 (e) ($L = 5$ nm).

Similarly to the case of isolated nanoprisms, the impact of spatial dispersion on connected bowties increases with smaller size. However, the phenomenology of the modes sensitivity is more complex than in the single-particle configuration. Figure 3.23 (e) shows that both the charge transfer and the quadrupole-quadrupole peaks are rather robust to nonlocal effects. However, the dipole-dipole resonance presents a much higher sensitivity. Again, we can gain physical insight into these observations through eq. 3.20.

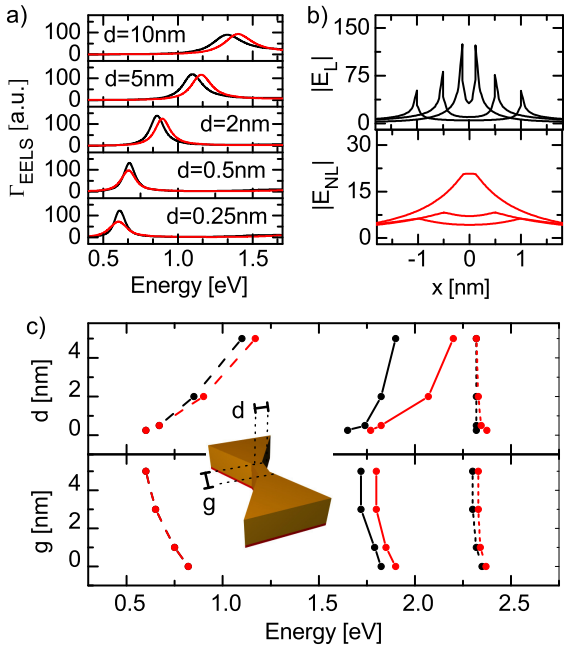


FIGURE 3.24: (a) Simulated local (black) and nonlocal (red) EELS spectra for gold nanoprisms connected by bridges of various widths, d ($L = 10$, $D = 3$, and $g = 0$ nm). The target configuration (substrate, adhesion layer, electric beam excitation) remain the same as in Figure 3.23. (b) Electric field amplitude along the bridge width for the three narrowest geometries in (a). Top (bottom) profiles correspond to local (nonlocal) calculations. (c) Trace of the local (black) and nonlocal (red) resonances for connected nanoprisms against d (top, $g = 0$ nm) and against g (bottom, $d = 1$ nm). Reprinted with permission from Ref. [147]. Copyright 2013 by the American Chemical Society.

The rapid spatial oscillation of the quadrupole-quadrupole mode effectively enlarges the longitudinal plasmon parallel wavevector, and therefore the normal component as well. In a similar way, it is the frequency term in the dispersion relation which increases $k_\perp$ for the charge transfer mode. As a result, δ_{LP} is diminished in both cases. On the other hand, for the dipole-dipole EELS maximum, both the $k_\parallel$ and the frequency term in the right hand side of eq. 3.20 acquire intermediate values. Our results indicate that the balance between these two terms yields the longest δ_{LP}, in a similar way to the dipole mode supported by a single nanoprism. Note that the nonlocal blueshift experienced by the lower energy resonance in Figure 3.21 resembles the one observed in Figure 3.23 for this mode.

The spectral properties of the plasmon modes supported by gold bowties are highly sensitive not only to the dimensions of the connected nanoprisms (as we have demonstrated above), but also to the geometry of the junction between them. This makes these structures very attractive candidates for photonic applications that rely on the precise engineering of one or several EM resonances over a wide frequency window [5; 12; 42]. In the following, we investigate how the high tunability featured by these plasmonic devices within the local approximation is affected by spatial dispersion. In Figure 3.24 (a), the

effect of the bridge width on the charge transfer mode is analyzed for connected nanoprisms with $L = 10$ nm and $D = 3$ nm. Local (black) and nonlocal (red) EELS spectra for d ranging from 0.25 to 10 nm are plotted ($g = 0$ nm). Interestingly, our results show that the impact of spatial dispersion on the position of the EELS maxima is higher at larger d. This is a surprising result, as it seems to contradict our previous observations which showed the enhancement of nonlocal effects with decreasing nanoparticle size, L. However, note that the thickest bridge ($d = 10$ nm) yields a rectangular-shaped nanoparticle, and the EELS peak in this case originates from a dipole mode similar to the one we identified in Figure 3.21 for single prisms. On the other hand, $d = 0.25$ nm corresponds to a connected dimer like the ones in Figure 3.23, and we can link the maximum in $\Gamma_{\mathrm{EELS}}(\omega)$ to a charge transfer plasmonic mode. As we showed above, the former is very sensitive to nonlocality, whereas the latter is much more robust. This explains the spectral trends that we observe in Figure 3.24 (a).

In order to gain further physical insight into the interplay between geometric and nonlocal effects at the dimer bridge, we plot in panel (b) of Figure 3.24 the local (top) and nonlocal (bottom) electric field amplitude across (x-direction) the bridge for the three narrowest bowties in panel (a). These profiles are evaluated at resonance and indicate that the electric field is significantly amplified at the junction for small d, whereas it remains moderate for wider geometries. In narrow bridges, the nonlocal smearing of the electron density effectively pushes the plasmonic modes into the metal regions, whilst decreasing their parallel wavevector. These manifestations of spatial nonlocality lead to the slower variation of the electric field amplitudes across the nanoprism junctions in panel (b). Note that, although the field accumulation for the narrow bridges does not lead to an apparent nonlocal shift of the EELS maxima, it gives rise to the highest reduction in their intensity in panel (a). In the top panel of Figure 3.24 (c), the spectral position of the EELS resonances is plotted against d for bridges narrower than 4 nm ($g = 0$ nm). In this panel, the three resonances supported by the nanostructure are investigated. As we already observed in Figure 3.23, the dipole-dipole peak at intermediate energies is the most affected by nonlocality, which also increases its sensitivity to the bridge width. In the bottom panel of Figure 3.24 (c), the effect of the bridge length g is investigated ($d = 1$ nm). This panel indicates that the bowtie resonances investigated here, even within the nonlocal description, can be only slightly tuned through this geometric parameter.

Current experimental capabilities make the accurate fabrication and characterization of plasmonic EELS samples shaped at the nanometer scale possible. Here, we compare our own theoretical findings with a set of EELS measurements obtained by other authors. [147] The experimental EELS measurements we consider were performed on a single gold bowtie antenna of 70 nm side length and 20 nm height. This target was fabricated onto a 30-nm-thick SiN_x membrane using methods previously described [63; 64; 28]. Shifts in the charge transfer plasmon mode were due only to variations in

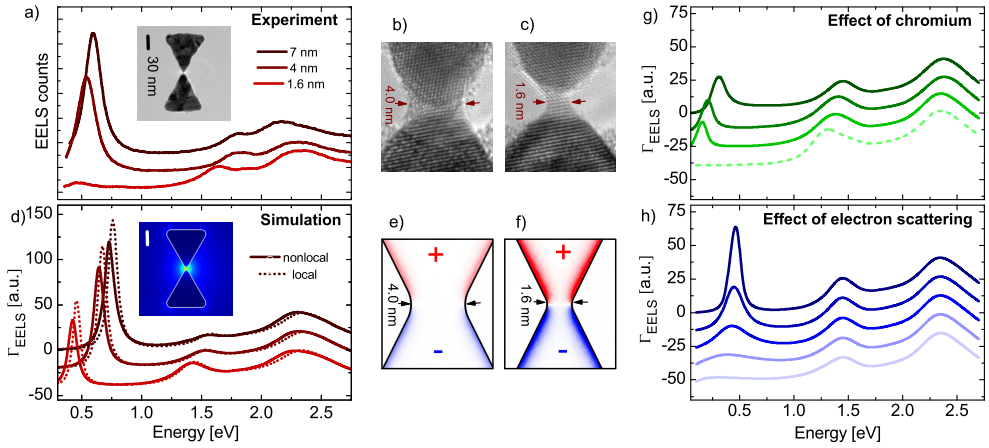


FIGURE 3.25: (a) Experimental EELS spectra for connected gold nanoprisms with $L = 70$ nm, $D = 20$ nm, and $d = 1.6$ nm, 4 nm and 7 nm. The bowties are placed on top of a 1 nm chromium layer and are supported by a 30 nm thick SiN_x membrane. The inset shows a TEM image of one of the samples. (b)-(c) TEM images zooming at the two narrowest connective bridges. (d) Local (dotted lines) and nonlocal (solid lines) simulations mirroring the experimental geometries in (a). (e)-(f) Nonlocal charge density maps evaluated at the charge transfer resonance for the geometries modelling the bridges in (b)-(c). (g) Local $\Gamma_{\mathrm{EELS}}(\omega)$ for bowties with $d = 1.6$ nm and chromium bridges of height 5, 2, 1 and 0 nm (from top to bottom). (h) The same as (g) but for 1 nm chromium thickness and increasing *Drude* damping frequency at the gold bridge, effectively modelling grain boundary electron scattering effects. The top (bottom) spectrum corresponds to an increase in the gold damping frequency by a factor of 1 (75) with respect to the prism regions. Reprinted with permission from Ref. [147]. Copyright 2013 by the American Chemical Society.

the bridge geometry, and not variations from one bowtie to another. This controlled experiment was achieved by performing local electron-beam sculpting (ablation) of the bridge region. Doing so allowed EELS spectra obtained from bridges of different widths (but of identical prisms) to be consistently compared with each other, as plotted in Figure 3.25 (a). As the bridge width was decreased from $d = 7$ nm to $d = 1.6$ nm, the charge transfer plasmon peak redshifted slightly but decreased significantly in intensity. Remarkably, these experimental results show that charge-transfer plasmons can still be supported across a bridge that is only 6 atoms across, as seen in Figure 3.25 (c).

We investigate the emergence of nonlocal effects in samples with bridge widths as small as 1.6 nm. In Figure 3.25 (a), the EELS spectra measured from three of these nanostructures (see inset for a TEM image) are plotted. Panels (b)-(c) display TEM images of the two narrowest junctions, $d = 4$ and 1.6 nm. Importantly, the experimental spectra show the signature of the plasmonic modes predicted theoretically for the structure. In agreement with the numerical $\Gamma_{\mathrm{EELS}}(\omega)$ in Figure 3.23, the lowest energy EELS maxima stand out in the measured EELS profiles. Note that the height of this peak diminishes drastically in the 1.6 nm bridge case. As expected from the numerical trends in Figure 3.24 (c), the charge transfer and the dipole-dipole resonances are more sensitive to the bridge geometry and red-shift significantly with decreasing d. On the other hand,

the quadrupole-quadrupole mode (the highest in energy) emerges at roughly the same position for the three samples.

Figure 3.25 (d) show numerical $\Gamma_{\mathrm{EELS}}(\omega)$ mimicking the experimental conditions. The model geometries in our calculations are set in accordance to the nominal dimensions of the measured samples. Dashed and solid lines correspond to local and nonlocal calculations, respectively. We can observe the good agreement with the spectra in panel (a), in particular for the two widest bridges. Our theoretical results also show the low impact that nonlocality has on the connected geometries explored in the experiments. Note that the main nonlocal feature in the EELS spectra is the further red-shift of the charge transfer mode with decreasing d. This red-shift is a striking result, because it is contrary to the phenomenology observed in single nanoparticles [128] and gapped dimers [23], where spatial dispersion always increases the surface plasmon resonant energies. Note that a slight (0.01 eV) nonlocal red-shift of the EELS maximum (with respect to the local prediction) can be also observed in the bottom spectrum of Figure 3.24 (a). We can understand this spectral lowering of the charge transfer mode as a consequence of the effective narrowing of the bridge width associated to the nonlocal smearing of the surface charge distribution at the metal boundaries [34; 74]. This interpretation is supported by the nonlocal charge density maps at the bridge areas displayed in Figures 3.25 (e)-(f). These are evaluated at the charge transfer resonance for the two narrowest bridges. Note that the color scale is the same for both structures, demonstrating the effective narrowing of the connective bridge associated to the nonlocal thickening of the surface charge distribution in the $d = 1.6$ nm case.

Our theoretical EELS spectrum does not reproduce the drastic reduction of the charge transfer peak found in the experiments for the 1.6 nm thick bridge. This means that spatial dispersion is not the cause for the severe lowering in the experimental EELS signal, and that the physical mechanism inhibiting the charge transfer plasmonic mode is not reflected in our theoretical description. To explain the drastic reduction in peak height as the bridge was narrowed, we turn to three plausible considerations, all of which result in drastically reduced conductance by the bridge. First, we consider the case in which the gold bridge has been removed and only chromium atoms remained at the junction. We realize that this is an unlikely case because the gold lattice fringes can be seen in the TEM image to extend from the individual nanoprisms into the bridge region. Nevertheless, Figure 3.25 (g) plots $\Gamma_{\mathrm{EELS}}(\omega)$ for nanoprisms with chromium bridges ranging from 5 nm (top) to 0 nm (bottom). Note that the bottom spectrum (dashed line) corresponds to a separated bowtie, which does not exhibit the charge transfer EELS maximum. We can observe that the reduction of the chromium bridge leads to a continuous red-shift of the lower energy EELS resonance similar to the one associated to the decrease in d in Figure 3.24 (c). This allows us to discard this consideration, as it does not reproduce the drastic reduction in peak height observed experimentally, and overestimates the red-shift of the peaks as the bridge was narrowed.

A second possibility is that quantum confinement present in the bridge has lowered the conductance substantially by offering a reduced number of open channels. The increased effective resistivity can be included by an enhanced Drude damping in the bridge[107]. The third plausible origin of the drastic decrease in $\Gamma_{\mathrm{EELS}}(\omega)$ at the charge transfer mode for narrow bridges is as follows, and can be described also by an increased Drude damping. The TEM images in Figures 3.25 (b)-(c) show the polycrystalline character of the bridges connecting the nanoprisms. Upon careful inspection, it is evident that the crystal orientations in the nanoprisms are different, and merge at a single grain boundary that spans the entire cross section of the $d = 1.6$ nm bowties. Grain boundaries have been described as tunnel-barriers for electron transport that introduce electron surface scattering [13] and therefore increase the *Drude* damping rate. Note that this effect is inversely proportional to the metallic cross sectional area, and therefore, we can expect that this damping mechanism will be larger for narrower bridges. To capture the effect of this locally-enhanced resistance, we increased the gold *Drude* damping only at the junction of $d = 1.6$ nm bowties. This phenomenological treatment of electron scattering is inspired in the so-called *quantum corrected model*, in which the effect of quantum tunnelling at the sub-nanometric gap between two metallic nanoparticles is modelled through an effective *Drude* permittivity with high absorption losses [32]. Figure 3.25 (h) plots the EELS spectra obtained by increasing the damping frequency in our local calculations by a factor of 1, 10, 25, 50 and 75 (top to bottom) with respect to the gold prism regions. These numbers are in good agreement with the resistivity enhancement due to electron scattering reported for polycrystalline gold nanowires with grain sizes ranging from a few nanometers to a few angstroms [155]. Our results indicate that this increase in *Drude* damping yields the observed reduction in the charge transfer peak, without altering its spectral position. Note as well that the higher energy plasmonic modes are not affected significantly by the increase in absorption losses at the prisms junction. Therefore, we can conclude that either quantum confinement or grain boundary electron scattering , or a combination of the two, are likely to be the cause of the disagreement between our theoretical and experimental results for 1.6 nm thick bridges.

3.5.4 Conclusion

In summary, we have developed a three-dimensional nonlocal hydrodynamic solution of *Maxwell*'s equations in order to investigate the electron-energy loss probing of nonlocal effects in metals structured below the nanoscale. Applying our theoretical model to single gold prisms, we have bracketed the onset of the regime of significant nonlocality for this geometry between 10 nm and 50 nm prism side length. We have extended our study to connected bowties, where the phenomenology associated to spatial dispersion is richer, analyzing the interplay between nonlocal and geometric effects for this structure in detail. Using the longitudinal plasmon decay length as a key magnitude, we have shed light into the different degrees of nonlocal sensitivity exhibited by the various

plasmonic modes supported by these two nanoparticle configurations. For connected bowties, we show that it is the dipole-dipole mode that is most affected by nonlocality, resulting in blueshifts as large as 0.7 eV for a dimer made up of prisms with side length 5 nm. Finally, we have expanded our discussion by considering existing experimental electron-energy loss spectra for gold nanoprisms connected by bridges as narrow as 1.6 nm. Here, comparison to our own theoretical calculations indicate that nonlocal effects do not appear to be pronounced. Our results reveal that, in contrast to nonlocal models which treat metals as completely homogeneous, quantum confinement and granularity at the nanometer scale need to be taken into consideration. In particular, comparison with our theoretical predictions has enabled us to reveal the strong additional damping that occurs in plasmonic nanostructures connected by diminutive junctions.

Chapter 4

Conclusion

The field of nano-optics is entering an exciting era. As the length scales of the structures under investigation approach the sub-nanometer regime, long held approximations and assumptions have come into question; such as the assumption of a local-dielectric response function [124] and more recently the quasi-static approximation. [115] In these tiny metal structures, both quantum confinement [156] and the nonlocal response [83; 108] have been shown to lead to strong physical effects, with consequences for electromagnetic field enhancements, wave confinement and extinction cross sections.

In chapter 1 of this Thesis we have reviewed the literature around different implementations of nonlocality into grid based electromagnetics calculations. After identifying a scheme based on the full hydrodynamic equation as the most appropriate one for our requirements, we have implemented the underlying equations into a nonlocal Finite Element Method (FEM) scheme in chapter 2, successfully benchmarking our implementation against an existing analytic solution by *Ruppin*. [121]

In the second part of this Thesis we have used our nonlocal FEM implementation to gain physical insight into five systems of interest: plasmonic hourglass Metal-Insulator-Metal (MIM) waveguides, kissing metallic nanowires, nanofocusing metallic tips, three-dimensional nanocrescent light harvesters, and coupled metallic nanoprisms under electron beam excitation.

In the case of plasmonic hourglass MIM waveguides we have demonstrated that in the nonlocal case Surface Plasmon Polaritons (SPPs)chapters/Chapters.tex are able to tunnel through a geometrical singularity which terminates them in the local case. We have used this result to inspire our study of kissing nanowires, where it has lead us to identify a set of new nonlocal resonances in the visible spectrum. These resonances are sensitive to the degree of nonlocality and our tests show that they are robust in large structures of up to approximately $R = 200$ nm.

Next, we have considered a third physical system which is used to concentrate light into small spatial regions: the experimentally relevant geometry of a nanofocusing metallic tip. We have derived a nonlocal analytical solution for the fields in this geometry and find excellent agreement between this new analytical solution and our nonlocal FEM simulations provided that there are no reflections from the tip. Our study shows that nonlocality leads to a reduction of the electric field amplitude at the tip of the cone as long as the fields are growing in amplitude towards the tip, but has the effect of increasing the amplitude of the fields over and above the value predicted within the local approximation if the fields decay towards the tip. We also find that the geometry parameters which lead to maximum field enhancements are modified by nonlocality. We have also demonstrated that spatial dispersion increases the robustness of plasmonic tips performance against structural imperfections such as apex bluntness and surface roughness, a result that is relevant to other plasmonic geometries with imperfect surfaces.

Building on our findings related to nanofocusing plasmonic tips, we have performed a related study into the geometrical and material properties which control the performance of nanocrescent light harvesters. Basing our investigation on a hydrodynamical FEM solution, effects of nonlocality in nanocrescents with subnanometer shells were investigated, revealing a set of nonlocal resonances in singular nano crescents, as well as a reduction of the maximum field enhancement. Specifically, we find that despite adverse effects of nonlocality, field enhancements of more than 100 can be achieved in a gold nanocrescent with diameter 80 nm and inner radius 34 nm.

Finally, we have moved beyond the limitations imposed by Two-Dimensional (2D) and axially symmetric Three-Dimensional (3D) space by applying our hydrodynamic nonlocal FEM approach to geometries in three dimensions. Applying our theoretical model to single gold prisms iluminated by an electron beam, we have bracketed the onset of the regime of significant nonlocality for this geometry between 10 nm and 50 nm prism side length. We have extended our study to connected bowties, using the longitudinal plasmon decay length as a key magnitude to shed light into the different degrees of nonlocal sensitivity exhibited by the various plasmonic modes supported by these two nanoparticle configurations. We have expanded our discussion by considering a set of experimental electron-energy loss spectra for gold nanoprisms connected by bridges as narrow as 1.6 nm, obtained by other authors. Thus, comparison with results obtained from our theoretical calculations has enabled us to reveal the strong additional damping that occurs in plasmonic nanostructures connected by metallic junctions only a few atomic layers thick.

In conclusion, our results indicate that whilst classical electrodynamics provides an excellent framework for the description and analysis of plasmonic phenomena in most systems of experimental relevance, this formalism is no longer sufficient when the effective wavelengths that characterise the Electromagnetic (EM) modes supported by plasmonic devices are squeezed into deep sub-wavelength volumes. At such length scales, plasmonic

structures often consist of only a handful of atomic layers, such as in the case of the plasmonic tips considered in section 3.3 or the sub-nanometric bridges investigated in section 3.5. The principal effects of nonlocality that span all our results are a reduction in field enhancements, which can be as large as two orders of magnitude in the case of the kissing nanowires studied in section 3.2, as well as a blue shift of the Localised Surface Plasmon Resonance (LSPR) modes which, as illustrated by our results for triangular prisms in section 3.5 show, is most pronounced in small structures.

In those geometries where Propagating Surface Plasmonss (PSPs) can occur, such as in the plasmonic voids considered in section 3.1, the plasmonic tips of section 3.3, and the self-interfering circulating PSPs found on the surface of the kissing nano wires of section 3.2, we find that spatial dispersion results in an increased effective wavelength of these modes at a fixed frequency.

Finally, we stress that nonlocality is not the only effect that needs to be considered when investigating sub-nanometric plasmonic structures. As evidenced by our study of bridged metallic nanoprisms, when metallic structures approach each other and are separated by only a few Angstroms, additional quantum effects, such as electron tunnelling, will need to be taken into account.

Bibliography

[1] *Comsol Multiphysics User's Guide*. Version 4.1. www.comsol.com, 2011.

[2] A. L. Aden and M. Kerker. Scattering of electromagnetic waves from two concentric spheres. *J. Appl. Phys.*, 22:1242–1246, 1951.

[3] P. R. Amestoy, I. S. Duff, and J. Y. L'Excellent. Multifrontal parallel distributed symmetric and unsymmetric solvers. *Computer Methods in Applied Mechanics and Engineering*, 184(2-4):501–520, 2000.

[4] M. Anderegg, B. Feuerbacher, and B. Fitton. Optically excited longitudinal plasmons in potassium. *Phys. Rev. Lett.*, 27(23):1565–1568, 1971.

[5] J. N. Anker, W. P. Hall, O. Lyandres, N. C. Shah, J. Zhao, and R. P. Van Duyne. Biosensing with plasmonic nanosensors. *Nature Materials*, 7(6):442–453, 2008.

[6] N. Ashcroft and D. Mermin. *Solid State Physics*. Holt, Rinehart, and Winston, 1976.

[7] H. A. Atwater and A. Polman. Plasmonics for improved photovoltaic devices. *Nature Materials*, 9(3):205–213, 2010.

[8] A. Aubry, D. Y. Lei, A. I. Fernández-Domínguez, Y. Sonnefraud, S. A. Maier, and J. B. Pendry. Plasmonic light-harvesting devices over the whole visible spectrum. *Nano Letters*, 10(7):2574–2579, 2010.

[9] A. Aubry, D. Y. Lei, S. A. Maier, and J. B. Pendry. Plasmonic hybridization between nanowires and a metallic surface: A. transformation optics approach. *ACS nano*, 5(4):3293–3308, 2011.

[10] R. D. Averitt, S. L. Westcott, and N. J. Halas. Linear optical properties of gold nanoshells. *J. Optl. Am. B*, 16:1824–1832, 1999.

[11] R. Bardhan, N. K. Grady, T. Ali, and N. J. Halas. Metallic nanoshells with semiconductor cores: Optical characteristics modified by core medium properties. *ACS Nano*, 4:6169–6179, 2010.

[12] P. Bharadwaj, B. Deutsch, and L. Novotny. Optical antennas. *Adv. Opt. Photonics*, 1:438–483, 2009.

[13] A. Bietsch and B. Michel. Size and grain-boundary effects of a gold nanowire measured by conducting atomic force microscopy. *Appl. Phys. Lett.*, 80:3346, 2002.

[14] N. Bloembergen, R. Chang, S. Jha, and C. Lee. Optical second-harmonic generation in reflection from media with inversion symmetry. *Phys. Rev.*, 174(3):813–822, 1968.

[15] A. D. Boardman. *Electromagnetic Surface Modes*. Wiley, New York, 1982.

[16] C. F. Bohren and D. R. Huffman. Absorption and scattering of light by small particles. *Wiley-VCH*, 1998.

[17] M. Born and E. Wolf. *Principles of Optics*. Cambridge, 1999.

[18] M. Bosman, V. J. Keast, M. Watanabe, A. I. Maaroof, and M. B. Cortie. Mapping surface plasmons at the nanometre scale with an electron beam. *Nanotechnology*, 18:165505, 2007.

[19] R. P. Brent. *Algorithms for minimization without derivatives*. Dover Publications Inc, 1973.

[20] R. Bukasov and J. S. Shumaker-Parry. Highly tunable infrared extinction properties of gold nanocrescents. *Nano Letters*, 7:1113–1118, 2007.

[21] D. E. Chang, A. S. Sørensen, P. R. Hemmer, and M. D. Lukin. Quantum optics with surface plasmons. *Phys. Rev. Lett.*, 97:053002, 2006.

[22] H. Choo, M. K. Kim, M. Staffaroni, T. J. Seok, J. Bokor, S. Cabrini, P. J. Schuck, M. C. Wu, and E. Yablonovitch. Nanofocusing in a metal–insulator–metal gap plasmon waveguide with a three-dimensional linear taper. *Nature Photon*, 6(12):838–844, 2012.

[23] C. Ciraci, R. T. Hill, J. J. Mock, Y. Urzhumov, A. I. Fernandez-Dominguez, S. A. Maier, J. B. Pendry, A. Chilkoti, and D. R. Smith. Probing the ultimate limits of plasmonic enhancement. *Science*, 337(6098):1072–1074, 2012.

[24] C. Ciracì, J. B. Pendry, and D. R. Smith. Hydrodynamic model for plasmonics: A. macroscopic approach to a microscopic problem. *ChemPhysChem*, 14(6):1109–1116, 2013.

[25] C. David and F. J. García de Abajo. Spatial nonlocality in the optical response of metal nanoparticles. *The Journal of Physical Chemistry C*, 115(40):19470–19475, 2011.

[26] P. Drude. Zur elektronentheorie der metalle. *Annalen der Physik*, 306(3):566–613, 1900.

[27] P. Drude. Zur elektronentheorie der metalle; ii. teil. galvanomagnetische und thermomagnetische effecte. *Annalen der Physik*, 308(11):369–402, 1900.

[28] H. Duan, A. I. Fernández-Domínguez, M. Bosman, S. A. Maier, and J. K. W. Yang. Nanoplasmonics: Classical down to the nanometer scale. *Nano Letters*, 12(3):1683–1689, 2012.

[29] P. M. Echenique, R. H. Ritchie, N. Barberán, and J. Inkson. Semiclassical image potential at a solid surface. *Ultramicroscopy*, 23:6486–6493, 1981.

[30] P. M. Echenique, A. Rivacoba, N. Zabala, and R. H. Ritchie. Electron energy loss in stem spectra. *Springer Proc. Phys.*, 62:127–134, 1991.

[31] R. F. Egerton. Electron energy-loss spectroscopy in the tem. *Rep. Prog. Phys.*, 72:016502, 2009.

[32] R. Esteban, A. G. Borisov, P. Nordlander, and J. Aizpurua. Bridging quantum and classical plasmonics with a quantum-corrected model. *Nat. Commun.*, 3:825, 2012.

[33] A. I. Fernández-Domímguez, P. Zhang, S. A. Maier, F. J. García-Vidal, and J. B. Pendry. Transformation-optics insight into nonlocal effects in separated nanowires. *Phys. Rev. B*, 86:241110R, 2012.

[34] A. I. Fernández-Domínguez, Y. Luo, A. Wiener, J. B. Pendry, and S. A. Maier. Theory of three-dimensional nanocrescent light harvesters. *Nano Letters*, 12(11):5946–5953, 2012.

[35] A. I. Fernández-Domínguez, S. A. Maier, and J. B. Pendry. Collection and concentration of light by touching spheres: A transformation optics approach. *Phys. Rev. Lett.*, 105:266807, Dec 2010.

[36] A. I. Fernández-Domínguez, L. Martín-Moreno, F. J. García-Vidal, S. R. Andrews, and S. A. Maier. Spoof surface plasmon polariton modes propagating along periodically corrugated wires. *IEEE Journal of Selected Topics in Quantum Electronics*, 14, 2008.

[37] A. I. Fernández-Domínguez, A. Wiener, F. J. García-Vidal, S. A. Maier, and J. B. Pendry. Transformation-optics description of nonlocal effects in plasmonic nanostructures. *Phys. Rev. Lett.*, 108:106802, Mar 2012.

[38] R. Fuchs and F. Claro. Multipolar response of small metallic spheres: Nonlocal theory. *Phys. Rev. B*, 35:3722–3727, Mar 1987.

[39] R. Fuchs and K. Kliewer. Surface plasmon in a semi-infinite free-electron gas. *Phys. Rev. B.*, 3(7):2270–2278, 1971.

[40] F. García de Abajo and M. Kociak. Probing the photonic local density of states with electron energy loss spectroscopy. *Phys. Rev. Lett.*, 100(10), 2008.

[41] F. J. García de Abajo. Nonlocal effects in the plasmons of strongly interacting nanoparticles, dimers, and waveguides. *J. Phys. Chem. C*, 112(46):17983–17987, 2008.

[42] V. Giannini, A. I. Fernández-Domínguez, Y. Sonnefraud, T. Roschuk, R. Fernández-García, and S. A. Maier. Controlling light localization and light-matter interactions with nanoplasmonics. *Small*, 6:2498–2507, 2010.

[43] V. Giannini, A. I. Fernández-Domínguez, S. C. Heck, and S. A. Maier. Plasmonic nanoantennas: Fundamentals and their use in controlling the radiative properties of nanoemitters. *Chemical Reviews*, 111(6):3888–3912, 2011.

[44] D. K. Gramotnev and S. I. Bozhevolnyi. Plasmonics beyond the diffraction limit. *Nature Photonics*, 4(2):83–91, 2010.

[45] D. K. Gramotnev, M. W. Vogel, and M. I. Stockman. Optimized nonadiabatic nanofocusing of plasmons by tapered metal rods. *Journal of Applied Physics*, 104(3):034311–034311–8, aug 2008.

[46] H. Haberland. Looking from both sides. *Nature*, 494:E1–E2, 2013.

[47] N. J. Halas, S. Lal, W. S. Chang, S. Link, and P. Nordlander. Plasmons in strongly coupled metallic nanostructures. *Chemical Reviews*, 111(6):3913–3961, 2011.

[48] N. Halas. Playing with plasmons: Tuning the optical resonant properties of metallic nanoshells. *MRS Bulletin*, 30:362–367, 2005.

[49] P. Halevi. Generalised additional boundary condition for non-local dielectrics. i. reflectivity. *Journal of Physics C: Solid State Physics*, 1984.

[50] P. Halevi. Hydrodynamic model for the degenerate free-electron gas: Generalization to arbitrary frequencies. *Phys. Rev. B*, 51(12):7497–7499, 1995.

[51] B. Hecht, H. Bielefeldt, L. Novotny, Y. Inouye, and D. Pohl. Local excitation, scattering, and interference of surface plasmons. *Phys. Rev. Lett.*, 77(9):1889–1892, 1996.

[52] K. Henneberger. Additional boundary conditions: An historical mistake. *Phys. Rev. Lett.*, 80(13):2889–2892, 1998.

[53] O. Hess, J. B. Pendry, S. A. Maier, R. F. Oulton, J. M. Hamm, and K. L. Tsakmakidis. Active nanoplasmonic metamaterials. *Nature Materials*, 11:573–584, 2012.

[54] L. R. Hirsch, R. J. Stafford, J. A. Bankson, S. R. Sershen, B. Rivera, R. E. Price, J. D. Hazle, N. J. Halas, and J. L. West. Nanoshell-mediated near-infrared thermal therapy of tumors under magnetic resonance guidance. *Proceedings of the National Academy of Sciences of the United States of America*, 100:13549–13554, 2003.

[55] U. Hohenester, H. Ditlbacher, and J. Krenn. Electron-energy-loss spectra of plasmonic nanoparticles. *Phys. Rev. Lett.*, 103(10), 2009.

[56] J. C. Idrobo, W. Walkosz, S. F. Yip, S. Öğüt, J. Wang, and J. Jellinek. Static polarizabilities and optical absorption spectra of gold clusters (au_n, $n = 2^{\smile}14$ and 20) from first principles. *Phys. Rev. B*, 76:205422, Nov 2007.

[57] J. D. Jackson. Classical electrodynamics (3rd edition). *Wiley*, 1998.

[58] P. Jewsbury. Electrodynamic boundary conditions at metal interfaces. *Multiple values selected*, 11(1):195–206, 2000.

[59] J. Jin. *The finite element method in electromagnetics*. Wiley-IEEE Press, 2002.

[60] P. B. Johnson and R. W. Christy. Optical constants of the noble metals. *Phys. Rev. B*, 6(12):4370–4379, 1972.

[61] C. Kittel. *Introduction to Solid State Physics*. Wiley, New York, 1996.

[62] M. W. Knight and N. J. Halas. Nanoshells to nanoeggs to nanocups: optical properties of reduced symmetry core-shell nanoparticles beyond the quasi-static limit. *New Journal of Physics*, 10:105006, 2008.

[63] A. L. Koh, D. W. McComb, S. A. Maier, H. Y. Low, and J. Yang. Sub-10 nm patterning of gold nanostructures on silicon-nitride membranes for plasmon mapping with electron energy-loss spectroscopy. *J. Vac. Sci. Technol. B.*, 28:C6O45, 2010.

[64] A. L. Koh, A. I. Fernández-Domínguez, D. W. McComb, S. A. Maier, and J. K. W. Yang. High-resolution mapping of electron-beam-excited plasmon modes in lithographically defined gold nanostructures. *Nano Letters*, 11(3):1323–1330, 2011.

[65] A. V. Krasavin and N. I. Zheludev. Active plasmonics: Controlling signals in au/ga waveguide using nanoscale structural transformations. *Applied Physics Letters*, 84(8):1416–1418, 2004.

[66] E. Kretschmann. Die bestimmung optischer konstanten von metallen durch anregung von oberflächenplasmaschwingungen. *Zeitschrift für Physik A. Hadrons and Nuclei*, 241(4):313–324, 1971.

[67] S. Lal, S. Link, and N. J. Halas. Nano-optics from sensing to waveguiding. *Nature Photon*, 1(11):641–648, 2007.

[68] L. D. Landau and E. M. Lifshits. Electrodynamics of continuous media, second edition: Volume 8 (course of theoretical physics) (2 edition). *Butterworth-Heinemann*, 1984.

[69] J. B. Lassiter, M. W. Knight, N. A. Mirin, and N. J. Halas. Reshaping the plasmonic properties of an individual nanoparticle. *Nano Letters*, 9:4326–4332, 2009.

[70] D. Y. Lei, A. I. Fernández-Domínguez, Y. Sonnefraud, A. Kannatassen, R. F. J. Haglund, J. B. Pendry, and S. A. Maier. Revealing plasmonic gap modes in particle-on-film systems using dark-field spectroscopy. *ACS Nano*, 6:1380–1386, 2012.

[71] D. Y. Lei, A. Aubry, S. A. Maier, and J. B. Pendry. Broadband nano-focusing of light using kissing nanowires. *New Journal of Physics*, 12(9):093030, 2010.

[72] I. Lindau and P. Nilsson. Experimental verification of optically excited longitudinal plasmons. *Physica Scripta*, 3:87, 1971.

[73] Y. Lu, G. L. Liu, J. Kim, Y. X. Mejia, and L. P. Lee. Nanophotonic crescent moon structures with sharp edge for ultrasensitive biomolecular detection by local electromagnetic field enhancement effect. *Nano Letters*, 5:119–124, 2005.

[74] Y. Luo, A. I. Fernández-Domínguez, A. Wiener, S. A. Maier, and J. B. Pendry. Local analogue to spatial nonlocality. page Submitted, 2013.

[75] Y. Luo, D. Y. Lei, S. A. Maier, and J. B. Pendry. Broadband light harvesting nanostructures robust to edge bluntness. *Phys. Rev. Lett.*, 108:023901, 2012.

[76] Y. Luo, D. Y. Lei, S. A. Maier, and J. B. Pendry. Transformation-optics description of plasmonic nanostructures containing blunt edges/corners: From symmetric to asymmetric edge rounding. *ACS Nano*, 6:6492–6506, 2012.

[77] Y. Luo, J. B. Pendry, and A. Aubry. Surface plasmons and singularities. *Nano Letters*, 10(4186–4191), 2010.

[78] K. F. MacDonald, Z. L. Sámson, M. I. Stockman, and N. I. Zheludev. Ultrafast active plasmonics. *Nature Photonics*, 3(1):55–58, 2008.

[79] S. A. Maier. *Plasmonics: Fundamentals and Applications*. Springer, 2007.

[80] S. A. Maier, S. R. Andrews, L. Martín-Moreno, and F. J. García-Vidal. Terahertz surface plasmon-polariton propagation and focusing on periodically corrugated metal wires. *Physical Review Letters*, 97:176805, 2006.

[81] M. P. Marder. *Condensed Matter Physics*. Marder/Condensed. John Wiley & Sons, Inc., Hoboken, NJ, USA, 2010.

[82] D. C. Marinica, A. K. Kazansky, P. Nordlander, J. Aizpurua, and A. G. Borisov. Quatum plasmonics: Nonlinear effects in the field enhandement of a plasmonic nanoparticle dimer. *Nano Letters*, 12:1333–1339, 2012.

[83] J. McMahon, S. Gray, and G. Schatz. Nonlocal optical response of metal nanostructures with arbitrary shape. *Physical Review Letters*, 103(9):097403, 2009.

[84] J. Mcmahon, S. Gray, and G. Schatz. Calculating nonlocal optical properties of structures with arbitrary shape. *Phys. Rev. B*, 82(3):035423, 2010.

[85] J. McMahon, S. Gray, and G. Schatz. Nonlocal dielectric effects in core-shell nanowires. *J. Phys. Chem. C*, 2010.

[86] J. McMahon, S. Gray, and G. Schatz. Optical properties of nanowire dimers with a spatially nonlocal dielectric function. *Nano Letters*, 10(9):3473–3481, 2010.

[87] A. Melnyk and M. Harrison. Theory of optical excitation of plasmons in metals. *Phys. Rev. B*, 2(4):835–850, 1970.

[88] G. Mie. Beiträge zur optik trüber medien, speziell kolloidaler metallösungen. *Annalen der Physik*, 330(3):377–445, 1908.

[89] M. I. Mishchenko, L. D. Travis, and A. A. Lacis. *Scattering, absorption, and emission of light by small particles*. Cambridge Univ Press, 2002.

[90] A. Moreau, C. Ciraci, and D. R. Smith. Influence of excitation and collection geometry on the dark field spectra of individual plasmonic nanostructures. *Opt. Express*, 18:2579–2587, 2010.

[91] A. Moreau, C. Ciraci, and D. R. Smith. Impact of nonlocal response on metallodielectric multilayers and optical patch antennas. *Phys. Rev. B*, 87:045401, 2013.

[92] N. A. Mortensen, S. Raza, M. Wubs, T. Søndergaard, and S. I. Bozhevolnyi. A generalized non-local optical response theory for plasmonic nanostructures. *Nat Comms*, 5, 2014.

[93] N. A. Mortensen. Nonlocal formalism for nanoplasmonics: Phenomenological and semi-classical considerations. *Photonics and Nanostructures - Fundamentals and Applications*, 2013.

[94] C. L. Nehl, N. K. Grady, G. P. Goodrich, F. Tam, N. J. Halas, and J. H. Hafner. Scattering spectra of single gold nanoshells. *Nano Letters*, 4:2355–2359, 2004.

[95] J. Nelayah, M. Kociak, O. Stéphan, F. J. García de Abajo, M. Tencé, L. Henrard, D. Taverna, I. Pastoriza-Santos, L. M. Liz-Marzán, and C. Colliex. Mapping surface plasmons on a single metallic nanoparticle. *Nat Phys*, 3(5):348–353, 2007.

[96] K. Nerkararyan. Superfocusing of a surface polariton in a wedge-like structure. *Physics Letters A*, 237(1-2):103–105, 1997.

[97] L. Novotny and H. Bert. *Principles of Nano-Optics*. Cambridge, 2006.

[98] L. Novotny and N. van Hulst. Antennas for light. *Nature Photonics*, 5:83–90, 2011.

[99] A. Otto. Excitation of nonradiative surface plasma waves in silver by the method of frustrated total reflection. *Zeitschrift für Physik A. Hadrons and Nuclei*, 216(4):398–410, 1968.

[100] R. F. Oulton, V. J. Sorger, T. Zentgraf, R. M. Ma, C. Gladden, L. Dai, G. Bartal, and X. Zhang. Plasmon lasers at deep subwavelength scale. *Nature*, 461:629–632, 2009.

[101] F. Ouyang, P. E. Batson, and M. Isaacson. Quantum size effects in the surface-plasmon excitation of small metallic particles by electron-energy-loss spectroscopy. *Phys. Rev. B*, 46:15421–15425, 1992.

[102] E. Ozbay. Plasmonics: Merging photonics and electronics at nanoscale dimensions. *Science*, 311(5758):189–193, 2006.

[103] E. D. Palik. *Handbook of Optical Constants of Solids*. Academic Press Handbook Series, New York, 1985.

[104] S. Palomba, L. Novotny, and R. E. Palmer. Blue-shifted plasmon resonance of individual size-selected gold nanoparticles. *Optics Communications*, 281(3):480–483, 2008.

[105] S. I. Pekar. The theory of electromagnetic waves in a crystal in which excitons are produced. *Soviet Journal of Experimental and Theoretical Physics*, 6:785, 1958.

[106] J. B. Pendry, A. Aubry, D. Smith, and S. A. Maier. Transformation optics and subwavelength control of light. *Science*, 337:549–552, 2012.

[107] O. Pérez-González, N. Zabala, A. G. Borisov, N. J. Halas, P. Nordlander, and J. Aizpurua. Optical spectroscopy of conductive junctions in plasmonic cavities. *Nano Letters*, 10(8):3090–3095, 2010.

[108] J. M. Pitarke, V. M. Silkin, E. V. Chulkov, and P. Echenique. Theory of surface plasmons and surface-plasmon polaritons. *Reports on Progress in Physics*, 70:1, 2007.

[109] E. Prodan, C. Radloff, N. J. Halas, and P. Nordlander. A hybridization model for the plasmon response of complex nanostructures. *Science*, 302:5644, 2003.

[110] E. Prodan, P. Nordlander, and N. J. Halas. Electronic structure and optical properties of gold nanoshells. *Nano Letters*, 3:1411–1415, 2003.

[111] B. Radt, T. A. Smith, and C. F. Optically addressable nanostructured capsules. *Advanced Materials*, 16:2184–2189, 2004.

[112] H. Raether. *Surface plasmons on smooth and rough surfaces and on gratings.* Springer Verlag, 1988.

[113] G. Raschke, S. Brogl, A. S. Shusa, A. L. Rogach, T. A. Klar, J. Feldmann, B. Fieres, N. Petkov, T. Bein, A. Nichtl, and K. Kürzinger. Gold nanoshells improve single nanoparticle molecular sensors. *Nano Letters*, 4:1853–1857, 2004.

[114] S. Raza, T. Christensen, M. Wubs, S. I. Bozhevolnyi, and N. A. Mortensen. Nonlocal response in thin-film waveguides: Loss versus nonlocality and breaking of complementarity, 2013.

[115] S. Raza, G. Toscano, A. P. Jauho, M. Wubs, and N. A. Mortensen. Unusual resonances in nanoplasmonic structures due to nonlocal response. *Phys. Rev. B*, 84:121412, 2011.

[116] S. Raza, N. Stenger, S. Kadkhodazadeh, S. V. Fischer, N. Kostesha, A.-P. Jauho, A. Burrows, M. Wubs, and N. A. Mortensen. Blueshift of the surface plasmon resonance in silver nanoparticles studied with eels. *Nanophotonics*, 2:131, 2013.

[117] A. Rivacoba, N. Zabala, and J. Aizpurua. Image potential in scanning transmission electron microscopy. *Prog. Surf. Sci.*, 65:1, 2000.

[118] S. Rodrigo, F. García-Vidal, and L. Martin-Moreno. Influence of material properties on extraordinary optical transmission through hole arrays. *Phys. Rev. B*, 77(7):075401, 2008.

[119] B. M. Ross and L. P. Lee. Plasmon tuning and local field enhancement maximization of the nanocrescent. *Nanotechnology*, 19:275201, 2008.

[120] R. Ruppin. Mie theory with spatial dispersion. *Optics Communications*, 30(3):380–382, 1979.

[121] R. Ruppin. Optical properties of a spatially dispersive cylinder. *JOSA B, Vol. 6, Issue 4, pp. 787-796*, 6(8):1559–1563, 1989.

[122] R. Ruppin. Extinction properties of thin metallic nanowires. *Optics Communications*, 190(1-6):205–209, 2001.

[123] R. Ruppin. Effect of non-locality on nanofocusing of surface plasmon field intensity in a conical tip. *Physics Letters A*, 340(1-4):299–302, 2005.

[124] R. Ruppin. Non-local optics of the near field lens. *Journal of Physics: Condensed Matter*, 17(12):1803–1810, 2005.

[125] K. J. Savage, M. M. Hawkeye, R. Esteban, A. G. Borisov, J. Aizpurua, and J. J. Baumberg. Revealing the quantum regime in tunnelling plasmonics. *Nature*, 491(7425):574–577, 2012.

[126] M. Scalora, M. A. Vincenti, D. de Ceglia, V. Roppo, M. Centini, N. Akozbek, and M. J. Bloemer. Second- and third-harmonic generation in metal-based structures. *Physical Review A*, 82(4):043828, 2010.

[127] J. A. Scholl, A. García-Etxarri, A. L. Koh, and J. A. Dionne. Observation of quantum tunneling between two plasmonic nanoparticles. *Nano Letters*, 13(2):564–569, 2013.

[128] J. A. Scholl, A. L. Koh, and J. A. Dionne. Quantum plasmon resonances of individual metallic nanoparticles. *Nature*, 483(7390):421–427, 2012.

[129] D. Schurig, J. J. Mock, B. J. Justice, S. A. Cummer, J. B. Pendry, A. F. Starr, and D. R. Smith. Metamaterial electromagnetic cloak at microwave frequencies. *Science*, 314(5801):977, 2006.

[130] J. Sipe, V. So, M. Fukui, and G. Stegeman. Analysis of second-harmonic generation at metal surfaces. *Phys. Rev. B*, 21(10):4389–4402, 1980.

[131] Y. Sivan, Y. Sonnefraud, S. Kena-Cohen, J. B. Pendry, and M. S. A. Nanoparticle-assisted stimulated-emission-depletion nanoscopy. *ACS Nano*, 6:5291–5296, 2012.

[132] D. R. Smith, J. B. Pendry, and M. C. K. Wiltshire. Metamaterials and negative refractive index. *Science*, 305(5685):788, 2004.

[133] L. Stella, P. Zhang, F. J. García-Vidal, A. Rubio, and P. García-González. Performance of non-local optics when applied to plasmonic nanostructures. *J. Phys. Chem. C*, Article ASAP, 2013.

[134] M. I. Stockman. Nanofocusing of optical energy in tapered plasmonic waveguides. *Physical Review Letters*, 93(13):137404, 2004.

[135] Y. Sun, B. Mayers, and X. Younan. Metal nanostructures with hollow interiors. *Advanced Materials*, 15:641–646, 2003.

[136] A. Taflove. Computational electrodynamics: The finite-difference time-domain method (3rd revised edition edition). *Artech House*.

[137] F. Tam, C. Moran, and N. J. Halas. Geometrical parameters controlling sensitivity of nanoshell plasmon resonances to changes in dielectric environment. *J. Phys. Chem. B*, 108:17290–17294, 2004.

[138] T. V. Teperik, P. Nordlander, J. Aizpurua, and A. G. Borisov. Robust subnanometric plasmon ruler by rescaling of the nonlocal optical response. *Phys. Rev. Lett.*, 110:263901, 2013.

[139] T. V. Teperik, P. Nordlander, J. Aizpurua, and A. G. Borisov. Quantum effects and nonlocality in strongly coupled plasmonic nanowire dimers. *Optics Express, Vol. 16, Issue 26, pp. 21626-21640*, 21(22):27306, 2013.

[140] G. Toscano, S. Raza, W. Yan, C. Jeppesen, S. Xiao, M. Wubs, A. P. Jauho, S. I. Bozhevolnyi, and N. A. Mortensen. Nonlocal response in plasmonic waveguiding with extreme light confinement. *Nanophotonics*, 2(3), 2013.

[141] G. Toscano, M. Wubs, S. Xiao, M. Yan, Z. F. ztrk, A. Jauho, and N. A. Mortensen. Proceedings of spie. In *Plasmonics: Metallic Nanostructures and Their Optical Properties VIII*, pages 77571T–77571T–7. SPIE, 2010.

[142] G. Toscano, S. Raza, A.-P. Jauho, N. A. Mortensen, and M. Wubs. Modified field enhancement and extinction by plasmonic nanowire dimers due to nonlocal response. *Opt. Express*, 20(4):4176–4188, Feb 2012.

[143] G. Toscano, M. Wubs, S. Xiao, M. Yan, Z. F. Oztürk, A.-P. Jauho, and N. A. Mortensen. Plasmonic nanostructures: local versus nonlocal response. pages 7757, 77571T, 2010.

[144] Y. Tsunoda, Y. Hamaguchi, and N. Kunitomi. Neutron scattering measurements in chromium near the néel temperature. *J. Phys. Soc. Jpn.*, 32(2):394–399, 1972.

[145] A. Unger, U. Rietzler, R. Berger, and M. Kreiter. Sensitivity of crescent-shaped metal nanoparticles to attachment of dielectric colloids. *Nano Letters*, 9:2311–2315, 2009.

[146] H. Wang, Y. Wu, B. Lassiter, C. L. Nehl, J. H. Hafner, P. Nordlander, and N. J. Halas. Symmetry breaking in individual plasmonic nanoparticles. *Proceedings of the National Academy of Sciences of the United States of America*, 103:10856–10860, 2006.

[147] A. Wiener, H. Duan, M. Bosman, A. P. Horsfield, J. B. Pendry, J. K. W. Yang, S. A. Maier, and A. I. Fernández-Domínguez. Electron-energy loss study of nonlocal effects in connected plasmonic nanoprisms. *ACS Nano*, 7(7):6287–6296, 2013.

[148] A. Wiener, A. I. Fernández-Domínguez, A. P. Horsfield, J. B. Pendry, and S. A. Maier. Nonlocal effects in the nanofocusing performance of plasmonic tips. *Nano Letters*, 12(6):3308–3314, 2012.

[149] A. Wiener, A. I. Fernández-Domínguez, J. B. Pendry, A. P. Horsfield, and S. A. Maier. Nonlocal propagation and tunnelling of surface plasmons in metallic hourglass waveguides. *Optics Express, Vol. 16, Issue 26, pp. 21626-21640*, 21(22):27509, 2013.

[150] K. A. Willets and R. P. Van Duyne. Localized surface plasmon resonance spectroscopy and sensing. *Annu. Rev. Phys. Chem.*, 58(1):267–297, 2007.

[151] L. Y. Wu, B. M. Ross, and L. P. Lee. Optical properties of the crescent-shaped nanohole antenna. *Nano Letters*, 9:1956–1961, 2009.

[152] H. Xu, E. Bjerneld, M. Käll, and L. Börjesson. Spectroscopy of single hemoglobin molecules by surface enhanced raman scattering. *Phys. Rev. Lett.*, 83(21):4357–4360, 1999.

[153] W. Yan, M. Wubs, and N. A. Mortensen. Hyperbolic metamaterials: Nonlocal response regularizes broadband supersingularity. *Phys. Rev. B*, 86(20):205429, 2012.

[154] N. Zabala and P. M. Echenique. Energy loss of fast electrons moving near plane boundaries with dispersive media. *Ultramicroscopy*, 32:327, 1990.

[155] L. Zhu, K. Jin, and X. Zheng. Effect of quantum transport on the resistivity of metal nanocrystalline materials in an electric field. *Appl. Phys. Lett.*, 91:103108, 2007.

[156] J. Zuloaga, E. Prodan, and P. Nordlander. Quantum description of the plasmon resonances of a nanoparticle dimer. *Nano Letters*, 9(2):887–891, 2009.

A1 Drude fitting

In the local limit the Drude metal permittivity may be expressed as

$$\epsilon_{\mathrm{D}}(\omega) = \epsilon_{\infty} - \frac{\omega_{\mathrm{P}}^2}{\omega(\omega + i\gamma)} \tag{1}$$

where ϵ_{∞}, ω_{P} and γ are considered fitting parameters. In all calculations, these local Drude constants were taken from the fitting to *Palik* experimental data for silver [103]. The result of the fitting of eq. (1), over the frequency range considered in our studies, is shown in fig. 1.

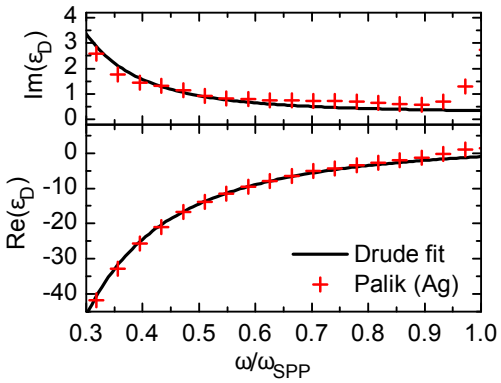
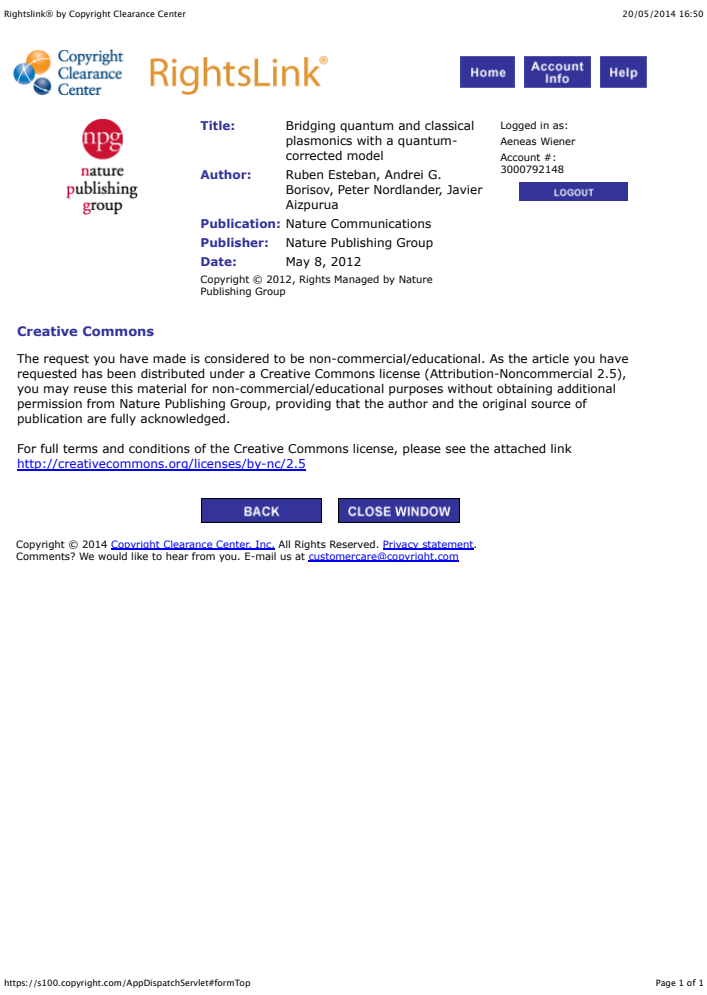


FIGURE 1: Real (bottom panel) and imaginary (top panel) parts of the permittivity used in all calculations. Results from Palik experimental data for silver (red crosses) are compared to our Drude fit based on 1 (black lines). The Drude fitting parameters are $\epsilon_{\infty} = 3.46 + 0.256i$, $\omega_{\mathrm{P}} = 8.59\mathrm{eV}$, $\gamma = 0.075\mathrm{eV}$, which gives $\mathrm{Re}(\epsilon_{\mathrm{D}}) = -1$ at $\omega_{\mathrm{SPP}} = 4.06\mathrm{eV}$.

A2 Copies of permission documents



Rightslink® by Copyright Clearance Center 20/05/2014 16:50

Copyright Clearance Center RightsLink®

Home | Account Info | Help

nature publishing group

Title: Bridging quantum and classical plasmonics with a quantum-corrected model

Author: Ruben Esteban, Andrei G. Borisov, Peter Nordlander, Javier Aizpurua

Publication: Nature Communications

Publisher: Nature Publishing Group

Date: May 8, 2012

Copyright © 2012, Rights Managed by Nature Publishing Group

Logged in as:
Aeneas Wiener
Account #:
3000792148

LOGOUT

Creative Commons

The request you have made is considered to be non-commercial/educational. As the article you have requested has been distributed under a Creative Commons license (Attribution-Noncommercial 2.5), you may reuse this material for non-commercial/educational purposes without obtaining additional permission from Nature Publishing Group, providing that the author and the original source of publication are fully acknowledged.

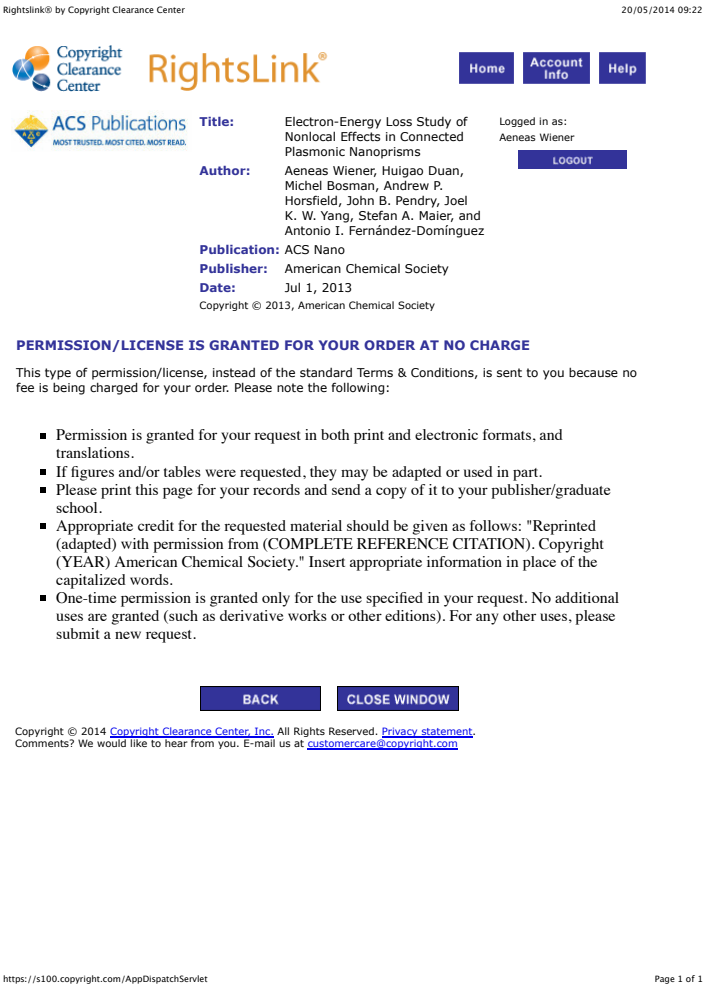
For full terms and conditions of the Creative Commons license, please see the attached link http://creativecommons.org/licenses/by-nc/2.5

BACK | CLOSE WINDOW

Copyright © 2014 Copyright Clearance Center, Inc. All Rights Reserved. Privacy statement.
Comments? We would like to hear from you. E-mail us at customercare@copyright.com

https://s100.copyright.com/AppDispatchServlet#formTop Page 1 of 1

FIGURE 2: Permission to reproduce figures from: Bridging quantum and classical plasmonics with a quantum-corrected model



Rightslink® by Copyright Clearance Center 20/05/2014 09:22

Copyright Clearance Center RightsLink® Home Account Info Help

ACS Publications MOST TRUSTED. MOST CITED. MOST READ.

Title: Electron-Energy Loss Study of Nonlocal Effects in Connected Plasmonic Nanoprisms

Author: Aeneas Wiener, Huigao Duan, Michel Bosman, Andrew P. Horsfield, John B. Pendry, Joel K. W. Yang, Stefan A. Maier, and Antonio I. Fernández-Domínguez

Publication: ACS Nano

Publisher: American Chemical Society

Date: Jul 1, 2013

Copyright © 2013, American Chemical Society

Logged in as: Aeneas Wiener LOGOUT

PERMISSION/LICENSE IS GRANTED FOR YOUR ORDER AT NO CHARGE

This type of permission/license, instead of the standard Terms & Conditions, is sent to you because no fee is being charged for your order. Please note the following:

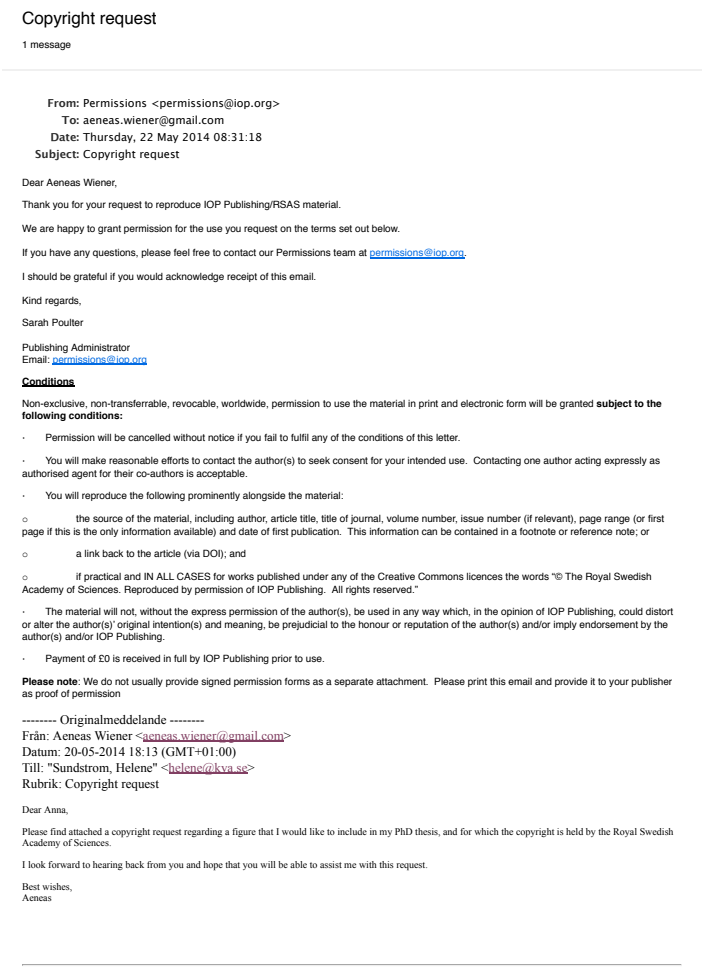
- Permission is granted for your request in both print and electronic formats, and translations.
- If figures and/or tables were requested, they may be adapted or used in part.
- Please print this page for your records and send a copy of it to your publisher/graduate school.
- Appropriate credit for the requested material should be given as follows: "Reprinted (adapted) with permission from (COMPLETE REFERENCE CITATION). Copyright (YEAR) American Chemical Society." Insert appropriate information in place of the capitalized words.
- One-time permission is granted only for the use specified in your request. No additional uses are granted (such as derivative works or other editions). For any other uses, please submit a new request.

BACK CLOSE WINDOW

Copyright © 2014 Copyright Clearance Center, Inc. All Rights Reserved. Privacy statement.
Comments? We would like to hear from you. E-mail us at customercare@copyright.com

https://s100.copyright.com/AppDispatchServlet Page 1 of 1

FIGURE 3: Permission to reproduce figures from: Electron-Energy Loss Study of Nonlocal Effects in Connected Plasmonic Nanoprisms



Copyright request

1 message

From: Permissions <permissions@iop.org>
To: aeneas.wiener@gmail.com
Date: Thursday, 22 May 2014 08:31:18
Subject: Copyright request

Dear Aeneas Wiener,

Thank you for your request to reproduce IOP Publishing/RSAS material.

We are happy to grant permission for the use you request on the terms set out below.

If you have any questions, please feel free to contact our Permissions team at permissions@iop.org.

I should be grateful if you would acknowledge receipt of this email.

Kind regards,

Sarah Poulter

Publishing Administrator
Email: permissions@iop.org

Conditions

Non-exclusive, non-transferrable, revocable, worldwide, permission to use the material in print and electronic form will be granted **subject to the following conditions:**

· Permission will be cancelled without notice if you fail to fulfil any of the conditions of this letter.

· You will make reasonable efforts to contact the author(s) to seek consent for your intended use. Contacting one author acting expressly as authorised agent for their co-authors is acceptable.

· You will reproduce the following prominently alongside the material:

○ the source of the material, including author, article title, title of journal, volume number, issue number (if relevant), page range (or first page if this is the only information available) and date of first publication. This information can be contained in a footnote or reference note; or

○ a link back to the article (via DOI); and

○ if practical and IN ALL CASES for works published under any of the Creative Commons licences the words "© The Royal Swedish Academy of Sciences. Reproduced by permission of IOP Publishing. All rights reserved."

· The material will not, without the express permission of the author(s), be used in any way which, in the opinion of IOP Publishing, could distort or alter the author(s)' original intention(s) and meaning, be prejudicial to the honour or reputation of the author(s) and/or imply endorsement by the author(s) and/or IOP Publishing.

· Payment of £0 is received in full by IOP Publishing prior to use.

Please note: We do not usually provide signed permission forms as a separate attachment. Please print this email and provide it to your publisher as proof of permission

-------- Originalmeddelande --------
Från: Aeneas Wiener <aeneas.wiener@gmail.com>
Datum: 20-05-2014 18:13 (GMT+01:00)
Till: "Sundstrom, Helene" <helene@kva.se>
Rubrik: Copyright request

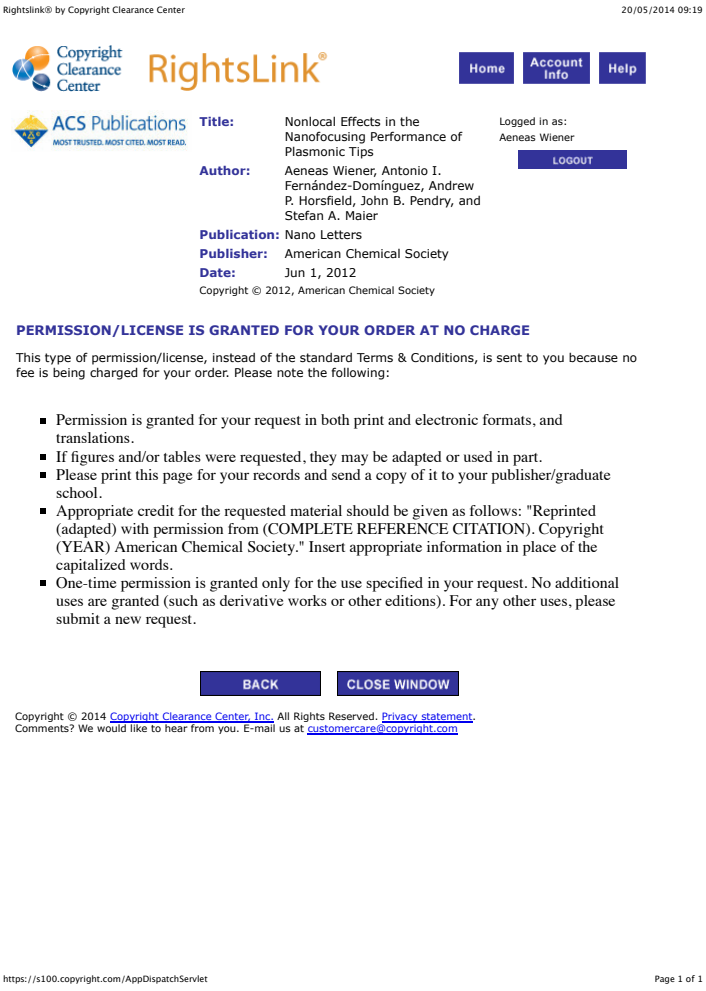
Dear Anna,

Please find attached a copyright request regarding a figure that I would like to include in my PhD thesis, and for which the copyright is held by the Royal Swedish Academy of Sciences.

I look forward to hearing back from you and hope that you will be able to assist me with this request.

Best wishes,
Aeneas

FIGURE 4: Permission to reproduce figures from: Experimental Verification of Optically Excited Longitudinal Plasmons



Rightslink® by Copyright Clearance Center 20/05/2014 09:19

Copyright Clearance Center RightsLink® Home Account Info Help

ACS Publications MOST TRUSTED. MOST CITED. MOST READ.

Title: Nonlocal Effects in the Nanofocusing Performance of Plasmonic Tips

Author: Aeneas Wiener, Antonio I. Fernández-Domínguez, Andrew P. Horsfield, John B. Pendry, and Stefan A. Maier

Publication: Nano Letters

Publisher: American Chemical Society

Date: Jun 1, 2012

Copyright © 2012, American Chemical Society

Logged in as: Aeneas Wiener LOGOUT

PERMISSION/LICENSE IS GRANTED FOR YOUR ORDER AT NO CHARGE

This type of permission/license, instead of the standard Terms & Conditions, is sent to you because no fee is being charged for your order. Please note the following:

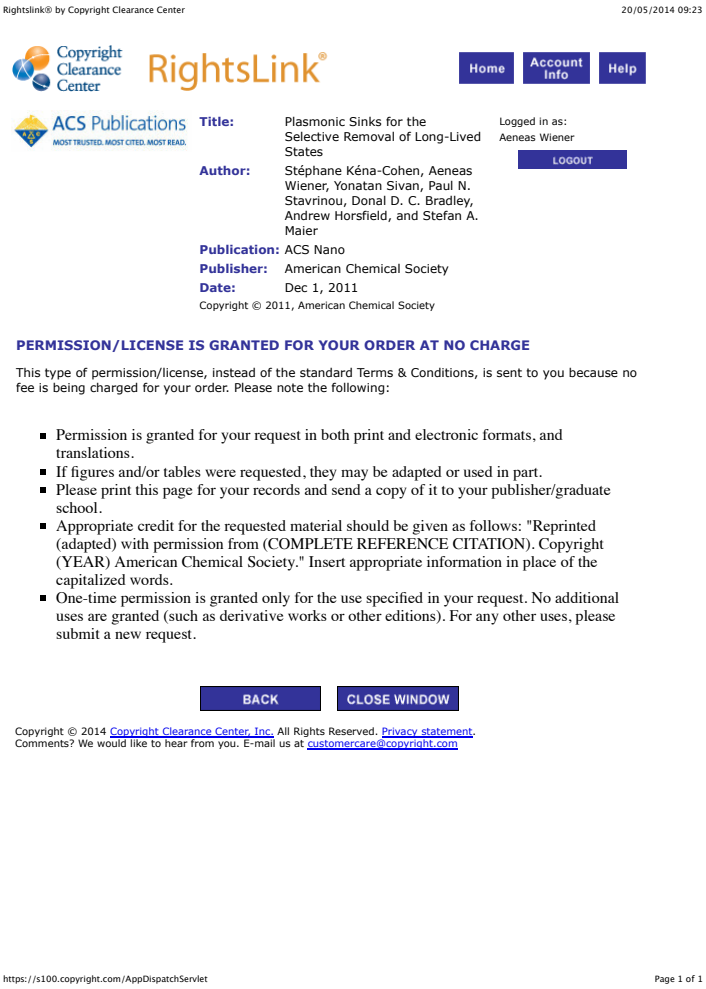
- Permission is granted for your request in both print and electronic formats, and translations.
- If figures and/or tables were requested, they may be adapted or used in part.
- Please print this page for your records and send a copy of it to your publisher/graduate school.
- Appropriate credit for the requested material should be given as follows: "Reprinted (adapted) with permission from (COMPLETE REFERENCE CITATION). Copyright (YEAR) American Chemical Society." Insert appropriate information in place of the capitalized words.
- One-time permission is granted only for the use specified in your request. No additional uses are granted (such as derivative works or other editions). For any other uses, please submit a new request.

BACK CLOSE WINDOW

Copyright © 2014 Copyright Clearance Center, Inc. All Rights Reserved. Privacy statement.
Comments? We would like to hear from you. E-mail us at customercare@copyright.com

https://s100.copyright.com/AppDispatchServlet Page 1 of 1

FIGURE 5: Permission to reproduce figures from: Nonlocal Effects in the Nanofocusing Performance of Plasmonic Tips



Rightslink® by Copyright Clearance Center 20/05/2014 09:23

Copyright Clearance Center RightsLink®

Home | Account Info | Help

ACS Publications
MOST TRUSTED. MOST CITED. MOST READ.

Title: Plasmonic Sinks for the Selective Removal of Long-Lived States

Author: Stéphane Kéna-Cohen, Aeneas Wiener, Yonatan Sivan, Paul N. Stavrinou, Donal D. C. Bradley, Andrew Horsfield, and Stefan A. Maier

Publication: ACS Nano

Publisher: American Chemical Society

Date: Dec 1, 2011

Copyright © 2011, American Chemical Society

Logged in as:
Aeneas Wiener
LOGOUT

PERMISSION/LICENSE IS GRANTED FOR YOUR ORDER AT NO CHARGE

This type of permission/license, instead of the standard Terms & Conditions, is sent to you because no fee is being charged for your order. Please note the following:

- Permission is granted for your request in both print and electronic formats, and translations.
- If figures and/or tables were requested, they may be adapted or used in part.
- Please print this page for your records and send a copy of it to your publisher/graduate school.
- Appropriate credit for the requested material should be given as follows: "Reprinted (adapted) with permission from (COMPLETE REFERENCE CITATION). Copyright (YEAR) American Chemical Society." Insert appropriate information in place of the capitalized words.
- One-time permission is granted only for the use specified in your request. No additional uses are granted (such as derivative works or other editions). For any other uses, please submit a new request.

BACK CLOSE WINDOW

Copyright © 2014 Copyright Clearance Center, Inc. All Rights Reserved. Privacy statement.
Comments? We would like to hear from you. E-mail us at customercare@copyright.com

https://s100.copyright.com/AppDispatchServlet Page 1 of 1

FIGURE 6: Permission to reproduce figures from: Plasmonic Sinks for the Selective Removal of Long-Lived States

Rightslink Printable License 20/05/2014 16:39

THE AMERICAN ASSOCIATION FOR THE ADVANCEMENT OF SCIENCE LICENSE TERMS AND CONDITIONS

May 20, 2014

This is a License Agreement between Aeneas Wiener ("You") and The American Association for the Advancement of Science ("The American Association for the Advancement of Science") provided by Copyright Clearance Center ("CCC"). The license consists of your order details, the terms and conditions provided by The American Association for the Advancement of Science, and the payment terms and conditions.

All payments must be made in full to CCC. For payment instructions, please see information listed at the bottom of this form.

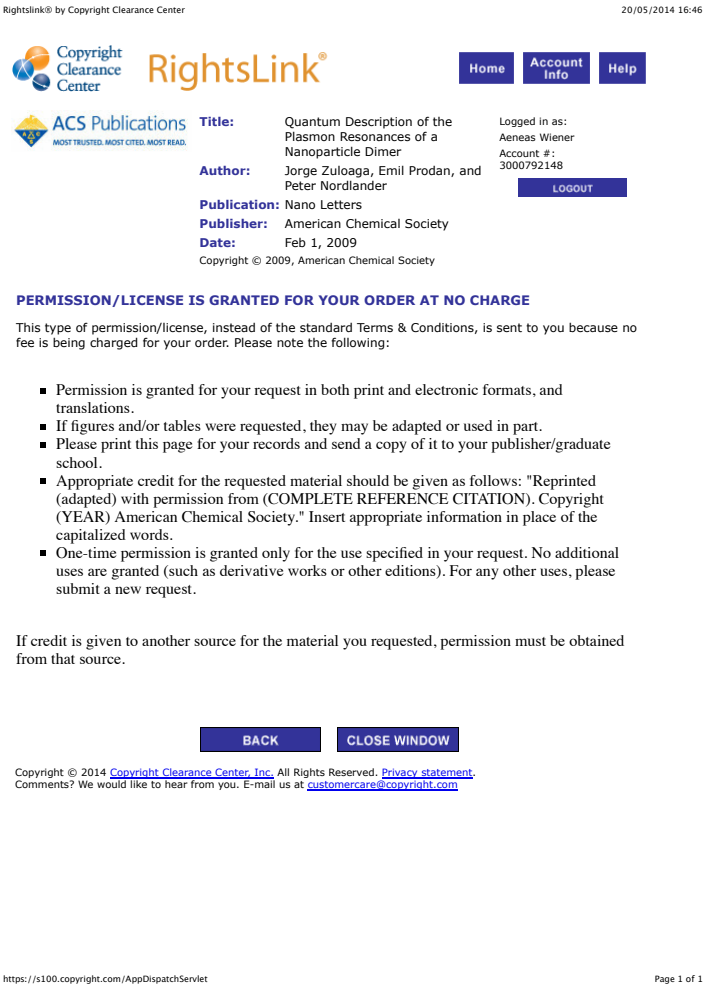
License Number	3393130655680
License date	May 20, 2014
Licensed content publisher	The American Association for the Advancement of Science
Licensed content publication	Science
Licensed content title	Probing the Ultimate Limits of Plasmonic Enhancement
Licensed content author	C. Ciracì, R. T. Hill, J. J. Mock, Y. Urzhumov, A. I. Fernández-Domínguez, S. A. Maier, J. B. Pendry, A. Chilkoti, D. R. Smith
Licensed content date	Aug 31, 2012
Volume number	337
Issue number	6098
Type of Use	Thesis / Dissertation
Requestor type	Scientist/individual at a research institution
Format	Print and electronic
Portion	Figure
Number of figures/tables	2
Order reference number	None
Title of your thesis / dissertation	Nonlocal Effects in Plasmonic Nanostructures
Expected completion date	Oct 2014
Estimated size(pages)	150
Total	0.00 USD
Terms and Conditions	

American Association for the Advancement of Science TERMS AND CONDITIONS

Regarding your request, we are pleased to grant you non-exclusive, non-transferable permission, to republish the AAAS material identified above in your work identified above,

https://s100.copyright.com/App/PrintableLicenseFrame.jsp?publisher...ff8-d581-45df-8696-a69ae4d1cc8e%20%20&targetPage=printablelicense Page 1 of 8

FIGURE 7: Permission to reproduce figures from: Probing the Ultimate Limits of Plasmonic Enhancement



Rightslink® by Copyright Clearance Center 20/05/2014 16:46

Copyright Clearance Center RightsLink® Home Account Info Help

ACS Publications MOST TRUSTED. MOST CITED. MOST READ.

Title: Quantum Description of the Plasmon Resonances of a Nanoparticle Dimer
Author: Jorge Zuloaga, Emil Prodan, and Peter Nordlander
Publication: Nano Letters
Publisher: American Chemical Society
Date: Feb 1, 2009
Copyright © 2009, American Chemical Society

Logged in as: Aeneas Wiener
Account #: 3000792148
LOGOUT

PERMISSION/LICENSE IS GRANTED FOR YOUR ORDER AT NO CHARGE

This type of permission/license, instead of the standard Terms & Conditions, is sent to you because no fee is being charged for your order. Please note the following:

- Permission is granted for your request in both print and electronic formats, and translations.
- If figures and/or tables were requested, they may be adapted or used in part.
- Please print this page for your records and send a copy of it to your publisher/graduate school.
- Appropriate credit for the requested material should be given as follows: "Reprinted (adapted) with permission from (COMPLETE REFERENCE CITATION). Copyright (YEAR) American Chemical Society." Insert appropriate information in place of the capitalized words.
- One-time permission is granted only for the use specified in your request. No additional uses are granted (such as derivative works or other editions). For any other uses, please submit a new request.

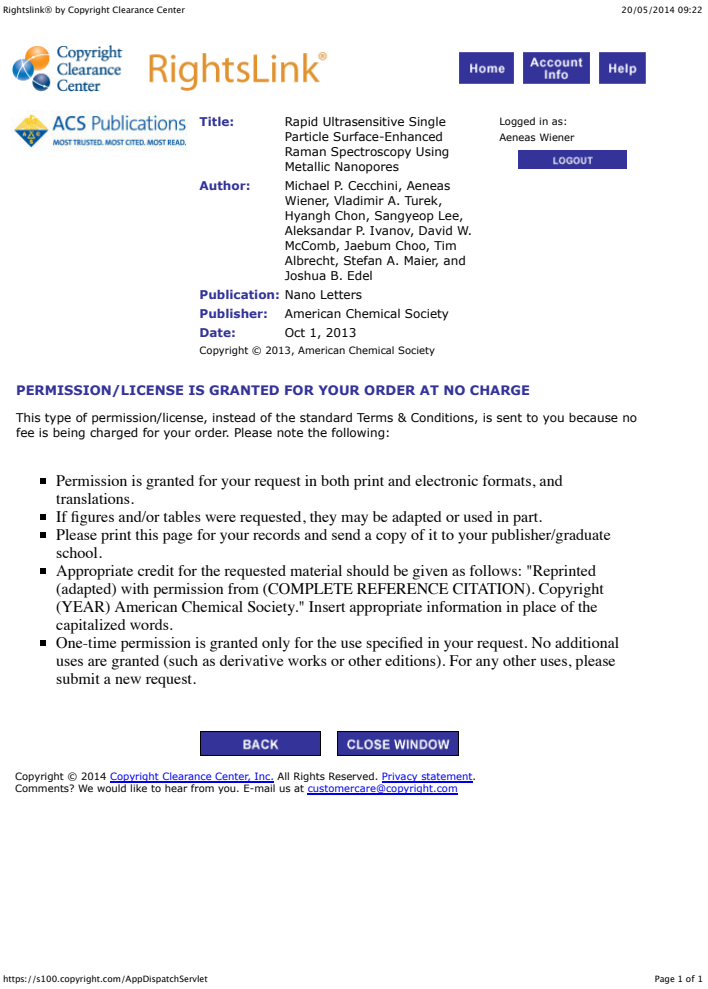
If credit is given to another source for the material you requested, permission must be obtained from that source.

BACK CLOSE WINDOW

Copyright © 2014 Copyright Clearance Center, Inc. All Rights Reserved. Privacy statement.
Comments? We would like to hear from you. E-mail us at customercare@copyright.com

https://s100.copyright.com/AppDispatchServlet Page 1 of 1

FIGURE 8: Permission to reproduce figures from: Quantum Description of the Plasmon Resonances of a Nanoparticle Dimer



Rightslink® by Copyright Clearance Center 20/05/2014 09:22

Copyright Clearance Center RightsLink® Home Account Info Help

ACS Publications MOST TRUSTED. MOST CITED. MOST READ.

Title: Rapid Ultrasensitive Single Particle Surface-Enhanced Raman Spectroscopy Using Metallic Nanopores

Author: Michael P. Cecchini, Aeneas Wiener, Vladimir A. Turek, Hyangh Chon, Sangyeop Lee, Aleksandar P. Ivanov, David W. McComb, Jaebum Choo, Tim Albrecht, Stefan A. Maier, and Joshua B. Edel

Publication: Nano Letters

Publisher: American Chemical Society

Date: Oct 1, 2013

Copyright © 2013, American Chemical Society

Logged in as: Aeneas Wiener LOGOUT

PERMISSION/LICENSE IS GRANTED FOR YOUR ORDER AT NO CHARGE

This type of permission/license, instead of the standard Terms & Conditions, is sent to you because no fee is being charged for your order. Please note the following:

- Permission is granted for your request in both print and electronic formats, and translations.
- If figures and/or tables were requested, they may be adapted or used in part.
- Please print this page for your records and send a copy of it to your publisher/graduate school.
- Appropriate credit for the requested material should be given as follows: "Reprinted (adapted) with permission from (COMPLETE REFERENCE CITATION). Copyright (YEAR) American Chemical Society." Insert appropriate information in place of the capitalized words.
- One-time permission is granted only for the use specified in your request. No additional uses are granted (such as derivative works or other editions). For any other uses, please submit a new request.

BACK CLOSE WINDOW

Copyright © 2014 Copyright Clearance Center, Inc. All Rights Reserved. Privacy statement.
Comments? We would like to hear from you. E-mail us at customercare@copyright.com

https://s100.copyright.com/AppDispatchServlet Page 1 of 1

FIGURE 9: Permission to reproduce figures from: Rapid Ultrasensitive Single Particle Surface-Enhanced Raman Spectroscopy Using Metallic Nanopores

Rightslink Printable License 20/05/2014 16:44

NATURE PUBLISHING GROUP LICENSE TERMS AND CONDITIONS

May 20, 2014

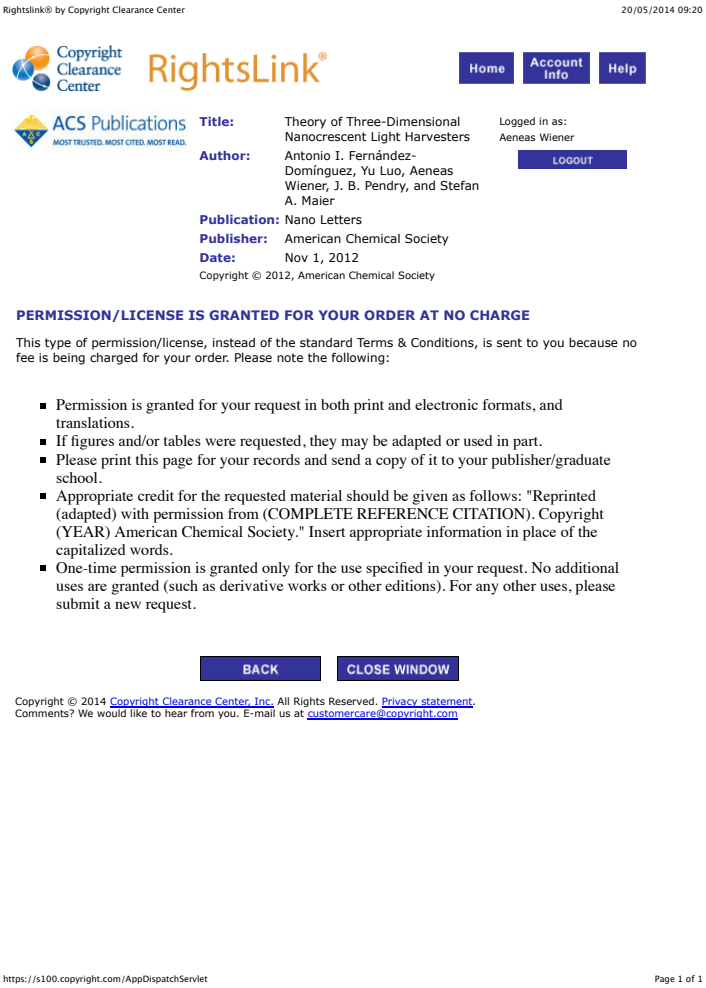
This is a License Agreement between Aeneas Wiener ("You") and Nature Publishing Group ("Nature Publishing Group") provided by Copyright Clearance Center ("CCC"). The license consists of your order details, the terms and conditions provided by Nature Publishing Group, and the payment terms and conditions.

All payments must be made in full to CCC. For payment instructions, please see information listed at the bottom of this form.

License Number	3393130935796
License date	May 20, 2014
Licensed content publisher	Nature Publishing Group
Licensed content publication	Nature
Licensed content title	Revealing the quantum regime in tunnelling plasmonics
Licensed content author	Kevin J. Savage, Matthew M. Hawkeye, Rubén Esteban, Andrei G. Borisov, Javier Aizpurua, Jeremy J. Baumberg
Licensed content date	Nov 7, 2012
Volume number	491
Issue number	7425
Type of Use	reuse in a dissertation / thesis
Requestor type	academic/educational
Format	print and electronic
Portion	figures/tables/illustrations
Number of figures/tables/illustrations	1
High-res required	no
Figures	Figure 2: Onset of quantum tunnelling in sub-nm plasmonic cavities.
Author of this NPG article	no
Your reference number	None
Title of your thesis / dissertation	Nonlocal Effects in Plasmonic Nanostructures
Expected completion date	Oct 2014
Estimated size (number of pages)	150
Total	0.00 USD
Terms and Conditions	

https://s100.copyright.com/App/PrintableLicenseFrame.jsp?publisher...cf3-a849-4969-9766-36003f753dcc%20%20&targetPage=printablelicense Page 1 of 3

FIGURE 10: Permission to reproduce figures from: Revealing the quantum regime in tunnelling plasmonics



Rightslink® by Copyright Clearance Center 20/05/2014 09:20

Copyright Clearance Center RightsLink® Home Account Info Help

ACS Publications MOST TRUSTED. MOST CITED. MOST READ.

Title: Theory of Three-Dimensional Nanocrescent Light Harvesters

Author: Antonio I. Fernández-Domínguez, Yu Luo, Aeneas Wiener, J. B. Pendry, and Stefan A. Maier

Publication: Nano Letters

Publisher: American Chemical Society

Date: Nov 1, 2012

Copyright © 2012, American Chemical Society

Logged in as: Aeneas Wiener LOGOUT

PERMISSION/LICENSE IS GRANTED FOR YOUR ORDER AT NO CHARGE

This type of permission/license, instead of the standard Terms & Conditions, is sent to you because no fee is being charged for your order. Please note the following:

- Permission is granted for your request in both print and electronic formats, and translations.
- If figures and/or tables were requested, they may be adapted or used in part.
- Please print this page for your records and send a copy of it to your publisher/graduate school.
- Appropriate credit for the requested material should be given as follows: "Reprinted (adapted) with permission from (COMPLETE REFERENCE CITATION). Copyright (YEAR) American Chemical Society." Insert appropriate information in place of the capitalized words.
- One-time permission is granted only for the use specified in your request. No additional uses are granted (such as derivative works or other editions). For any other uses, please submit a new request.

BACK CLOSE WINDOW

Copyright © 2014 Copyright Clearance Center, Inc. All Rights Reserved. Privacy statement.
Comments? We would like to hear from you. E-mail us at customercare@copyright.com

https://s100.copyright.com/AppDispatchServlet Page 1 of 1

FIGURE 11: Permission to reproduce figures from: Theory of Three-Dimensional Nanocrescent Light Harvesters